



universität
wien

MASTERARBEIT / MASTER'S THESIS

Titel der Masterarbeit / Title of the Master's Thesis

„Trojan Twin Planets“

verfasst von / submitted by

Igor Kraut, BSc

angestrebter akademischer Grad / in partial fulfilment of the requirements for the degree of
Master of Science (MSc)

Wien, 2018 / Vienna 2018

Studienkennzahl lt. Studienblatt /
degree programme code as it appears on
the student record sheet:

A 066 861

Studienrichtung lt. Studienblatt /
degree programme as it appears on
the student record sheet:

Masterstudium Astronomie

Betreut von / Supervisor:

ao. Univ.-Prof. i.R. tit. Univ.-Prof. Dr. Rudolf Dvorak

“Achilles glared at him and answered, ”Fool, prate not to me about covenants. There can be no covenants between men and lions, wolves and lambs can never be of one mind, but hate each other out and out an through. Therefore there can be no understanding between you and me, nor may there be any covenants between us, till one or other shall fall”

Homer, The Iliad

Contents

1	Introduction	3
2	Restricted Three-Body Problem	5
2.1	Potential of Circular R3BP	5
2.2	Solution of the Circular R3BP	6
2.2.1	Lagrangian Point L1	7
2.2.2	Lagrangian Point L2	8
2.2.3	Lagrangian Point L3	8
3	Trojans	9
3.1	The Origin of Trojans	11
3.2	Motion of Trojans around Triangular Lagrangian Points	12
3.2.1	Tadpole and Horseshoe Orbits	13
3.3	Exo-Trojans and Trojan Planets	14
3.3.1	Mass Limit for a Trojan Planet	15
4	Trojan Twin Planets	17
4.1	From R3BP to Twin Trojan Planets	17
4.2	Restrictions on the Parameters	18
4.2.1	Habitability	19
4.3	Orbits of the Trojan Twin Planets	20
5	Stability of Astrodynamical Systems	23
5.1	Resonances	23
5.2	Instabilities in Trojan Twins Planets	24
5.3	Stability Indicators	25
5.3.1	Maximal Relative Eccentricity	25
5.3.2	Logarithmic Semi-Major Axis-Ratio $\ln(a)$	27
5.3.3	Comparison of e_{max} and $\ln(a)$	27
6	Lyapunov Indicator	31
6.1	Introduction to LCE	31
6.2	N-Body Integration with Lie-Series	33
6.3	MLCE via Mapping	35
6.4	MLCE via Hamiltonian	36
6.5	Application of MLCE-Algorithm on Standard Map: Mapping-Approach	36
6.6	Application of MLCE-Algorithm on Lie-Series N-Body Integrator: Mapping-Approach	39
6.6.1	Derivatives of Lie-Series-Recursions	39
6.6.2	Derivatives of Spatial Components	39
6.6.3	Derivatives of Velocity Components	39
6.6.4	Derivatives of Order Zero and One	40

6.6.5	Derivative of Lie-Series	41
6.7	Application of MLCE-Algorithm on Henon-Heiles System: Hamiltonian-Approach	41
6.8	Hamiltonian of N-Body System	46
6.9	Application of MLCE-Algorithm on N-Body System: Hamiltonian-Approach	47
6.10	Application of Hamiltonian-Approach on Trojan Twin Planets	48
6.11	Conclusions	51
6.11.1	Mapping-Approach	51
6.11.2	Hamiltonian-Approach	52
6.11.3	Comparison of the Two Approaches	52
7	Results	53
7.1	Integration Time	53
7.2	Grey Area	55
7.3	Long Term Stability	57
7.4	The Valley of Stability	59
7.5	High Mass Twins	63
7.6	Change of the Semi-Major Axis of Gas-Giant	64
7.7	Change of the Gas-Giants Eccentricity	67
7.8	Additional Gas-Giant	69
7.9	Fractal Structures	70
8	Conclusion	73
8.1	Lyapunov Indicator	73
8.2	Trojan Twin Planets	73

Abstract

Aims: In this master's thesis a special astrodynamical system will be studied, the Trojan twin planets. It consists of two terrestrial planets located around the Lagrangian point $L4$ of a gas-giant. The crucial parameters characterizing this system are the angular separation dm , the total mass of the Trojans $M_{tot} = M1 + M2$ as well as the Trojan's mass-ratio $MR = \frac{M1}{M2}$. In order to study the system's stability, different stability indicators are introduced. This defines a second goal of the thesis which consists of developing a code capable of calculating the Lyapunov indicator for a n-body system.

Means: The method of studying the stability of the Trojan twin planets consists primarily of simulations to solve the equations of motion of the n-body problem. A Lie-series n-body integrator is used to perform these calculations as well as to conduct parameter studies. This includes both the analysis of individual trajectories and the calculation of stability maps which are also called initial condition plots. There are two possible ways of calculating the Lyapunov indicators. The first approach considers the explicit form of the n-body integrator which in this case is the Lie-series integrator while the second approach is independent of the n-body integrator.

Results: It was found that the Trojan twin planets have an astonishingly broad range of stable parameters. Consider Trojan twins with masses around M_{Earth} located in the Lagrangian point $L4$ of a host planet with a semi-major axis of $1AU$. It turns out that such a system can be stable for more than hundred million years.

The stable angular distance is proportional to the cubic root of the total mass of the Trojans ($dm \propto M_{tot}^{1/3}$). A slight deviation from this relation is explained by different mass-ratios (MR) of the twins. Increasing the mass up to several Jupiter masses the system can remain stable for more than $2 \cdot 10^4$ years. This duration corresponds to the same number of periods of the planets motion around the host star.

Since planetary systems are often inhabited by more than one gas-giant, the Trojan twin planets stability with a perturbing gas-giant added is analyzed. The results show that mean motion resonances play a major role in the stability of the Trojan twin planets. No significant destabilizing effects are observed for an additional gas-giant of mass $M_{Jupiter}$ and with a semi-major axis of $a > 2.5AU$.

High resolution studies of the stability border in the initial condition plot revealed fractal structures. It turns out that the mass-ratio of the Trojan twins has the biggest influence on the form of the structures. The initial condition plot for $MR > 1$ includes spike-like structures whereas $MR < 1$ leads to wing-like structures.

It was possible to calculate Lyapunov indicators for two different problem types (Hamiltonian systems and mappings). The mapping-approach was successfully applied to the standard map where it was possible to distinguish between stable and chaotic behavior. In the case of Hamiltonian systems it was shown that the local Lyapunov histograms provide information about the system's stability. Studies on the Henon-Heiles system were used as a test-case

for the more complex general n -body Hamiltonian. The successful application of the Hamiltonian-approach was demonstrated on the Trojan twin planets.

1 Introduction

The Thesis consists of two major tasks. The first one is the dynamical analysis of the Trojan twin planets which is a special dynamical system where two terrestrial Trojans, having non-negligible masses, inhabit one of the triangular Lagrangian points of a gas-giant. The second task is the development of a code for the calculation of the Lyapunov indicator for a n-body system.

We begin with a discussion of the restricted three-body problem (r3bp) including the derivation of analytical solutions called Lagrangian points. Objects found in the Lagrangian points $L4$ and $L5$ are named Trojans. They can also be found in many orbits of solar system planets, in particular Jupiters orbit.

The subsequent section discusses the Trojans in detail. Important theories of the origin of the Trojans are presented. However, the numerical studies are only conducted on already formed Trojan twin planets. Analytically derived limits of the stability Trojans are discussed.

Finally, Trojan twin planets are introduced and the ideal parameters in terms of masses and orbital elements for the system are chosen systematically in consideration of possible habitability. Simulations aimed to analyze the motion of the Trojan twins around $L4$ also found connections to the mass-less r3bp.

In order to study the stability of a configuration, one section is dedicated to the stability of astrodynamical systems. After a theoretical treatment of resonances the special destabilization mechanism of the Trojan twin planets is portrayed. Two stability indicators are introduced and a comparison of their ability to detect stable and unstable configurations is conducted.

Another stability indicator is the so-called Lyapunov indicator which is treated in the adjoining chapter. This section is separated into two parts. The first part deals with the theoretical introduction to the Lyapunov exponent while the second part concerns the application to different systems. Two approaches for the calculation of the Lyapunov indicator, the mapping-approach and the Hamiltonian-approach, are discussed in terms of their applicability to the Lie-series n-body integrator. The mapping-approach is then applied to the standard-map, an exceptionally well studied dynamical system, whereas the Hamiltonian-approach is initially tested for the Henon-Heiles system, a simple 4-dimensional Hamiltonian system.

The success of these calculations is opening the doors towards the computation of the Lyapunov indicator for the general n-body system. The Hamiltonian-approach is not only applicable to the Lie-series n-body integrator but to all gravitational n-body codes. The last segment of this chapter consists of applying the Lyapunov indicator calculations to the Trojan twin planets and testing the functionality of this indicator in comparison to already introduced stability indicators.

The major results concerning the Trojan twin planets are presented in the next section. A time truncation error analysis is conducted, ensuring that good results for the stability indicator can be achieved within reasonable integration times. In addition the stability border in the initial condition plots is studied. At the border,

regions where stable and unstable configurations are mixed, can be observed which we call "grey area".

Long term stability is relevant especially if habitability is considered. For this reason long time integrations of more than a hundred million years are conducted. The stable configurations are chosen through the "valley of stability", a stripe of exceptional stable configurations in the $dm - M_{tot}$ -initial condition plot.

Another study of significance is the search for the upper mass limit of stable configurations. Simulations of Trojan twins with masses of several Jupiters are carried out to study the stability of such extreme cases. To characterize the Trojan twin planets' robustness, the change of the gas-giants semi-major axis and its effect on the stability is analyzed. A comparison to the r3bp and escape orbits, found in plots with changes of the semi-major axis of the Trojans, is drawn showing the strong connection between the r3bp and the Trojan twin planets.

A similar study on the change of the gas-giants eccentricity is realized. Since many planetary systems show the presence of more than one gas-giant, the influence of an additional gas-giant in the outer region of the system is examined. Here, the focus is set on mean motion resonances leading to destabilizing effects.

Many chaotic systems show fractal behavior. For this reason high resolution initial condition plots are analyzed to identify possible fractal structures. The influence of the mass-ratio (MR) is analyzed in detail.

2 Restricted Three-Body Problem

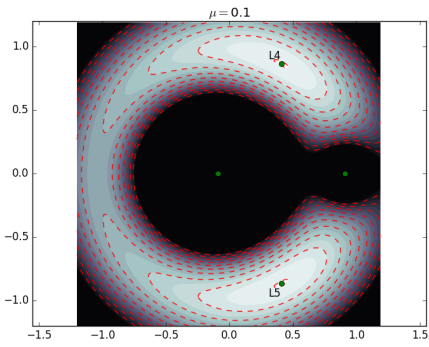
The restricted three-body problem (r3bp) is a well understood dynamical problem. Two of the three bodies are considered having non-negligible masses $M_1, M_2 > 0$, whereas the third body is mass-less ($M_3 = 0$). Many famous mathematicians and astronomers have worked on the r3bp including Leonhard Euler (1707-1783), Joseph Lagrange (1736-1813) and Jakob Jacobi (1804-1851). A distinction between the circular and the elliptical three-body problem can be made. In this thesis only the circular r3bp will be treated.

2.1 Potential of Circular R3BP

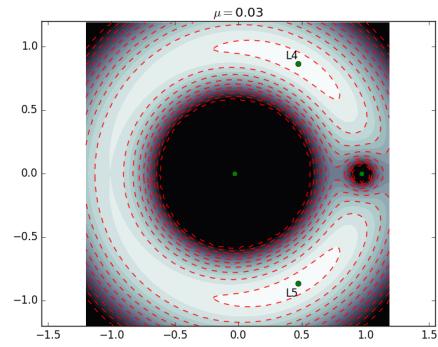
If we consider the three-body problem in the rotational frame of the two massive bodies with coordinates r_1 and r_2 the potential acting upon the mass-less third body with the coordinates (x, y) can be explicitly written as follows:

$$V = -\frac{GM_1}{\sqrt{(x-r_1)^2 + y^2}} - \frac{GM_2}{\sqrt{(x-r_2)^2 + y^2}} - \frac{1}{2}\Omega^2 r^2 \quad (1)$$

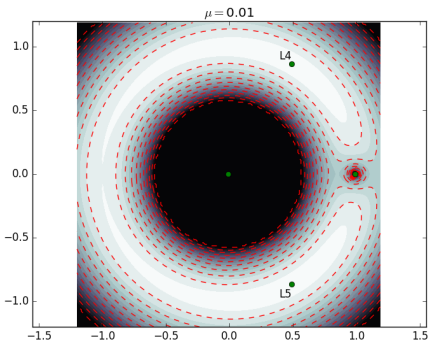
The potential function is not depending on time since the moving third body does not gravitationally interact with the two massive bodies. In the co-rotating frame no relative motion between the two massive bodies occurs as circular orbits are assumed. The effective potential in equation 1 consists of two terms, one considering the gravitational interaction of the massive bodies on the third body and the other term for correcting the co-rotating frame with a angular velocity Ω where $r = \sqrt{r_1^2 + r_2^2}$. Figure 1 shows the effective potential of the r3bp for different mass-ratios $\mu = \frac{M_1}{M_2}$. By choosing the right time units a co-rotating coordinate system with a rotation period of unity can be achieved. An unit system is chosen in such a way that $M_1 = 1 - \mu$ and $M_2 = \mu$ with $\mu = \frac{M_2}{M_1}$. Hence $M_1 + M_2 = 1$ holds. The unit of length is chosen in such manner that the radii are equal to the masses of the bodies.



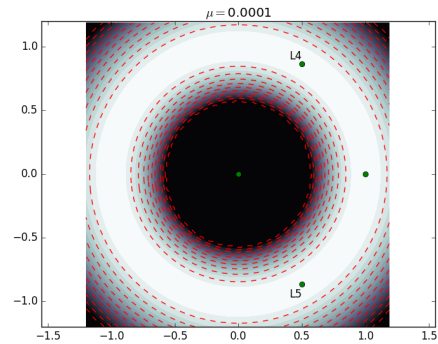
(a) Effective r3bp potential for $\mu = 0.1$



(b) Effective r3bp potential for $\mu = 0.03$



(c) Effective r3bp potential for $\mu = 0.01$



(d) Effective r3bp potential for $\mu = 0.001$

Figure 1: This figure shows the effective potential of the r3bp (equation 1) for different mass-ratios $\mu = \frac{M_2}{M_1}$. The red dotted lines represent equipotential lines. The form of the equipotential lines of the effective potential strongly depends on the mass-ratio of the two massive bodies. Characteristic tadpole equipotential lines are formed around the Lagrangian points $L4$ and $L5$. When choosing smaller mass-ratios we observe that the tadpole structures get more elongated forming so called horse-shoe equipotential lines. In the limit of $\mu \rightarrow 0$ the asymmetric deformation of the potential vanishes and a radial symmetric potential is obtained.

2.2 Solution of the Circular R3BP

The Lagrangian points $L1$, $L2$ and $L3$ were initially described by Leonhard Euler in the year 1767 and triangular Lagrangian point for the first time by Lagrange in 1772 ([15]). This section follows the calculations from Dvorak and Lhotka ([16]) in order to derive the Lagrangian points. A unit system as well as the coordinate system to conveniently handle the r3bp is introduced. The first body has the mass M_1 and the second body M_2 . Additionally, reduced masses are introduced: $\mu_1 = \frac{M_1}{M_1+M_2}$, $\mu_2 = \frac{M_2}{M_1+M_2}$. The mass units are chosen in a way that $\mu_1 + \mu_2 = 1$, hence $\mu_1 = 1 - \mu$ and $\mu_2 = \mu$ holds. The distance between the two massive bodies l as well as

the gravitational constant are set to unity. The angular frequency takes the form $\omega = \sqrt{\frac{(1-\mu)+\mu}{I^3}}$ and the value 1. The effective potential can be seen in equation 2 where $r_1 = (x + \mu_2)^2 + y^2$ and $r_2 = (x - \mu_1)^2 + y^2$.

$$\Omega = \mu_1 \left(\frac{r_1^2}{2} + \frac{1}{r_1} \right) + \mu_2 \left(\frac{r_2^2}{2} + \frac{1}{r_2} \right). \quad (2)$$

Since we want to find stable points in the potential of the r3bp we form the spatial derivatives of the effective potential as seen in equation 3.

$$\frac{\partial \Omega}{\partial x} = \frac{\partial \Omega}{\partial r_1} \frac{\partial r_1}{\partial x} + \frac{\partial \Omega}{\partial r_2} \frac{\partial r_2}{\partial x} = 0 \quad (3)$$

$$\frac{\partial \Omega}{\partial y} = \frac{\partial \Omega}{\partial r_1} \frac{\partial r_1}{\partial y} + \frac{\partial \Omega}{\partial r_2} \frac{\partial r_2}{\partial y} = 0$$

$$\frac{\partial \Omega}{\partial x} = \mu_1 \left(r_1 - \frac{1}{r_1^2} \right) \frac{\mu_2 + x}{r_1} + \mu_2 \left(r_2 - \frac{1}{r_2^2} \right) \frac{x - \mu_1}{r_2} = 0 \quad (4)$$

$$\frac{\partial \Omega}{\partial y} = \mu_1 \left(r_1 - \frac{1}{r_1^2} \right) \frac{y}{r_1} + \mu_2 \left(r_2 - \frac{1}{r_2^2} \right) \frac{y}{r_2} = 0$$

We immediately find two solutions of the equations 4. For $r_1 - \frac{1}{r_1^2} = 0$ and $r_2 - \frac{1}{r_2^2} = 0$ the equations are fulfilled. This is the case for $r_1 = r_2 = 1$. When recalling that the distance between the two bodies $l = 1$ we see that an equilateral triangle constellation is formed. This is possible for positive and negative y . The first body has the position $(-\mu, 0)$ and the second body $(1-\mu, 0)$ in the coordinate system. This gives the positions of the stable solutions at $(\frac{1}{2} - \mu, \sqrt{3}/2)$ and $(\frac{1}{2} - \mu, -\sqrt{3}/2)$. These points are denoted as L4 and L5 respectively. Via condition 5 further minima are found. The condition is fulfilled for $y = 0$.

$$\det \begin{pmatrix} \frac{\partial r_1}{\partial x} & \frac{\partial r_2}{\partial x} \\ \frac{\partial r_1}{\partial y} & \frac{\partial r_2}{\partial y} \end{pmatrix} = \frac{y(\mu_1 + \mu_2)}{r_1 r_2} = \frac{y}{r_1 r_2} = 0 \quad (5)$$

Plotting the effective potential (figure 2) reveals that three more minima can be found along $y = 0$.

- L1 for interval $-\mu_2 < x < \mu_1$
- L2 for interval $x > \mu_1$
- L3 for interval $x < -\mu_2$

2.2.1 Lagrangian Point L1

The distance to the first body is $r_1 = x + \mu_2$ hence $r_2 = 1 - r_1$. The partial derivatives are then $\frac{\partial r_1}{\partial x} = 1$ and $\frac{\partial r_2}{\partial x} = -1$. Equation 3 gives the new condition seen in equation

6. Lets define $\lambda = r_2/r_1 = \frac{1-r_1}{r_1}$ and replace r_1 and r_2 in equation 6 and we find equation 7, which has to be solved to find the x-value of the position of $L1$.

$$\frac{\partial \Omega}{\partial r_1} - \frac{\partial \Omega}{\partial r_1} = 0 \quad (6)$$

$$\frac{\mu_2}{\mu_1}(1 + 3\lambda + 3\lambda^2) - 3\lambda^3 - 3\lambda^4 - \lambda^5 = 0 \quad (7)$$

The solution for λ is obtained by a series expansion of λ and solving for the coefficients. This gives equation 8 where $\lambda_0 = \sqrt[3]{\mu_2/(3\mu_1)}$.

$$\lambda = \lambda_0 + \frac{2}{3}\lambda_0^2 + \frac{2}{9}\lambda_0^3 - \frac{32}{81}\lambda_0^4 + O(\lambda_0)^5 \quad (8)$$

2.2.2 Lagrangian Point L2

For $L2$ it holds that $r_1 = x + \mu_2$ and $r_2 = r_1 - 1$, which gives the condition in equation 9. We introduce $\lambda = \frac{r_1-1}{r_2}$ and again replace r_1 and r_2 . By solving equation 10 the position of $L2$ is obtained.

$$\frac{\partial \Omega}{\partial r_1} + \frac{\partial \Omega}{\partial r_1} = 0 \quad (9)$$

$$\lambda^3(3 - 3\lambda + \lambda^2) + \frac{\mu_2}{\mu_1}(2\lambda - 1)(1 - \lambda + \lambda^2) = 0 \quad (10)$$

For λ we get the solution with equation 11 where again $\lambda_0 = \sqrt[3]{\mu_2/(3\mu_1)}$.

$$\lambda = \lambda_0 + \frac{1}{3}\lambda_0^2 - \frac{1}{9}\lambda_0^3 - \frac{31}{81}\lambda_0^4 + O(\lambda_0)^5 \quad (11)$$

2.2.3 Lagrangian Point L3

The third Lagrangian point is found at $r_1 = -x - \mu_2$ and $r_2 = r_1 + 1$. Via the partial derivatives we find the same condition as for $L2$ seen in equation 9. By using $\lambda = \frac{r_1+1}{r_1}$ we get equation 12.

$$(-1 + 3\lambda - 3\lambda^2)\frac{\mu_2}{\mu_1} - 2\lambda^2 + 3\lambda^3 - 3\lambda^4 + \lambda^5 = 0 \quad (12)$$

Solving for λ we find 13.

$$\lambda = 1 + \frac{7}{12}\frac{\mu_2}{\mu_1} - \frac{35}{144}\left(\frac{\mu_2}{\mu_1}\right)^2 + \frac{3227}{20726}\left(\frac{\mu_2}{\mu_1}\right)^3 + O\left(\frac{\mu_2}{\mu_1}\right)^4 \quad (13)$$

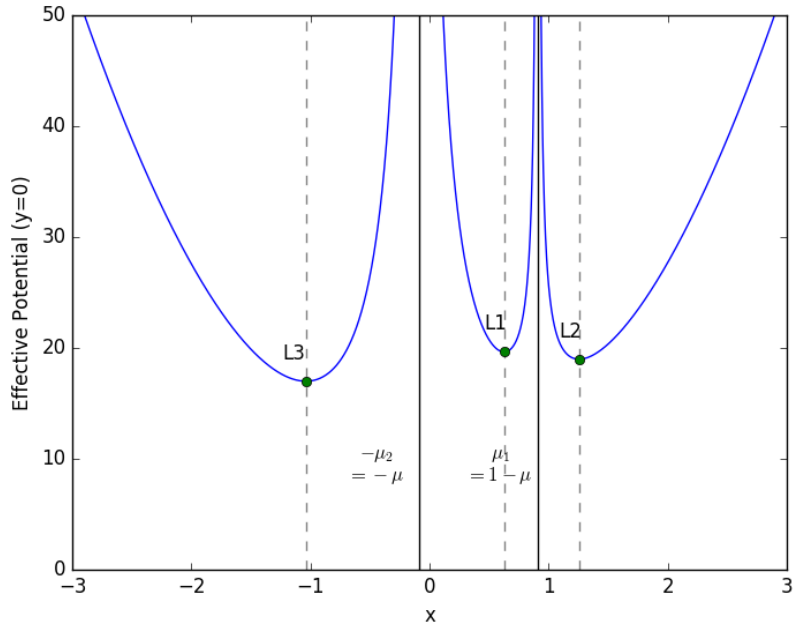


Figure 2: For a fixed value of $y = 0$ we can see the Lagrangian points $L1, L2, L3$ as minima of the effective potential of the r3bp. This plot was created for a mass-ratio of $\mu = 0.1$. The positions of the massive bodies are labeled by solid lines according to their x -position, whereas the the Lagrangian points are labeled by dashed lines.

3 Trojans

Trojans are celestial objects which are librating around the Lagrangian points $L4$ or $L5$, called triangular Lagrangian points. This means they have the same semi-major axis as the massive planet. We have seen that these triangular points are found $\pm 60^\circ$ apart from the planet on its orbit. We will now discuss some observations of Trojans in the solar system. Terminologically the word "Trojan" is a relict of history [19]. The first discovered Trojan objects of Jupiter were named after heroes of Homers "Iliad". All bodies of Jupiter's $L4$ are named after participants on the Greek side of the Trojan war, except for 624 Hektor who was a prince of Troy. 624 Hektor is not only the biggest Trojan (sphere diameter $\approx 250km$) of Jupiter but also the first and to date only one with a satellite [29]. This is the reason why Jupiter's $L4$ -Trojans are called "Greeks". The bodies in Jupiter's $L5$ are called "Trojans" due to the naming of the bodies after participants of the Trojan war on the Trojan side. Another misnaming occurs since 617 Patroclus was brother in arms of Achilles and should, following the convention, be part of the "Greeks". The term Trojan in respect to Jupiter is hence a hypernym of "Greeks" and "Trojans". Jupiter is not the only planet in the solar system which has Trojan objects but by far the one with the most. The first Trojan 588 Achilles was found by Max Wolf, who is known for

his many discoveries of minor planets, in 1906 [36]. To date 7032 Trojan objects of Jupiter are known ¹.

There is an asymmetry in the number of objects found in $L4$ and $L5$. Approximately twice as many objects with diameters larger than $2km$ are found in $L4$ (6300 ± 1000 objects) as in $L5$ (3400 ± 500) [34]. The size distribution of Jupiter's Trojans is depicted in figure 3, which stems from data of the NEOWISE project, ([28]) an all sky survey designed to find NEOs (Near Earth Objects). It can be seen that the number density of the Trojan objects follows $N \propto D^{-2}$. The reason why Jupiter has so many Trojan minor planets is its gravitational dominance in the solar system. Estimations of the total number of Trojans compare it with the number of main belt objects ([40]). Nevertheless, also comparably "light" bodies Trojans have been found. For example Earth has a single known Trojan 2010 TK7 ([9]), Mars has 9 known Trojan objects. For Neptune 17 Trojans are found and Uranus has a single Trojan. Venus is a special case: In 2013 a temporary Trojan was discovered ([13]). No Trojans are found for the planet Saturn due to perturbing interactions with other planets ([19]).

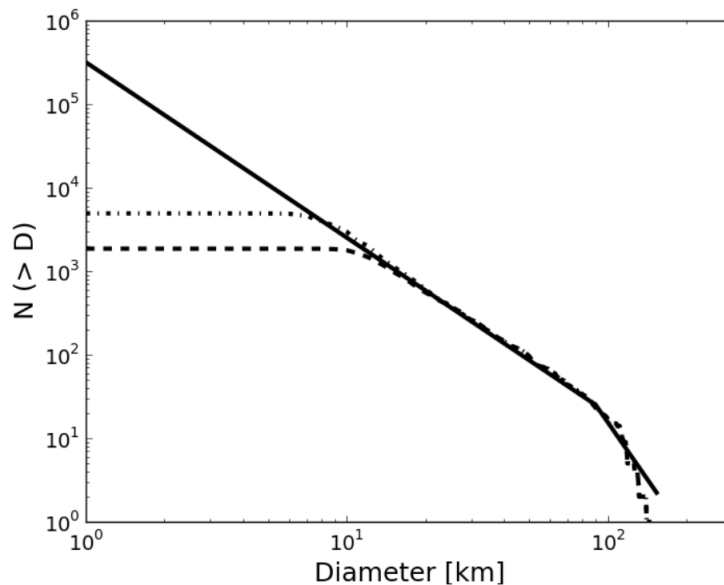


Figure 3: The size distribution of Jupiter's Trojans shows that the number density follows $N \propto D^{-2}$. The dashed line represents the NEOWISE sample ($> 20km$), the dotted line current optical surveys ($> 10km$). The solid line includes the extrapolation of the trend. Figure credit: [19].

¹<https://minorplanetcenter.net/iau/lists/Trojans.html>

3.1 The Origin of Trojans

Trojans are survivors of an initially numerous primordial population. A highly discussed issue is the origin of Trojans and their exceptional dynamics. It is therefore important to understand the processes which led to the positioning of the bodies in the Lagrangian points. By studying capture probabilities we learn about the early phase of the solar system. The composition of the Trojans can furthermore tell us much about the young solar system. When it comes to studying water transport mechanisms Trojans serve as probes of exceptional quality ([21]). The main problem is not the stability of objects in the triangular Lagrangian points but the process of capturing the bodies in the minima of the effective potential. We will discuss two main types of possible mechanisms resulting in co-orbital configurations. Following the classification of Morbidelli ([19]) the first group of processes is of non-gravitational nature. A planetesimal passes by the planet and following processes can appear:

- Gas drag hypothesis: The planetesimal drifts, due to gas drag, towards the Lagrangian point. Here smaller bodies are effected more efficiently and once they are in stable orbits the growth continues. Planetesimals around the triangular Lagrangian points would, due to the gas drag, slowly loose libration amplitude and get on more stable orbits. The approach is pictured in more detail in [37]. A problem is that the hypothesis favors more objects in $L5$ than in $L4$ for non-zero eccentricities which is contradicting the observations. Another effect that could play a key role is the Yarkovsky effect which is most significant for bodies $< 10km$.
- Fragment hypothesis: Fragments of colliding planetesimals are ejected directly into the Lagrangian points. This scenario is discussed in [40].

The second group of processes is characterized by a change in the orbit of the planet in such way that objects are now captured in the Lagrangian points.

- Slow migration hypothesis: A smooth migration of the planet sweeps with its Lagrangian points over bodies which are captured. Detailed discussion can be found in [27]. The paper is specifically working on Neptune's Trojans. A slow migration of giant planets has proven to be more effective in capturing objects and forming the observed population of Trojans from the trans Neptunian disk than a fast migration of Neptune from $\approx 23AU$ to $\approx 30AU$. In all simulations capturing efficiencies between 0.1% and 1% were found. Nevertheless, planetary disruptive events between Neptune and Uranus could, for some scenarios, lead to ejections of the Trojans.
- Jumping Jupiter hypothesis. Nesvorný et al ([35]) are using the results of the NICE-model (review in [11]). In the NICE-model Jupiter is changing its semi-major axis because of a scattering event with an ice-giant. Now the triangular Lagrangian points could be placed into a region populated with

planetesimals, which are captured. The hypothesis is capable of explaining the number asymmetry in the population of $L4$ and $L5$ ([34]). The capture probability is $(6 - 7) \cdot 10^{-7}$.

- Chaotic capture hypothesis: Morbidelli et al. ([33]) proposed another process of possible capture of Trojans based on the NICE-model. A global instability occurs when Saturn and Jupiter are in 2 : 1 resonance and hence prior inaccessible regions in the solar system become accessible. A so-called "chaotic path" is opened. Such region are e.g. the triangular Lagrangian points. When the path is opened the $L4$ and $L5$ regions can be accessed by planetesimals. Due to the ongoing migration at some point the chaotic path is closed and the objects passing the Lagrangian point remain captured.
- Planetary mass accretion hypothesis: Marzari et al. ([30]) proposed another process of capturing Trojans. In the early phase of planetary evolution we can assume a planetesimal disc. One object becomes gravitationally dominant and is accreting material. In figure 1 we see the effect of a changing mass of the planet on the equipotential lines. With increased mass tadpole structures are formed from an initially - at small masses - nonexistent substructure. Rapidly increasing mass of the planet can hence trap planetesimals in the triangular Lagrangian points.

It is most probable that some or all of the above processes in combination are responsible for the creation of co-orbital objects ([31]).

3.2 Motion of Trojans around Triangular Lagrangian Points

Lagrange not only found the solution for the Lagrangian points, he also analyzed the motion of a mass-less test body around the triangular Lagrangian points for small deviations. The motion of the body in the Lagrangian points can be described by a superposition of two motions on ellipses with different periods. Figure 4 shows the epicyclic motion pattern around $L4$. It is possible to express the periods of the motion with help of the reduced masses and the period of the giant planet ([30]). Equations 14 and 15 describe the period of the first order libration and the period of the second order libration respectively. In order to be applicable, the condition $\mu < \mu_{crit} \approx 0.0385$ has to be fulfilled.

$$T_1 = \frac{T_J}{\sqrt{(27/4)\mu}} \quad (14)$$

To give an example of the first order libration period of a Trojan for a Jovian planet ($\mu = 10^{-3}$) at $1AU$ is $T_1 = 12.17$ years. The second order libration period is $T_2 \approx 1year$.

$$T_2 = \frac{T_J}{\sqrt{1 - (27/8)\mu}} \quad (15)$$

Another interesting fact is that one can show that the axis-ratio of the ellipses of the first order libration is $\sqrt{3\mu}$ whereas the ellipse of the motion of the second order has an axis-ratio $1/2$.

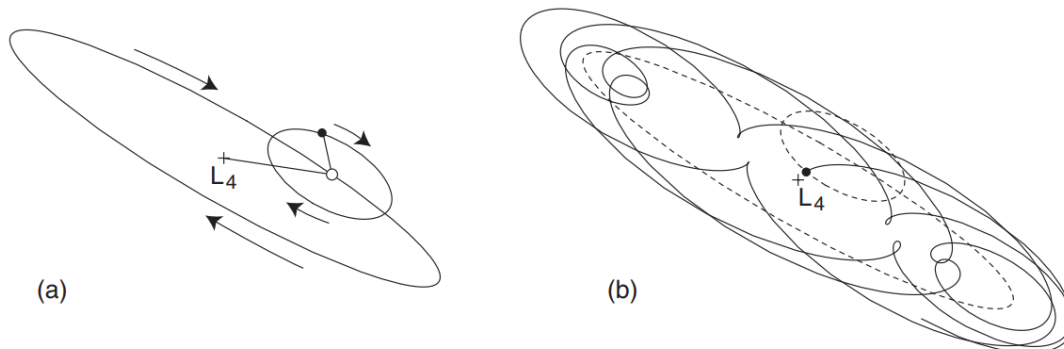


Figure 4: If a Trojan is nearby one of the triangular Lagrangian points the motion in the co-rotating frame is described by the superposition of the movement of two epicyclic ellipses with distinct periods. This leads to complicated orbits, as the right figure shows. Figure credit: [30].

3.2.1 Tadpole and Horseshoe Orbits

The solutions with the superposition of the two elliptic motions are only true for motions near the Lagrangian points and only for small amplitudes of the motion. For more extended motions we must rely on numerical simulations. If the body is initially positioned around L_4 or L_5 the body performs a motion on a so called tadpole orbit. The name stems from the elongated form of the orbit and its head structure which resemble the larvae of some amphibians ([8]). The tadpole orbit is elongated on the opposite side of the second body (the gas-giant) and shortened towards the second body. Hence the orbits are symmetric in terms of horizontal mirroring (x-axis). If we recall the shape of the equipotential lines of the effective potential of the r3bp in figure 1 we observe that the tadpole orbits which are depicted in figure 5, resemble the form of the equipotential lines. Please note that the orbits and the equipotential lines are not the same but strongly connected. The form of the tadpole orbits heavily depends on the initial positioning of the Trojan. In figure 5 the two charts show the orbits of two configurations only differentiated by a slight change in the initial position of the Trojan around L_4 . Nevertheless, the orbits show completely different shapes. Another possibility of a 1:1 resonant orbit is the horseshoe orbit. Again the study of the equipotential lines in figure 1 can anticipate the existence of such orbits. Two examples of horseshoe orbits are portrayed in figure 6. In this case the motion of the Trojan is not limited to a single triangular Lagrangian point but it extends in the co-rotating frame almost

to the whole orbit of the Jovian planet. Horseshoe orbits are numerically achieved by placing the object in the vicinity of L_3 , which is near the opposite place of the planet on the orbit.

A special and interesting example for a horseshoe orbit is the co-orbital configuration of the Saturn moons Janus and Epimetheus. The dynamics of the system are analyzed in Llibre and Olle ([26]). The semi-major axis of the moons are only separated by $50km$. This means that a collision of the moons is expected due to the slightly different orbital velocities and the radii of the objects (Janus: $\approx 90km$ ([43]), Epimetheus: $\approx 60km$ ([43])) being greater than their separation. Nevertheless, the bodies do not collide but swap their orbits when getting closer than approximately $10000km$. [26] showed that the observed behavior is closely connected to the r3bp and is sufficient to reproduce similar results numerically. This is astonishing since the r3bp neglects the mass of one moon. Only Janus was assumed to have a mass of $\mu = 3.5 \cdot 10^{-9}$. Furthermore an eccentricity $e = 0.0$ was assumed which is a good approximation since the eccentricity of Janus is 0.068 ([42]). A further example for an object with Trojans with horseshoe orbits is the earth. In 2016 five quasi-satellites of the earth were known. Interestingly, all five switch from quasi-satellite orbits to horseshoe orbit periodically ([14]).

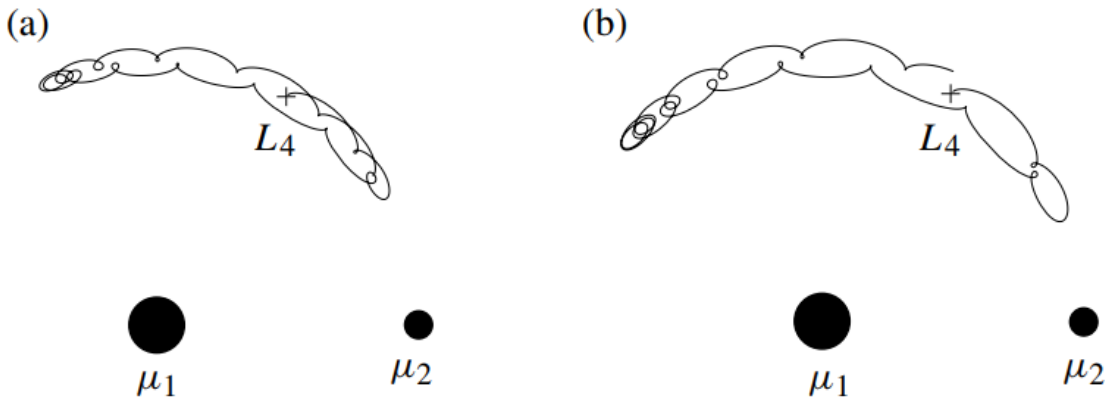


Figure 5: This figure shows two examples of tadpole orbits for slightly different initial conditions. Both examples have starting points near the Lagrangian point L_4 and $\mu = 0.001$. Figure credit: [8] p.97.

3.3 Exo-Trojans and Trojan Planets

Due to the numerous observations of Trojans in our solar system not only for Jupiter but for most of the planets it is almost certain that exoplanetary systems have similar objects. A problem of exo-Trojan detection is that Trojans normally have a high mean inclination ([45]) which makes it hard to find them via the transit method - the most commonly used exoplanetary detection method. [22] suggests

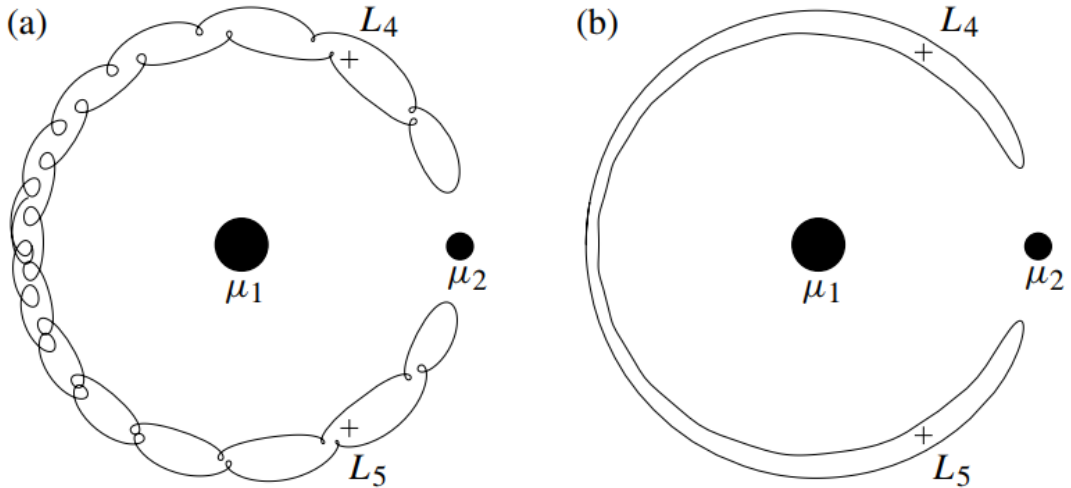


Figure 6: Depicted are two examples of a horseshoe orbit for different initial conditions. We observe that in this special case the motion of the body is no longer only restricted to the vicinity of a single Lagrangian point. Figure credit: [8] p.98.

that with upcoming PLATO 2.0 ([20]) it should be possible to detect Trojans which are $> 0.5R_{Earth}$ as a byproduct of planetary search.

3.3.1 Mass Limit for a Trojan Planet

The question arises how bodies with masses of terrestrial planets in the triangular Lagrangian points are formed. A possible answer is given by Beauge et al. ([3]). In the paper the initial condition is that many planetesimals are trapped in the Lagrangian points of a star-gas-giant configuration. The possible capture mechanisms leading to this configuration have already been discussed extensively. The planetesimals are merging supported by the gas, which is present due to the early phase of the planetary system's evolution and exhibits drag on the bodies. When the mass of the giant exceeds a critical mass a gap in the gas disc opens and consequently the further evolution of the Trojan objects lacks of a gaseous environment. This is the reason why both non-gas and gas-environment scenarios have to be tested. Beauge et al. placed 100 to 1000 equal mass bodies with a total mass of $1 - 3M_{Earth}$ in a wide range of initial conditions around one of the triangular Lagrangian points. The findings are that there is a mass limit for the formation of terrestrial planets in the Lagrangian points. It was not possible to create planets with masses higher than $0.6M_{Earth}$. It was also found that the introduction of hydrodynamics and gas did not change the maximal achieved masses for the terrestrial planet. The conclusion is that it can be expected to find a terrestrial planet as Trojan planet of a gas-giant. In exceptional configurations even an extreme mass of the Trojan planet can form a stable system. Laughlin and Chambers ([25]) showed that it is possible that a

Trojan planet is as massive as the gas-giant itself - if $\mu = \frac{2M_{pl}}{2M_{pl}+M_{star}} < 0.03812$ is fulfilled. It is hence possible to create 1:1 resonances with two identical gas-giants. These configurations are astonishingly robust and even migration processes do not destabilize the configuration.

4 Trojan Twin Planets

The planetary bodies which are subjects of the master's thesis are the so-called Trojan twin planets. The system consists of 4 bodies in total. The central object, a gas-giant and two Trojan planets with non-negligible masses. The Trojans are initially positioned barycentrically around the Lagrangian point L_4 . A schematic representation of the system is given by figure 7. In many ways, the system is a complication of the restricted three-body problem. The first task is to find the similarities to the simplified dynamical system, especially discussing the stability limits of the Lagrangian points. The next step is then pinning down the most important parameters for the system to finally conduct the numerical experiments. Figure 7 shows the basic geometry of the problem.

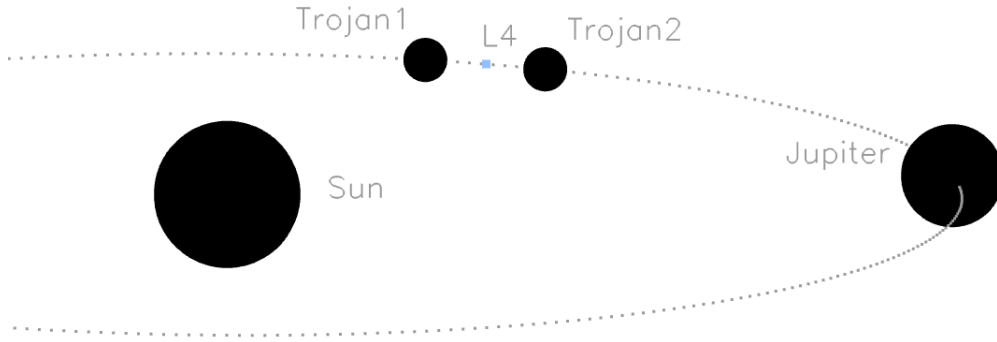


Figure 7: This figure depicts the configuration of the Trojan twin planets. The twins are positioned barycentrically around the Lagrangian point L_4 . The Jupiter is on a circular orbit at a distance of $1AU$.

4.1 From R3BP to Twin Trojan Planets

The r3bp includes the important assumption that the third body is mass-less. Without the assumption the problem is not analytically solvable. Nevertheless, we want to use its solutions to describe the behavior of the Trojan objects, which are in fact not mass-less. An estimator of how well the assumption of mass-lessness is fulfilled is the ratio of the masses of the Trojans and the Jovian planet. To estimate this quantity for the solar system's Jupiter we use the cumulative mass of the Trojan objects which is $\approx 2 \cdot 10^{-10} M_{Sun}$ for L_4 Trojans of Jupiter ([44]). This gives a ratio

of $2 \cdot 10^{-7}$. In the case of a Trojan planet of earth mass it would be $3.14 \cdot 10^{-3}$, which is significantly higher. Aforementioned estimation hence can not be used in our case to give estimates on the stability of a possible Trojan planet. We can apply the criterion of Routh from equation 16 ([18]), which when fulfilled, provides stable solutions for the triangular Lagrangian points. In the case of gravitational interaction $\kappa = 2$ and the right side of the equation becomes $1/27$.

$$\gamma < \frac{1}{3} \left(\frac{3 - \kappa}{1 + \kappa} \right)^2 = \frac{1}{27} \quad (16)$$

where

$$\gamma = \frac{M_1 M_2 + M_1 M_3 + M_2 M_3}{(M_1 + M_2 + M_3)^2} \quad (17)$$

We can assume that $M_1 \gg M_2$ and $M_1 \gg M_3$, where M_1 is the mass of the star, M_2 is the planet forming the Lagrangian points and M_3 is the Trojan. We explicitly do not demand $M_2 \gg M_3$. Linearizing equation 17 with these assumptions gives a simplified expression for γ , as seen in equation 18.

$$\gamma \approx \frac{M_2 + M_3}{M_1 + 2M_2 + 2M_3} \approx \frac{M_2 + M_3}{M_1} \quad (18)$$

Under assumption of $M_1 \gg M_2, M_3$ a much simpler expression for Routh's criterion in equation 19 is obtained. This allows us to investigate the upper mass limit of a Trojan planet. Interestingly, the criterion is independent from the mass-ratio of the planets. It allows configurations where the bodies 2 and 3 are of the same mass. This coincides with the numerical findings of Laughlin and Chambers ([25]), where a gas-giant inhabits another gas-giant in its Lagrangian points. It is therefore indeed expected to find similar solutions for massive bodies as Trojans as found in the r3bp. For the specific application of the stability criterion on the Trojan twin planets we have another additional variable. The first assumption for finding an upper limit is to substitute M_3 in equation 19 with the sum of the twin planets masses $M_3 + M_4$. No arguments speaking against the existence of stable solutions with two terrestrial planets captured in the same triangular Lagrangian point have been found yet.

$$\frac{M_2 + M_3}{M_1} < \frac{1}{27} \quad (19)$$

4.2 Restrictions on the Parameters

This section has the purpose of justifying the choices of the most important parameters. The goal of the thesis is to investigate the possibility of Trojan twin planets of terrestrial composition. The first parameters which we want to determine are the mass of the host star, the mass of the planet in whose triangular Lagrangian point the Trojan twins are placed and its semi-major axis. The first consideration is to coarsely give an estimate for the mass of the planet forming the Lagrangian points.

Considering the solar system an observation is that the best predictor for the existence of Trojans is the mass of the planet. Therefore, the decision is that it should be a gas-giant. When taking a look at figure 8 it is found that in the mass range of a Jovian planet ($\approx 318M_{earth}$) the M - a -plane is densely populated for a large range on the semi-major axis. Since habitability is taken into account the choice of $a = 1AU$ for a solar mass star is ideal. The figure is from a numerical experiment with the goal to give estimates on the populations of planets in the M - a -diagram. The habitable zone for a solar mass star is determined by Kasting et. al. from $0.95AU$ up to $1.37AU$ ([23]). The inner edge is defined by water loss whereas the outer edge is defined by CO_2 -condensation. Therefore, we will use a star mass of one solar mass and a mass of $1_{Jupiter}$ for the giant planet due to the predicted and observed high emergence of gas-giants of similar mass at $a = 1AU$ (see figure 8).

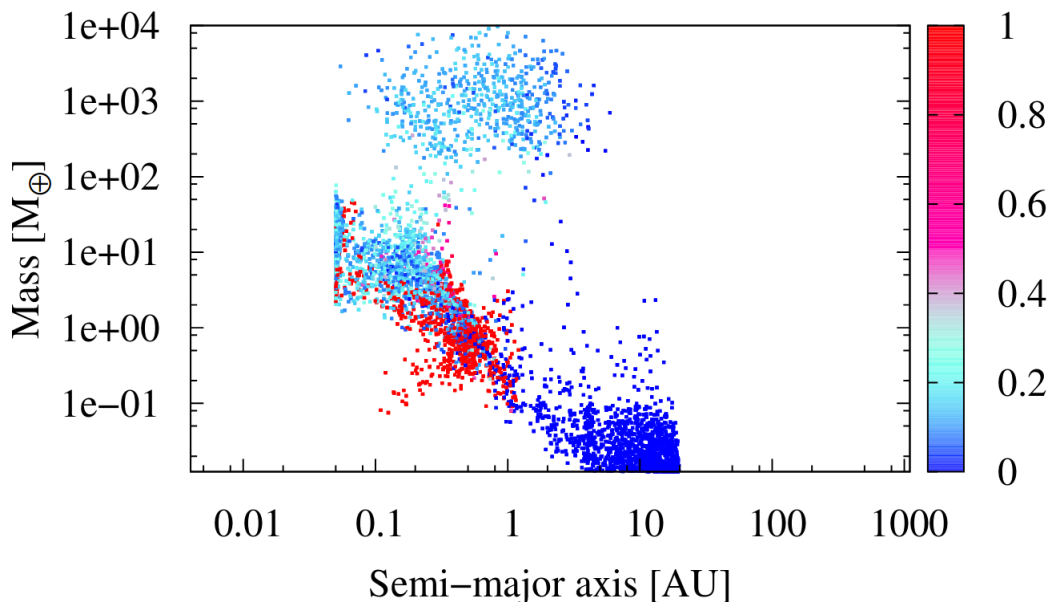


Figure 8: This plot depicts the distribution of planets in the M - a -plane achieved by numerical experiments. The color code represents the degree to which the formed planets accreted rocky planetesimals (red) or icy planetesimals (blue). The simulation was conducted for values between $0.03AU < a < 20AU$. Figure credit: [1].

4.2.1 Habitability

As soon as considering habitability more restrictions are applied on the system. One criterion for the classification as terrestrial planet is that the planets atmosphere is not a dominating part of the composition. Lammer et al. ([24]) have shown that a problem which occurs, is that heavy terrestrial planets accumulate thick hydrogen

envelopes. XUV photons from the star (G-star) are able to erode the atmosphere of the young planet for masses lower than $1M_{Earth}$. The eroding of the atmosphere is perpetuated by the heating of the gas via the photons in the ultraviolet regime of the host star. The hydrogen atoms with then high kinetic energy are capable of escaping the gravitational bound of the terrestrial planet. After the early phase of genesis the lower limit of the gas envelope of a $2M_{Earth}$ planet is given by $7.5 \cdot 10^{23}g$, which roughly corresponds to the mass of 100 earth atmospheres. This hydrogen envelope has then to be eroded in order to obtain earth-like habitable atmospheric conditions. For some cases even a $1M_{Earth}$ planet is not capable of getting rid of the massive envelope and hence staying inhabitable. An estimation of the maximal mass of the planet with a reasonably thin atmosphere (earth-like) is approximately $2M_{Earth}$. All simulations were conducted with a G-star and the planets in the habitable zone at $1AU$. The conclusion is that super earths most probably cannot lose their gas envelope, which is reducing chances for habitability. Nevertheless, in the context of the Trojan twin planets the situation is a bit more complicated. The above discussed models for the initial mass of the hydrogen envelope are estimations for isolated planets.

The specific genesis scenarios of Trojan planets can significantly differ due to interaction with the Jovian planet. A plausible assumption is the in situ genesis of the Trojans ([3]) and that the objects are depleted of gas by cannibalizing effects of the giant. The consequence of such a scenario would be that the upper limit of habitable Trojan planet's mass could be higher than that of an ordinary planet. Further investigations have to be conducted in order to verify the claims.

In addition to the upper limit of the mass a minimum mass is required in order to maintain an atmosphere. The lower limit for atmospheres are estimated to be around $1M_{Mars} = 0.107M_{Earth}$. Concerning Trojan planets it is strongly dependent on the genesis process if and how thick the gas envelope will get during the evolution of the planetary system. When looking at the list of possible formation scenarios we find that it is troublesome to give a clear answer just due to the big variations between them. A major uncertainty is whether the Trojans are captured before the vanishing of the gaseous disc in the planetary formation process. The only gaseous scenarios are the gas-drag hypothesis and planetary mass accretion hypothesis. All other scenarios described before are potentially possible in a gas free environment. A further distinction is if planetesimals are initially captured in the Lagrangian points and then accreted to a planet or if the planet is directly captured by the gas-giant. Numerical investigations are needed for the direct Trojan planet capturing process. Nevertheless, one would assume that the best scenario for a direct capture is the chaotic capture of the Jumping Jupiter hypothesis.

4.3 Orbits of the Trojan Twin Planets

The three most important parameters characterizing the system are the angular distance of the Trojan planets and their masses. We keep the mass of the gas-giant

fixed at $1M_{Jupiter}$ and the semi-major axis at $1AU$ on a circular orbit. Of great interest is the motion of the Trojan planets relative to the gas-giant. What makes the Trojan twin planets that interesting is that unlike in the restricted three-body problem there is a gravitational interaction between the two planets whilst in the r3bp two separately calculated Trojan orbits can just be superimposed. Hence we expect phenomena to occur which are unknown in the r3bp. Figure 9 shows the results of a simulation with Trojan planets of same mass ($50M_{Moon}$) at an initial angular separation of $dm = 8^\circ$ for an integration time of 100 years. For each individual planet the predicted pattern of relative motion as seen in figure 4 is observed. For this mass-ratio none of the two bodies actually touches the Lagrangian point and both libration motions have roughly the same shape. It is however not generally the case that the libration motion is of the same magnitude for both Trojans.

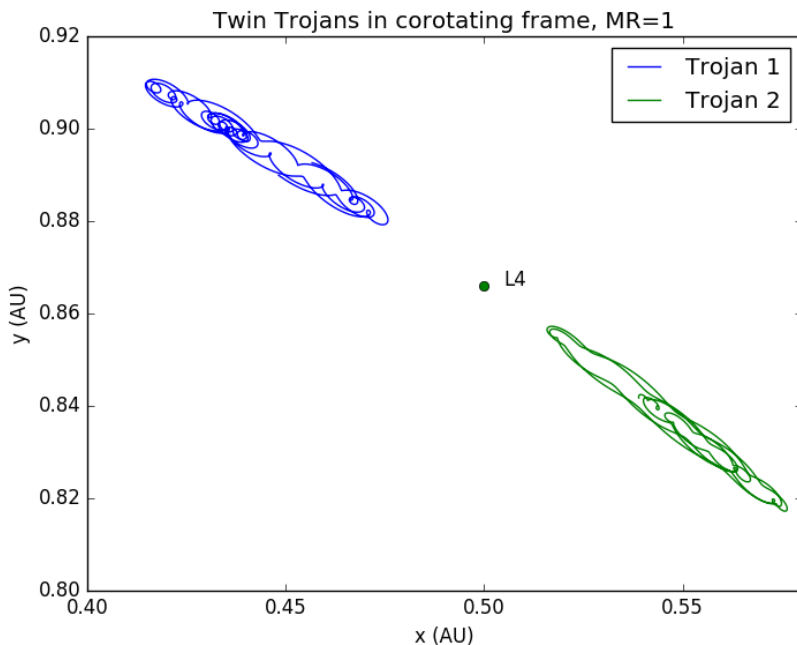
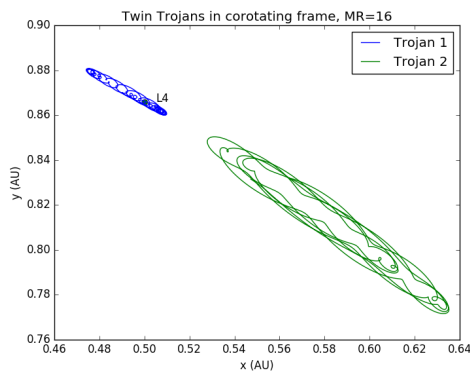


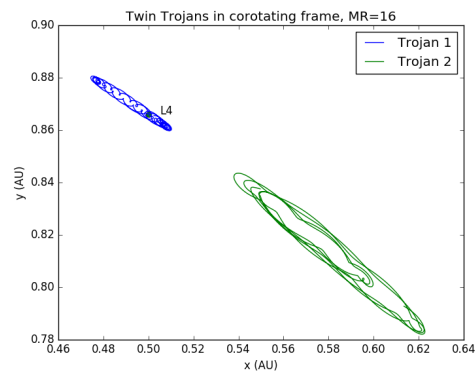
Figure 9: In the co-rotating frame of the gas-giant a separation of the accessible spacial phase space for each Trojan is observed. The simulation is conducted with a mass of $50M_{Moon}$ for each Trojan planet.

Figure 10 shows four cases where the upper two figures depict the libration motions for a $MR = 16$ and initial angular separations of $dm = 3^\circ$ and $dm = 8^\circ$ respectively. The two bottom charts are for mass-ratios of $MR = 1/16$ and the same initial angular separations. The first thing to notice is that the magnitude of the libration is higher the lighter the body is relative to the heavier one. Figure 10 a and b are clearly representing this since the libration motion of the lighter second

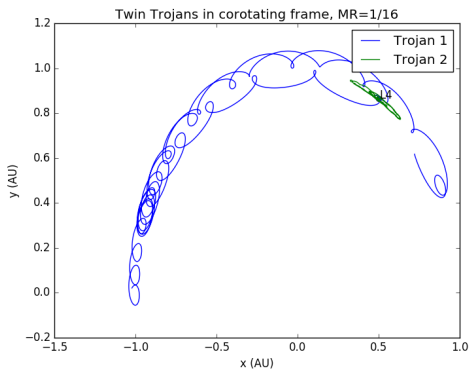
body is more prolonged. In figures c and d it can be seen that the motion of the lighter first body is very extended. For almost all depicted cases the spatial phase space separation phenomenon where each Trojan's motion in the co-rotating frame is restricted to an area distinct from the accessible area of the other Trojan is apparent. An exception is figure 10 c, where the libration motion of the first Trojan extends into the trajectory of Trojan two. Notable is that the first Trojan in this case is even reaching into Lagrangian point 3. The lighter body's libration motion is not only more elongated but also the change of the semi-major axis is more pronounced. For large extensions of the libration motion the creation of tadpole orbits as seen in figure 5 occurs. For small extensions the superposition of two motions on an ellipse seems to be accurate enough whilst still having relative motions of about 40° .



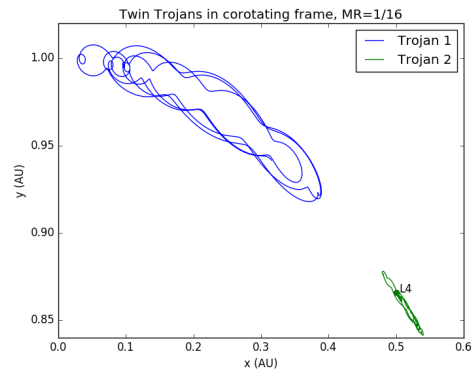
(a) $MR = 16, dm = 3^\circ$



(b) $MR = 16, dm = 8^\circ$



(c) $MR = 1/16, dm = 3^\circ$



(d) $MR = 1/16, dm = 8^\circ$

Figure 10: The libration motion of the Trojan planets changes dramatically as function of the mass-ratio (MR) as well as of the initial angular distance. All trajectories in the plots are for a simulation time of 100 years.

5 Stability of Astrodynamical Systems

In this section the tools of analyzing the stability of the Trojan twin planets are introduced. The first part gives a theoretical background of mechanisms causing instabilities, followed by a closer look at the process of body ejection in the Trojan twin system and finally the introduction of fast stability indicators is conducted. In order to provide a good visualization of the covered parameter space the initial condition plot is used. To each initial parameter combination a stability value is assigned. The two most prominent parameters are the total mass $M_{tot} = M_1 + M_2$ and the angular separation dm of the Trojans. The value of the stability indicator in the initial condition plot is represented by the color-code.

5.1 Resonances

Resonance phenomena can occur in systems with multiple planets. There are several resonant mechanisms from which the most prominent one is the mean motion resonance (MMR). In the following, a short introduction to resonances is portrayed. The main source of this chapter is Dvorak ([38]). It is useful to introduce the so-called Delaunay-variables, which are a transformation of the Keplerian orbital elements. $\Gamma_i = (L_i, H_i, G_i)^T$ describes the action variables and $\gamma_i = (l_i, h_i, g_i)$ the angular variables. The time evolution of the variables can be expressed via the Hamilton equations of motion 20 and 21.

$$\frac{d\Gamma_i}{dt} = \frac{dF_i}{d\gamma_i} \quad (20)$$

$$\frac{d\gamma_i}{dt} = -\frac{dF_i}{d\Gamma_i} \quad (21)$$

F_i is the perturbing function which is for the solution of the equations of motion evolved into a Fourier series. The solution is given by equation 22. We observe that the denominator can vanish for certain combinations of $j \cdot n_1 + k \cdot n_2$ (n is denoting the mean motion of the planet) and a big change in an orbital parameter can occur. Exactly this mechanism is called a mean motion resonance.

$$\Gamma_i = \Gamma_i^0 + \Gamma_i^1 t + \sum_{j,k \neq 0} \frac{E_{1,2}}{j \cdot n_1 + k \cdot n_2} \cos((j \cdot n_1 + k \cdot n_2)t + D_{1,2}) \quad (22)$$

By using Keplers third law (equation 23) it is possible to express MMRs with the help of the semi-major axis of the bodies, as seen in equation 24.

$$n^2 a^3 = const \quad (23)$$

$$\left(\frac{a_2}{a_1}\right)^{3/2} = \frac{k}{j} \quad (24)$$

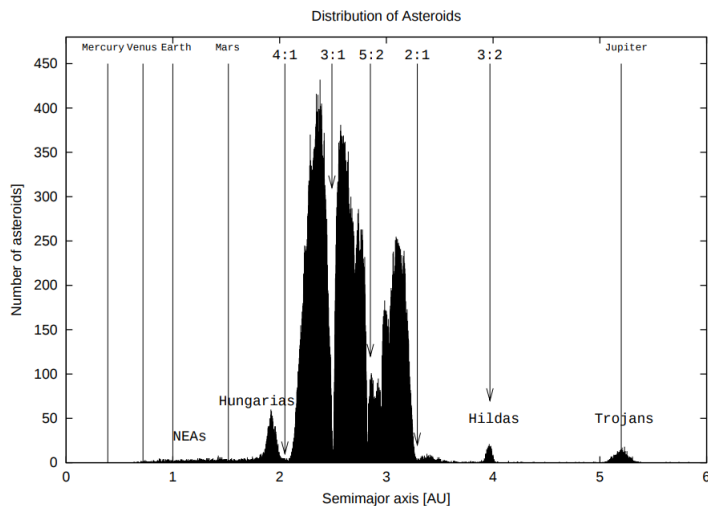


Figure 11: The distribution of asteroids in the solar system shows distinct features which are mostly caused by mean motion resonances. Very prominent feature is the so-called Kirkwood gap for which the 3:1 resonance with Jupiter is responsible. Source: [38].

Prominent examples of MMRs in the solar system are the 5:2 resonance of Jupiter and Saturn and the 3:1 Kirkwood gap in the asteroid belt seen in figure 11. We conclude that the MMR plays an important role in creating structures in planetary systems.

Another prominent resonance of higher order than MMR is the secular resonance. In a system with three bodies it is possible that a precision motion of the perihelion occurs. If another body is added it can exceed such a motion. If these frequencies are integer ratios of each other, resonance phenomena occur.

A further resonance arising only for practically mass-less bodies is the Kozai resonance. This is applicable for comets and asteroids and will not be discussed further.

5.2 Instabilities in Trojan Twins Planets

In the special case of Trojan twin planets the process of system destabilization is triggered by close encounters of a Trojan body with the gas-giant. In a prior chapter the motions of the Trojan twin planets in the co-rotating frame have already been presented (figure 10). The lighter Trojan exceeds the bigger libration motion. Once the Trojan is getting closer to the gas-giant the eccentricity of the Trojan object is increased due to the gravitational interaction. This increase is consequently transferred to the second Trojan body and the process continues until a close encounter of the Trojan and the Jupiter occurs, finally ejecting the object from the system. The process is depicted in figure 12.

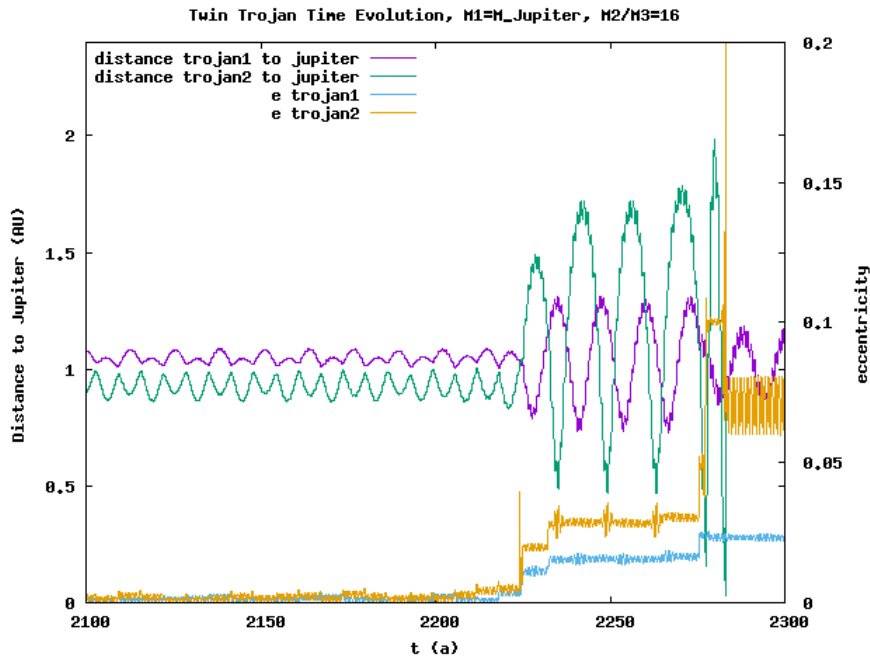


Figure 12: This figure portrays the time evolution of the distance of the two Trojan planets to the gas-giant (purple and turquoise) as well as the time evolution of the eccentricities of the Trojans (blue and yellow). After a simulation time of 2220 years the previously regular and periodic motion changes to a chaotic motion with the eccentricity of the objects increasing fast in discrete steps. The large relative motion of the planets leads to small distances towards the gas-giant until it exceeds a critical distance and the planet is ejected.

5.3 Stability Indicators

This section discusses two simple stability indicators and compares them concerning their accuracy of detecting stable and unstable configurations of the Trojan twin planets.

5.3.1 Maximal Relative Eccentricity

It is sometimes possible to find stability indicators which are exceptionally good for certain specific problems. For the Trojan twin planets such a stability estimator is the maximum relative eccentricity of the Trojans twins. When plotting the relative motion of the Trojans $\Delta\vec{r} = \vec{r}_1 - \vec{r}_2$ over a certain time interval for periodic motions a ringlike structure in the relative configuration space occurs. Since only cases with $i = 0^\circ$ are considered the configuration space can be reduced to 2 dimensions. The maximal relative eccentricity is defined via equation 25.

$$e_{max} = \frac{r_{max} - r_{min}}{r_{max} + r_{min}}, \quad (25)$$

where

$$r_{max} = \max(\{|\Delta r(\vec{t})|\}) \quad (26)$$

$$r_{min} = \min(\{|\Delta r(\vec{t})|\}) \quad (27)$$

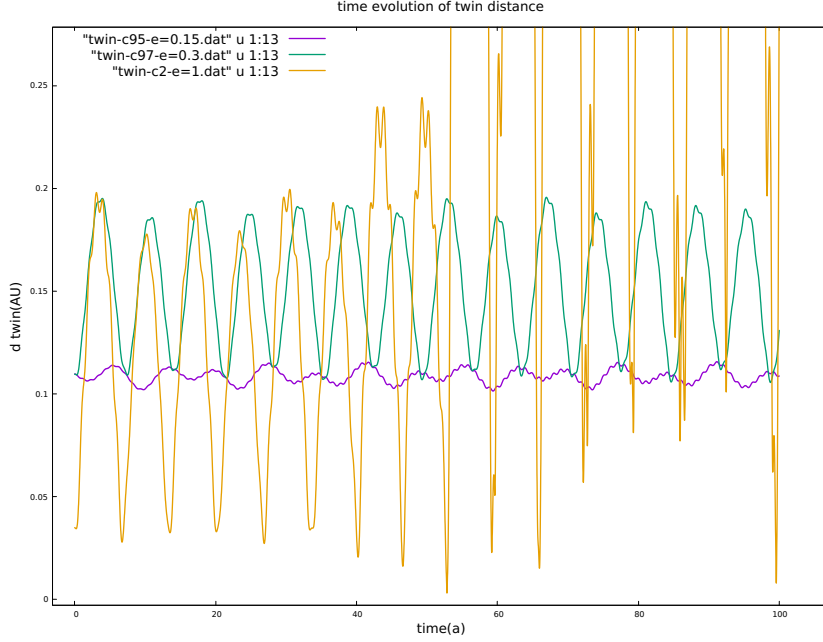


Figure 13: This figure shows the time evolution of the distances of the twin Trojans for different configurations. The purple line is for a system with Trojans of mass $M = 0.67M_{Earth}$ and an angular distance of $dm = 6.3^\circ$. This configuration leads to a low relative eccentricity of 0.15. The turquoise line represents a system with Trojans of mass $M = 1.1M_{Earth}$ and an angular distance of $dm = 6.3^\circ$. We observe an increase of the relative eccentricity to 0.3. Nevertheless, this system is still stable. The yellow line shows a system with Trojans of mass $M = 0.23M_{Earth}$ and an angular distance of $dm = 2.0^\circ$. We see that after approximately 50 years the system is becoming unstable and the relative eccentricity is converging towards unity ($e_{max} \rightarrow 1$).

Figure 13 shows different initial configurations of the twin Trojan planets and the corresponding time evolution of the distance between the objects. It is observed that for large eccentricities the relative motions are large and once a body escapes the stable region the eccentricity converges to 1.

5.3.2 Logarithmic Semi-Major Axis-Ratio $ln(a)$

A more general approach to indicate the stability of a celestial body in simulations is to introduce the $ln(a)$ -indicator. Contrary to the e_{max} -indicator it is not only applicable to the Trojan twin planets but can be generally used for finding changes in the semi-major axis of a body over a time period. In the definition of $ln(a)$ (equation 28) the logarithm the objects maximal over the minimal semi-major axis for the simulation time is formed. In this way changes in both directions increase the value. Since multiple Trojans are involved, the stability value assigned to the tested configuration is the maximum value of all Trojans in the system. The index i in equation 28 refers to the index of the Trojan.

$$ln(a) = max \left\{ ln \left(\frac{a_{max,i}}{a_{min,i}} \right) \right\} \quad (28)$$

where

$$a_{max,i} = max(\{a_i(t)\}) \quad (29)$$

$$a_{min,i} = min(\{a_i(t)\}) \quad (30)$$

5.3.3 Comparison of e_{max} and $ln(a)$

It is of uttermost importance that the results of different stability indicators are qualitatively the same. Of course the numbers assigned to the stability indicators will be different for distinct initial conditions of the system. Nevertheless, we demand that qualitatively the results are the same. This property can be tested at special points in the initial condition plot where the system suddenly jumps from stable to unstable behavior.

The comparison of the two stability indicators is shown in figure 14. A linear correlation seems to be present between e_{max} and $ln(a)$ at least for stable configurations. Interesting is that for e_{max} no values between ≈ 0.7 and 1.0 occur. Since a value of $e_{max} = 1.0$ corresponds to an unstable configuration, the limit of stability concerning e_{max} seems to be the value ≈ 0.7 . A question that occurs immediately is if this jumping behavior is observed for the $ln(a)$ stability indicator. We do not expect the saturation behavior for the $ln(a)$ -indicator, simply because the logarithmic definition of the $ln(a)$ -indicator can assume every positive value depending on the ejection orbit of the unstable Trojan. In the case of the $ln(a)$ -indicator we find a gap from values between ≈ 0.02 and ≈ 0.05 .

We conclude that for both indicators the sudden jump of the values can be observed and we have to investigate the reason for this behavior. The direct comparison of

the two stability indicators can be seen in figure 15. What we find is that at first glance the structures of the initial condition plot are the same. The blue region in the e_{max} -plot corresponds with the black region in the $ln(a)$ -plot. In the e_{max} -plot the yellow region represents unstable initial conditions. We observe that there is a sharp distinction between stable and unstable regions. This fact can already be observed in figure 14. For the $ln(a)$ -indicator we have two groups of values. The first group is formed by stable configurations and small values. All of these points are represented in the map with the color black. The second group consists of unstable configurations with rather high values of the stability indicator. We see that the visual representation of the $ln(a)$ -map is basically a dual state representation. In the stable region we are not able to identify finer substructures or patterns.

In the e_{max} -plot the stable region displays a variety of different values and we are able to observe substructures with darker colors. A valley of stability is formed in the center of the stable region where the smallest values of the relative eccentricity are assumed. This detail cannot be found in the $ln(a)$ -plot.

The conclusion is that it is of advantage to use the e_{max} stability indicator due to the higher resolution in the stable area. It is hence possible to identify substructures within this area which would not be observable directly by using the $ln(a)$ -indicator.

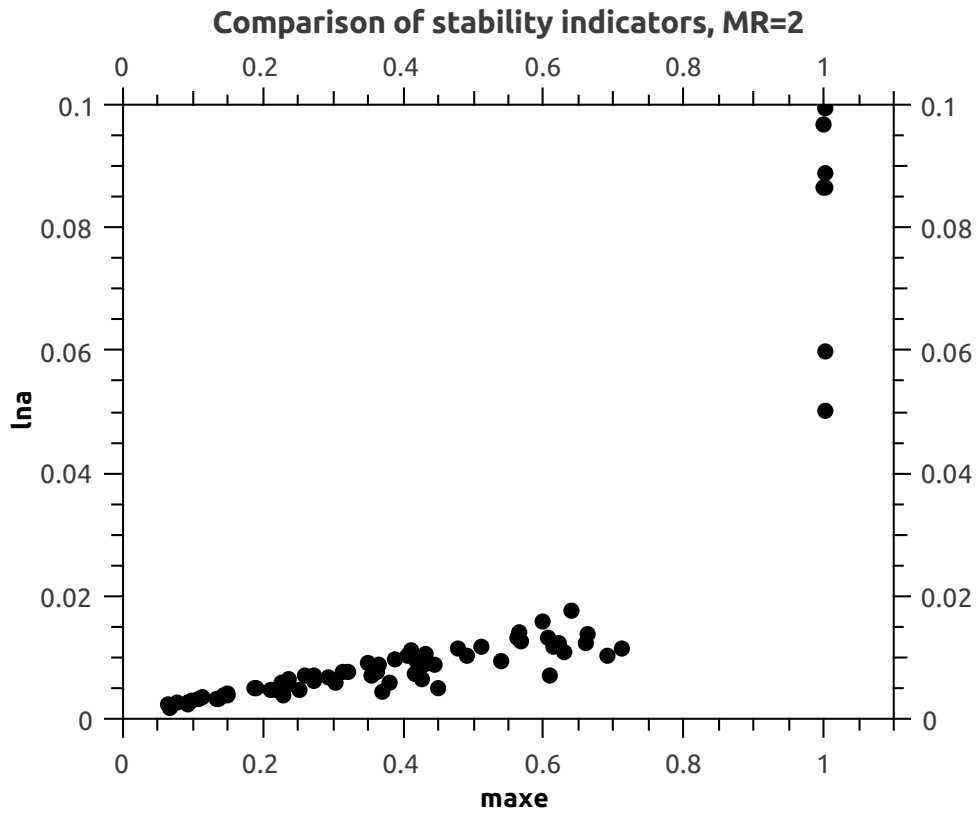
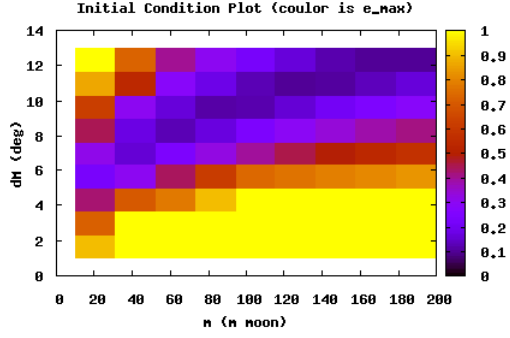
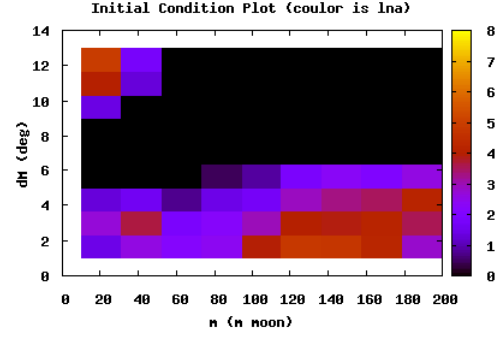


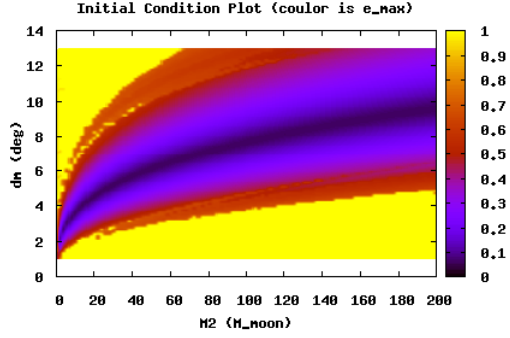
Figure 14: When comparing the two stability indicators we find that for small values there is a linear correlation between the two quantities. Furthermore we observe a gap in the values from ≈ 0.7 to 1 in e_{max} . A gap is found in the values of $\ln(a)$ from ≈ 0.02 to ≈ 0.05 . The data were generated from Trojan twin planets with a mass-ratio of $MR = 2$ and for different angular distances of the twins.



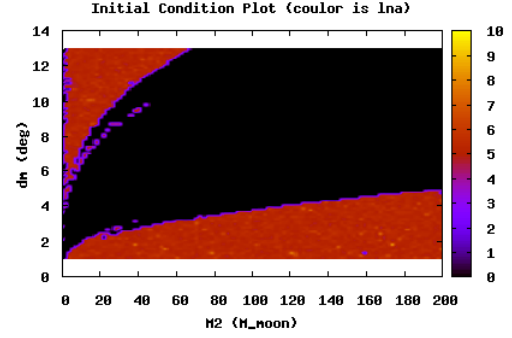
(a) Initial condition plot with e_{max} as stability indicator, mass-ratio $MR = 1.0$. The values of the stability indicator are given by the color code where blue corresponds to stable regions and yellow to unstable areas.



(b) Initial condition plot with $\ln(a)$ as stability indicator, mass-ratio $MR = 1.0$. The values of the stability indicator are given by the color code where black corresponds to stable regions and red to unstable regions.



(c) High resolution initial condition plot with e_{max} as stability indicator, mass-ratio $MR = 2.0$



(d) High resolution initial condition plot with $\ln(a)$ as stability indicator, mass-ratio $MR = 2.0$

Figure 15: Comparing the initial condition plots reveals that both the e_{max} -indicator (left) and the $\ln(a)$ -indicator (right) can distinguish stable from unstable configurations and that the results are consistent. The upper row depicts a low resolution example of an initial condition plot where many fine details cannot be perceived, whereas the high resolution figures already give a glimpse on the internal structures of the stable region. The biggest difference between the two indicators is that the $\ln(a)$ -indicator is not capable of resolving the detail in the stable area.

6 Lyapunov Indicator

A further goal of the master's thesis is developing a code capable of calculating the Lyapunov indicator for a n-body integrator. This quantity is used in order to quantify the speed of divergence or convergence of two infinitesimally close points in the phase space.

6.1 Introduction to LCE

A tool often used to characterize the chaoticity of dynamical systems is the so called Lyapunov exponent. An estimator for truncated integration time of the Lyapunov exponent (LCE) is called Lyapunov indicator (LCI). The first time the Lyapunov exponent was used to describe the exponential divergence of two nearby orbits was by Benettin et al. ([5]). The rate of divergence is expressed via equation 31. The next big step forward was the calculation of the Lyapunov indicators via solving the variational equations, instead of directly measuring the rate of divergence of two nearby orbits by Contopoulos et al. ([10]). The divergence is distinct for each dimension of the phase space of the dynamical system and hence the same number of Lyapunov exponents exist. Mostly, only the largest Lyapunov indicator is of interest but for the sake of completeness Benettin et al. ([4]) provides methods for the calculation of the whole spectrum. In this work only the largest Lyapunov indicator is calculated. The formal definition of the one dimensional LCE is given by equation 32. Figure 16 shows the time evolution of a trajectory and nearby trajectories in the phase space.

$$|x_t| = |x_0|e^{\lambda t} \quad (31)$$

$$\lambda = \lim_{t \rightarrow \infty} \frac{1}{t} \ln \frac{|x_t|}{|x_0|} \quad (32)$$

From equation 31 it is concluded that non-chaotic behavior is given for $\lambda \leq 0$. This condition has to be fulfilled by all λ_i .

$$(33)$$

Definition 1 *If $\forall \lambda_i$ with $i \in (1, D)$, where D is the dimension of the phase space: $\lambda_i \leq 0$, then the system is non-chaotic.*

To characterize the stability it is sufficient to only consider the maximum LCE (mLCE) denoted with λ_{max} .

Lemma 1 *If $\lim_{t \rightarrow \infty} \lambda_{max} = 0$, then the system is non-chaotic.*

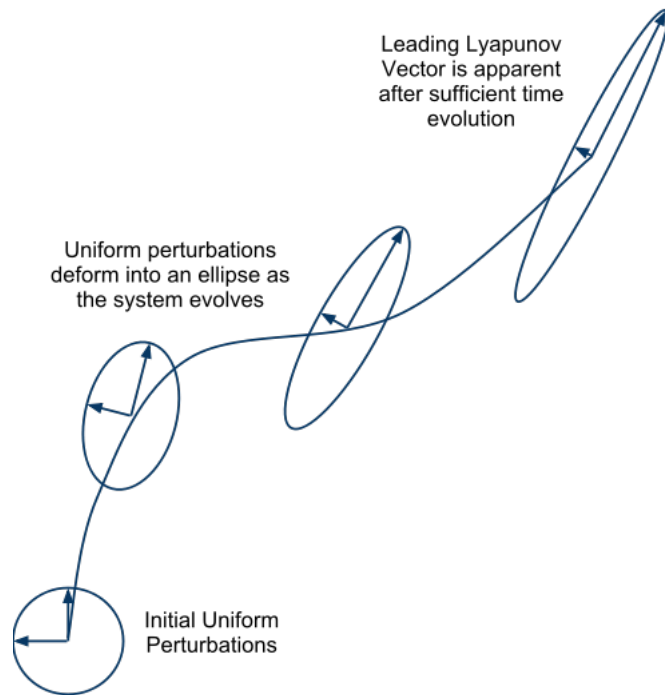


Figure 16: This figure shows the evolution of an initially uniform sphere around a point in the phase space with an infinitesimal small radius and its deformation over the time. Note that the total area of the ellipse is constant due to phase space conservation².

Let us furthermore introduce the Lyapunov exponent via the tangent space - a more formal way. Let $\Phi(\mathbf{x})^t$ be the state of the system at time t , then the state of the system at time $t + s$ can be written via equation 34.

$$\Phi(\mathbf{x})^{t+s} = \Phi^t \circ \Phi^s \quad (34)$$

The differential $d_{\mathbf{x}}\Phi^t$ is the tangent space of $\Phi^t(\mathbf{x})$. The application of $d_{\mathbf{x}}\Phi^t$ on a deviation vector \mathbf{w} in the tangent space gives the evolution of the deviation vector itself. The rule of consequential application of the tangent space is provided via equation 35.

$$d_{\mathbf{x}}\Phi^{t+s} = d_{\Phi^s(\mathbf{x})}\Phi^t \circ d_{\mathbf{x}}\Phi^s \quad (35)$$

We introduce $\lambda_t(\mathbf{x})$

$$\lambda_t(\mathbf{x}) = \frac{\|d_{\mathbf{x}}\Phi^t \mathbf{w}\|}{\|\mathbf{w}\|} \quad (36)$$

The expansion of the tangent space in direction of \mathbf{w} is described via λ_t . To get the order of exponential expansion the logarithm of the quantity is computed as seen in equation 37. We call this number the Lyapunov characteristic exponent (LCE).

$$LCE = \lim_{t \rightarrow \infty} \frac{1}{t} \ln \lambda_t(\mathbf{x}) \quad (37)$$

Nevertheless, for the computation this equation cannot be applied. The reason lies in the fast growth of the length of the deviation vector \mathbf{w} , which in short time reaches the overflow limit of computers. So other methods have to be used in order to calculate the LCE of a dynamical system. We will discuss them in later sections.

6.2 N-Body Integration with Lie-Series

Lie-series are a powerful tool to solve differential equations. The information for this chapter is from [17] on pages 449-453. The time evolution has the operator form as seen in equations 38 and 39.

$$\mathbf{r}_\nu(t + \Delta t) = e^{\Delta t D} \mathbf{r}_\nu(t) \quad (38)$$

$$\mathbf{v}_\nu(t + \Delta t) = e^{\Delta t D} \mathbf{v}_\nu(t) \quad (39)$$

This expression can be written as infinite series:

$$\mathbf{r}_\nu(t + \Delta t) = e^{\Delta t D} \mathbf{r}_\nu(t) = \sum_{n=0}^{\infty} \frac{(\Delta t D)^n}{n!} \mathbf{r}_\nu(0) \quad (40)$$

Each problem has its own Lie operator. For the gravitational n-body problem it has the form seen in equation 41.

²Figure credit: <https://upload.wikimedia.org/wikipedia/commons/0/04/LyapunovDiagram.svg>

$$D = \sum_{i=1}^3 \sum_{\nu=1}^N \left(v_{\nu}^i \frac{\partial}{\partial r_{\nu}^i} + \sum_{\mu=1, \nu \neq \mu}^N m_{\mu} r_{\mu\nu}^i \rho_{\nu\mu}^{-3} \frac{\partial}{\partial v_{\nu}^i} \right) \quad (41)$$

We use the following abbreviations:

$$\mathbf{r}_{\nu\mu} = \mathbf{r}_{\mu} - \mathbf{r}_{\nu} = -\mathbf{r}_{\mu\nu} \quad (42)$$

$$\rho_{\nu\mu} = |\mathbf{r}_{\mu} - \mathbf{r}_{\nu}| = |\mathbf{r}_{\nu\mu}| \quad (43)$$

$$\mathbf{v}_{\nu\mu} = \mathbf{v}_{\mu} - \mathbf{v}_{\nu} = -\mathbf{v}_{\mu\nu} \quad (44)$$

Fortunately there are recursion relations for the calculation of the terms of the Lie-series.

$$D^n \mathbf{r} = \sum_{k=1, l \neq k}^N m_{\mu} \sum_{l=0}^{n-2} \binom{n-2}{l} D^l \phi_{\nu\mu} D^{n-2-l} \mathbf{r}_{\mu\nu} \quad (45)$$

$$D^n \phi_{\nu\mu} = \rho_{\nu\mu}^{-2} \sum_{l=0}^{n-1} a_{n,l+1} D^{n-1-l} \phi_{\nu\mu} D^l \Lambda_{\mu\nu} \quad (46)$$

where the coefficients a are:

$$a_{n,n} = -3 \quad n \geq 0$$

$$a_{n,1} = a_{n-1,1} - 2 \quad n \geq 1$$

$$a_{n,l} = a_{n-1,l-1} + a_{n-1,l} \quad 1 \leq l < n$$

$$D^n \Lambda_{\mu\nu} = \sum_{i=1}^3 \sum_{l=0}^{nint(\frac{n}{2})} b_{n,l} D^l \mathbf{r}_{\mu\nu} D^{n+1-l} \mathbf{r}_{\mu\nu} \quad (47)$$

where the coefficients b are:

$$b_{n,0} = 1 \quad n \geq 0$$

$$b_{n,l} = b_{n-l,l-1} + b_{n-1,l} \quad 1 < l < nint \frac{n}{2}$$

$$b_{n,nint(\frac{n}{2})} = b_{n-1,nint(\frac{n}{2})} - 1 \quad n \text{ odd}$$

$$b_{n,nint(\frac{n}{2})} = 2b_{n-1,nint(\frac{n}{2})} + b_{n-1,nint(\frac{n}{2})-1} \quad n \text{ even}$$

Please keep in mind that these recursion equations only apply for order $n \geq 2$.

6.3 MLCE via Mapping

A scheme for the calculation of the mLCE is presented. Most of the equations can be found in [41] on pages 63-95. Consider an integration scheme of the form seen in equation 48.

$$\mathbf{x}(t + \Delta t) = \mathbf{f}(\mathbf{x}(t)) \quad (48)$$

Also consider a deviation vector \mathbf{w} and the Jacobian Matrix \mathbf{M} of the integration scheme as seen in equation 49. Here \mathbf{p} is the phase space vector with dimension $D = 6N$, $\mathbf{p} = (x_1, x_2, \dots, x_{3N}, p_1, p_2, \dots, p_{3N})$. The time derivatives of the deviation vector can be expressed as seen in equation 50.

$$\mathbf{M} = \frac{\partial f_i}{\partial p_j} \quad (49)$$

$$\dot{\mathbf{w}}(t) = \mathbf{M}\mathbf{w}(t) \quad (50)$$

If the map is symplectic equation 51 holds.

$$\mathbf{w}(t + \Delta t) = \mathbf{M}\mathbf{w}(t) \quad (51)$$

A symplectic map fulfills following relation:

$$\mathbf{M}^T \mathbf{J}_{2D} \mathbf{M} = \mathbf{J}_{2D} \quad (52)$$

where

$$\mathbf{J}_{2D} = \begin{bmatrix} \mathbf{0}_D & \mathbf{I}_D \\ -\mathbf{I}_D & \mathbf{0}_D \end{bmatrix} \quad (53)$$

After every time step the deviation vector is normalized: $\mathbf{w} = \frac{\hat{\mathbf{w}}}{\alpha}$, where $\alpha = |\hat{\mathbf{w}}|$. In order to calculate λ_{max} , equation 54 is utilized. Here N denotes the number of time steps, $\tau = N \cdot \Delta t$ is the total integration time and α_i is the absolute value of the deviation vector for the i -th timestep. The renormalization of the deviation vector is depicted in figure 17.

$$\lambda_{max} = \frac{1}{\tau} \sum_{i=0}^N \ln \alpha_i \quad (54)$$

Furthermore the Lyapunov-time can be introduced. It is the time that a nearby orbit needs to converge by e or in other words the time that the dynamical system needs to become chaotic (equation 55).

$$\tau_L = \frac{1}{\lambda_{max}} \quad (55)$$

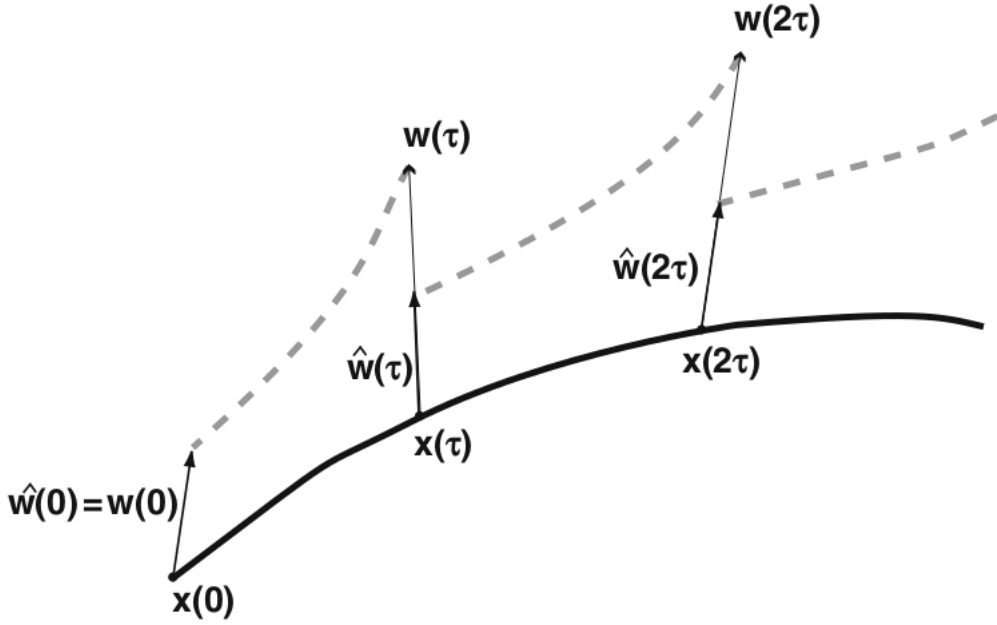


Figure 17: This figure shows the evolution of the deviation vector denoted by \mathbf{w} . After one timestep the initial deviation vector \mathbf{w} evolves to $\hat{\mathbf{w}}$. Then the deviation vector is renormalized and again evolved in time. Figure credit: [41] page 95.

6.4 MLCE via Hamiltonian

It is possible to calculate the mLCE from the Hamiltonian of the dynamical system with equation 56 for the time derivative of the deviation vector:

$$\dot{\mathbf{w}} = \mathbf{J}_{2D} \hat{\mathbf{H}}(H(\vec{x}(t))) \mathbf{w} \quad (56)$$

$$\hat{\mathbf{H}}(H) = \frac{\partial^2 H}{\partial x_i \partial x_j} \quad (57)$$

Here $\hat{\mathbf{H}}(H)$ is the Hessian of the Hamiltonian (equation 57) and \mathbf{J}_{2N} can be found in equation 53. In order to calculate the maximum Lyapunov indicator (equation 54) we have to use an integration scheme to obtain the next time step of the deviation vector \mathbf{w} .

6.5 Application of MLCE-Algorithm on Standard Map: Mapping-Approach

In this section the mapping-approach is tested on the standard map. The standard map is a two dimensional mapping defined via equation 58. Figure 18 shows the time evolution of the current mLCE in the case of resonant initial conditions. What

we see is that even after 10^7 iterations the LCE is still decreasing. This is typical for non-chaotic behavior.

$$p_{n+1} = p_n + k \cdot \sin(\theta_n) \quad (58)$$

$$\theta_{n+1} = (\theta_n + p_{n+1}) \bmod(2\pi) \quad (59)$$

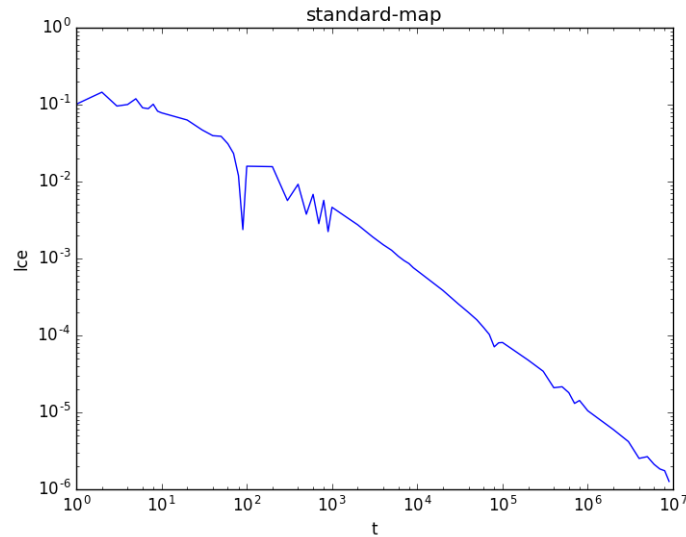


Figure 18: This plot shows the time evolution of the mLCE for resonant initial conditions of the standard map: $p=2.15$, $\theta = 0$.

By changing the initial conditions to $p = 3.1024048$, $\theta = 0$, we obtain the time evolution of the mLCE, as seen in figure 19. We observe that after approximately 10^6 iterations the values for the current Lyapunov indicators are staying almost constant. This means that two close points in the phase space diverge exponentially. We call this weakly chaotic, due to the small fixed value of the mLCE. For the initial conditions $p = 3.1024048$, $\theta = 0$ the system behaves strongly chaotic, which is seen in figure 20.

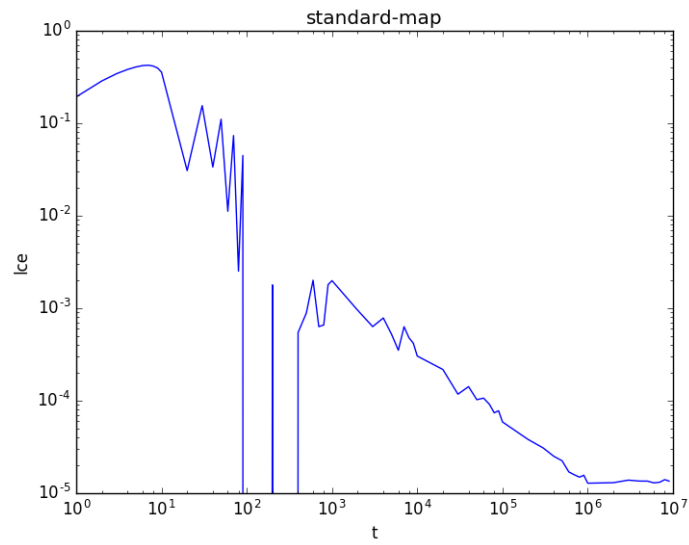


Figure 19: This plot shows the time evolution of the mLCE for weakly chaotic initial conditions of the standard map: $p=3.1024048$, $\theta = 0$.

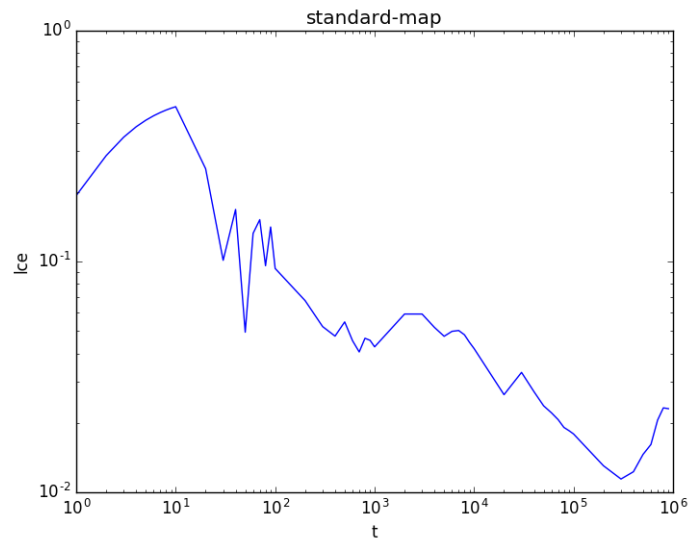


Figure 20: This plot shows the time evolution of the mLCE for strongly chaotic initial conditions of the standard map: $p=3.14$, $\theta = 0$.

6.6 Application of MLCE-Algorithm on Lie-Series N-Body Integrator: Mapping-Approach

When trying to calculate the mLCE, we need to know equation 48 explicitly in order to calculate the Jacobian. Due to the special form of equation 48 in the case of the Lie-series n-body integration it is numerically costly to calculate the Jacobian directly. The trick in the calculation of the integration is that a recursive relation of the Lie-terms can be found and hence the numerical values of the prior order are reused for the calculation of a higher order. This makes the else cpu-time intensive direct calculation of each lie-term efficient and comparable in speed to other integration schemes.

6.6.1 Derivatives of Lie-Series-Recursions

The goal is to explicitly express the Jacobian of relation 48 for the Lie-series integrator. The recursion of the time step is given by equations 45, 46 and 47. Now the partial derivatives of position and velocity of the recursion for one time step are formed.

6.6.2 Derivatives of Spatial Components

At first, the spatial derivatives of the Lie-terms are formed. The derivatives with respect to the spatial coordinates are needed of the body for which the Lyapunov indicator is to be calculated. $x_i \in (x_1, x_2, x_3, v_1, v_2, v_3)$ represents the phase space coordinates of the body of interest, where the first three entries are the spatial component. Equations 60, 61 and 62 are the recursion relations for the spatial derivatives.

$$\frac{\partial D^n \mathbf{r}_\nu}{\partial x_i} = \sum_{k=1, l \neq k}^N m_\mu \sum_{l=0}^{n-2} \binom{n-2}{l} \left(\frac{\partial D^l \phi_{\nu\mu}}{\partial x_i} D^{n-2-l} \mathbf{r}_{\mu\nu} + D^l \phi_{\nu\mu} \frac{\partial D^{n-2-l} \mathbf{r}_{\mu\nu}}{\partial x_i} \right) \quad (60)$$

$$\begin{aligned} \frac{\partial D^n \phi_{\nu\mu}}{\partial x_i} = & \sum_{l=0}^{n-1} a_{n,l+1} \left(\frac{\partial \rho_{\nu\mu}^{-2}}{\partial x_i} D^{n-1-l} \phi_{\nu\mu} D^l \Lambda_{\mu\nu} + \right. \\ & \left. \rho_{\nu\mu}^{-2} \frac{\partial D^{n-1-l} \phi_{\nu\mu}}{\partial x_i} D^l \Lambda_{\mu\nu} + \rho_{\nu\mu}^{-2} D^{n-1-l} \phi_{\nu\mu} \frac{\partial D^l \Lambda_{\mu\nu}}{\partial x_i} \right) \end{aligned} \quad (61)$$

$$\frac{\partial D^n \Lambda_{\mu\nu}}{\partial x_i} = \sum_{i=1}^3 \sum_{l=0}^{n \text{int}(\frac{n}{2})} b_{n,l} \left(\frac{\partial D^l \mathbf{r}_{\mu\nu}}{\partial x_i} D^{n+1-l} \mathbf{r}_{\mu\nu} + D^l \mathbf{r}_{\mu\nu} \frac{\partial D^{n+1-l} \mathbf{r}_{\mu\nu}}{\partial x_i} \right) \quad (62)$$

6.6.3 Derivatives of Velocity Components

By making one important observation it is possible to simplify the handling of the velocities with the Lie-series n-body integrator.

$$D^0 \mathbf{r}_\nu = \mathbf{r}_\nu \quad (63)$$

$$D^1 \mathbf{r}_\nu = \mathbf{v}_\nu = D^0 \mathbf{v}_\nu \quad (64)$$

Via equation 64 it is found that in order to calculate the velocities we simply need to shift the order of the Lie-terms. Hence the calculation of the velocities to the same order as the positions just requires an additional computation of a single further order:

$$\mathbf{v}_\nu(t + \Delta t) = \sum_{n=0}^{\infty} \frac{\Delta t^n D^{n+1}}{n!} \mathbf{r}_\nu(0) \quad (65)$$

This implies equation 66.

$$\frac{\partial D^n \mathbf{v}_\nu}{\partial x_i} = \frac{\partial D^{n+1} \mathbf{r}_\nu}{\partial x_i} \quad (66)$$

6.6.4 Derivatives of Order Zero and One

Above recursions are valid for $n \geq 2$. Therefore the expressions for the lower two orders have to be written down explicitly. However, this is not tedious. At first one has to make clear what the meanings of \mathbf{r}_ν and x_i are. Keep in mind that $\mathbf{r}_\nu = (x_1, x_2, x_3)$.

For $i \in (1, 2, 3)$, which are the derivatives in respect to the position, it holds that:

$$\begin{aligned} \frac{\partial D^0 \mathbf{r}_\nu}{\partial x_i} &= \delta_{\nu j i} && \text{since } D^0 \mathbf{r}_\nu = \mathbf{r}_\nu \\ \frac{\partial D^1 \mathbf{r}_\nu}{\partial x_i} &= 0 && \text{since } D^1 \mathbf{r}_\nu = \mathbf{v}_\nu \end{aligned}$$

For $i \in (4, 5, 6)$, which are the derivatives in respect to velocity, it holds that:

$$\begin{aligned} \frac{\partial D^0 \mathbf{r}_\nu}{\partial x_i} &= 0 && \text{since } D^0 \mathbf{r}_\nu = \mathbf{r}_\nu \\ \frac{\partial D^1 \mathbf{r}_\nu}{\partial x_i} &= \delta_{\nu j i} && \text{since } D^1 \mathbf{r}_\nu = \mathbf{v}_\nu \end{aligned}$$

By using equation 66 we get following relations for $i \in (1, 2, 3)$:

$$\begin{aligned} \frac{\partial D^0 \mathbf{v}_\nu}{\partial x_i} &= \frac{\partial D^1 \mathbf{r}_\nu}{\partial x_i} = 0 \\ \frac{\partial D^1 \mathbf{v}_\nu}{\partial x_i} &= \frac{\partial D^2 \mathbf{r}_\nu}{\partial x_i} \end{aligned}$$

For $i \in (4, 5, 6)$, which are the derivatives in respect to velocity, it holds that:

$$\begin{aligned}\frac{\partial D^0 \mathbf{v}_\nu}{\partial x_i} &= \frac{\partial D^1 \mathbf{r}_\nu}{\partial x_i} = \delta_{\nu_j i} \\ \frac{\partial D^1 \mathbf{v}_\nu}{\partial x_i} &= \frac{\partial D^2 \mathbf{r}_\nu}{\partial x_i}\end{aligned}$$

6.6.5 Derivative of Lie-Series

We now have the tools to calculate the partial derivatives of the Lie-series 40.

$$\frac{\partial \mathbf{r}_\nu(t + \Delta t)}{\partial x_i} = \sum_{n=0}^{\infty} \frac{\Delta t^n}{n!} \frac{\partial D^n \mathbf{r}_\nu(0)}{\partial x_i} \quad (67)$$

$$\frac{\partial \mathbf{v}_\nu(t + \Delta t)}{\partial x_i} = \sum_{n=0}^{\infty} \frac{\Delta t^n}{n!} \frac{\partial D^{n+1} \mathbf{r}_\nu(0)}{\partial x_i} \quad (68)$$

6.7 Application of MLCE-Algorithm on Henon-Heiles System: Hamiltonian-Approach

The most complicated part of the direct implementation of the LCE is the calculation of the Jacobian. This can be seen by the complex structure of equation 60. An easier way is the application of the Hamiltonian-approach. To demonstrate the applicability of the method it is tested on a simpler Hamiltonian system: The Henon-Heiles system. The Henon-Heiles system is formulated with the Hamiltonian seen in equation 69.

$$H(q_1, q_2, p_1, p_2) = \frac{1}{2}(p_1^2 + p_2^2 + q_1^2 + q_2^2) + q_1^2 q_2 - \frac{1}{3} q_2^3 \quad (69)$$

The Hessian matrix takes the form seen in equation 70.

$$\hat{\mathbf{H}} = \begin{bmatrix} 1 + 2q_2 & 2q_1 & 0 & 0 \\ 2q_1 & 1 - 2q_2 & 0 & 0 \\ 0 & 0 & 1 & 0 \\ 0 & 0 & 0 & 1 \end{bmatrix} \quad (70)$$

The time evolution of the system is given by the Hamilton equations 71.

$$\begin{aligned}\dot{q}_1 &= \frac{\partial H}{\partial p_1} = p_1 \\ \dot{q}_2 &= \frac{\partial H}{\partial p_2} = p_2 \\ \dot{p}_1 &= \frac{\partial H}{\partial q_1} = -q_1 - 2q_1 q_2 \\ \dot{p}_2 &= \frac{\partial H}{\partial q_2} = -q_2 - q_1^2 + q_2^2\end{aligned} \quad (71)$$

With help of equation 56 the variational equations describing the time evolution of the deviation vector are formed in equation 72.

$$\begin{aligned}
 \dot{w}_1 &= w_3 \\
 \dot{w}_2 &= w_4 \\
 \dot{w}_3 &= (-1 - 2q_2)w_1 - 2q_1w_2 \\
 \dot{w}_4 &= (-2q_1)w_1 + (-1 + 2q_2)w_2
 \end{aligned} \tag{72}$$

The integration of the system and the variational equations is conducted via a Runge-Kutte-4 integrator. In order to visualize the values of the phase space we have to apply the so called surface of section. The Henon-Heiles system is a 4-dimensional system. One parameter is eliminated by setting a fixed energy value. Then, for every time a third parameter obtains the value zero (e.g. $p_1 = 0$) a coordinate point of the remaining 2 parameters of the phase space is plotted. This method is called the surface of section. Additionally, the histograms of the local Lyapunov indicator are plotted in order to identify possible differences between regular and chaotic orbits. The local Lyapunov indicator is nothing else than the norm of the deviation vector at time t , $\alpha(t)$. The results for the Henon-Heiles system for different initial conditions are shown in figures 21, 22 and 23.

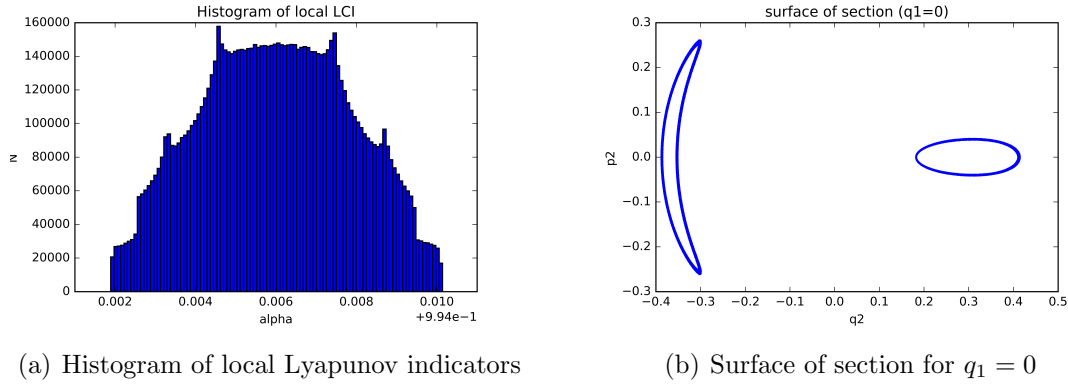
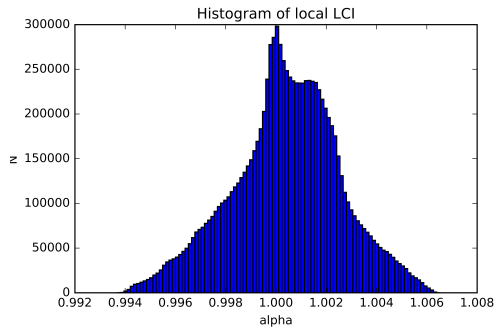
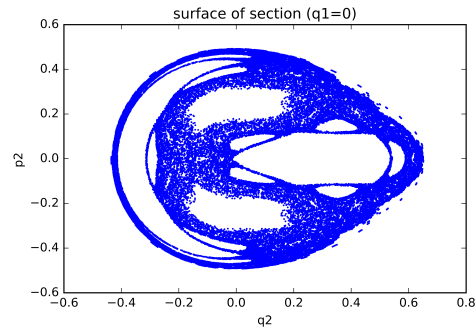


Figure 21: The initial conditions for these plots are $E = 0.125$, $q_2 = 0.2$, $p_2 = 0.02$.

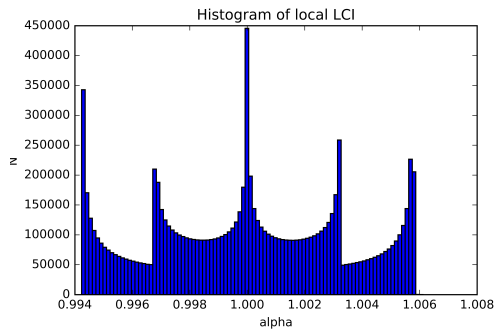


(a) Histogram of local Lyapunov indicators

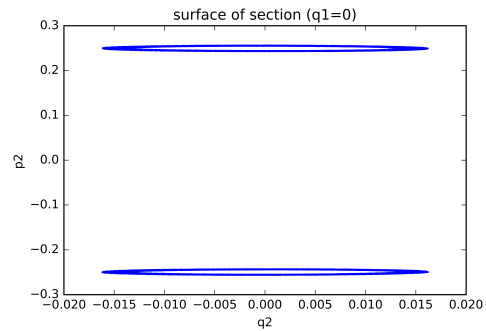


(b) Surface of section for $q_1 = 0$

Figure 22: The initial conditions for these plots are $E = 0.125$, $q_2 = 0.2$, $p_2 = 0.14$.



(a) [Histogram of local Lyapunov indicators



(b) Surface of section for $q_1 = 0$

Figure 23: The initial conditions for these plots are $E = 0.125$, $q_2 = 0.015$, $p_2 = 0.25$.

Figures 21 and 23 are results for periodic orbits. This is visible in the surface of section where only a restricted area in the phase space is attained. On the other hand, figure 22 shows a chaotic orbit of the Henon-Heiles system with a heavily scattered surface of section. When having a look on the corresponding local Lyapunov indicator histograms, one observes a striking difference depending on the orbits chaoticity. Chaotic orbits consistently show only one peak whereas stable orbits have multiple peaks. Furthermore the histograms are symmetric for stable orbits. When having a look at the time evolution of the Lyapunov indicator we find the expected behavior of convergence of the value toward zero for stable orbits and nonzero values in the case of chaotic orbits. Figure 24 shows the Lyapunov indicator and the surface of section of a regular orbit, figure 25 the Lyapunov indicator and the surface of section of a chaotic orbit. After a time of $T = 10^5$ the Lyapunov indicator assumes values of $\approx 10^{-4}$. The values can be compared with results from [6] whose results can be seen in figure 26. The calculated values from this work do correspond well with the values from [6]. Results for six different initial conditions

are found in table 1. The table includes the Lyapunov time, which is the inverse of the Lyapunov indicator, an estimate for the time the system stays stable.

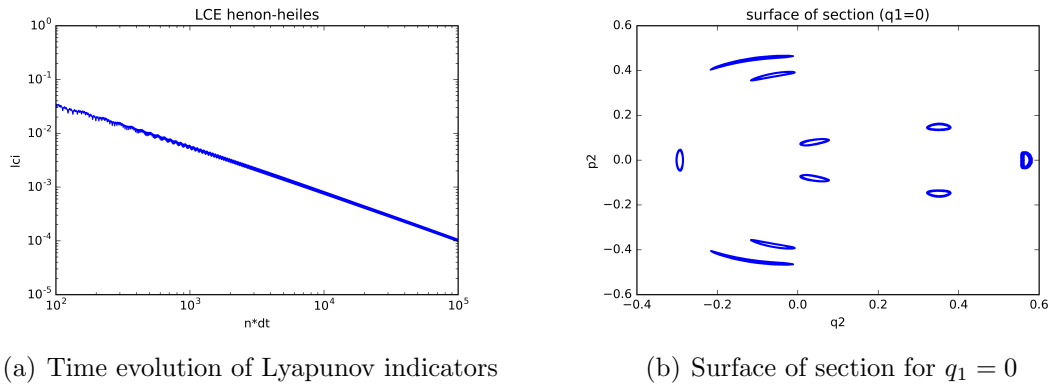


Figure 24: The initial conditions for these plots are $E = 0.125$, $q_2 = 0.33$, $p_2 = 0.14$.

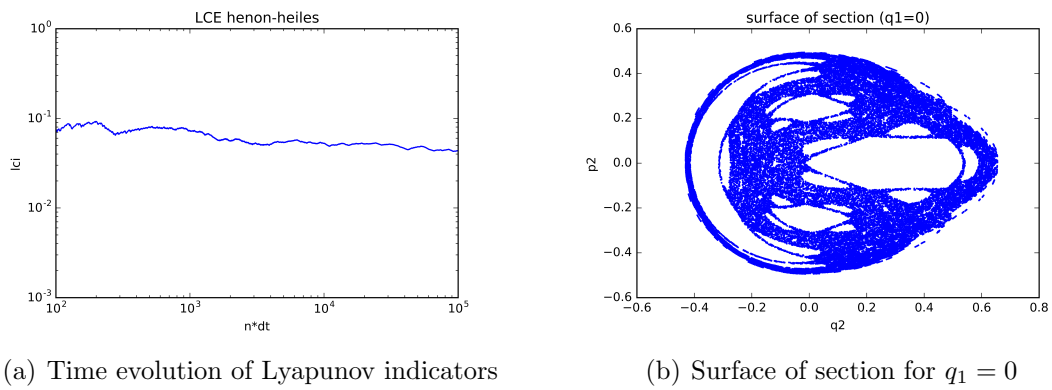


Figure 25: The initial conditions for these plots are $E = 0.125$, $q_2 = -0.15$, $p_2 = 0.02$.

Table 1: This table contains the results for the calculations of the Lyapunov indicator and Lyapunov time of the Henon-Heiles system for different initial conditions. The integration time for all values is $T = 10^5$.

E	q1	q2	p1	p2	LCI	Lyapunov-time
0.125	0.0	0.2	4.64E-01	0.02	8.870E-05	1.127E+04
0.125	0.0	0.33	3.81E-01	0.14	1.049E-04	9.529E+03
0.125	0.0	0.015	4.33E-01	0.25	1.088E-04	9.188E+03
0.125	0.0	0.2	4.42E-01	0.14	4.001E-02	2.499E+01
0.125	0.0	-0.15	4.74E-01	0.02	4.361E-02	2.293E+01
0.125	0.0	0.25	3.29E-01	0.3	3.626E-02	2.758E+01

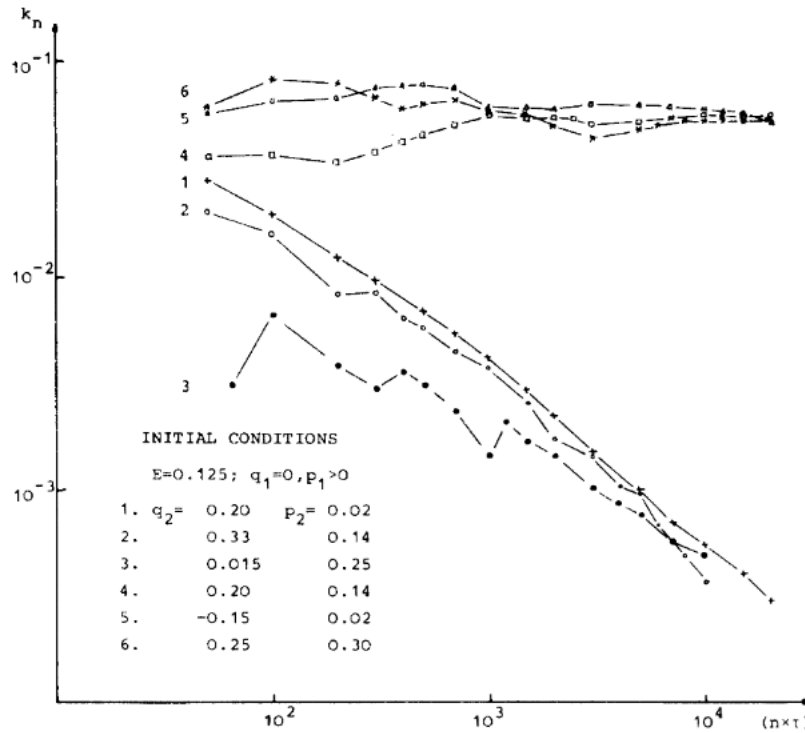


Figure 26: Results from [6] show that the values for the Lyapunov indicators are qualitatively and quantitatively extremely close to the calculations from this work. Figure source: [6].

6.8 Hamiltonian of N-Body System

The Hamiltonian of a general n-body system with only gravitational interaction can be expressed through equation 73.

$$H = T + U = \sum_{i=1}^N \frac{1}{2} p_i^2 m_i + \sum_{i < j} -G \frac{m_i m_j}{|r_i - r_j|} \quad (73)$$

We are now able to form the time derivative of the deviation vector \mathbf{w} with equation 74.

$$\dot{\mathbf{w}} = \mathbf{J}_{2D} \hat{\mathbf{H}}(H(\vec{x}(t))) \mathbf{w} \quad (74)$$

We denote the phase space variables as follows:

$\vec{x}_i = (\vec{r}_i, \vec{v}_i) = (x_{i,1}, x_{i,2}, x_{i,3}, v_{i,1}, v_{i,2}, v_{i,3})$. Hence the Hamiltonian from equation 73 is expressed in terms of components with equation 75.

$$H = \sum_{i=1}^N \sum_{j=1}^3 v_{i,j}^2 \frac{m_i}{2} + \sum_{i < j} -G \frac{m_i m_j}{\sqrt{(x_{i,1} - x_{j,1})^2 + (x_{i,2} - x_{j,2})^2 + (x_{i,3} - x_{j,3})^2}} \quad (75)$$

The Hessian simplifies due to the lack of mixed expressions of positions and velocities:

$$\forall i, k : \frac{\partial^2 H}{\partial x_{j,i} \partial v_{j,k}} = 0, \quad i, k = 1, 2, 3 \quad (76)$$

This leads to a block form of the Hessian matrix in equation 77.

$$\hat{\mathbf{H}} = \begin{bmatrix} \mathbf{H}_x & \mathbf{0}_3 \\ \mathbf{0}_3 & \mathbf{H}_v \end{bmatrix} \quad (77)$$

The spatial diagonal component of the Hessian can be written as seen in equation 78.

$$\mathbf{H}_{x,k,k} = \sum_{j=1, j \neq p}^N GM_p M_j \left(\frac{-3(x_{j,k} - x_{p,k})^2}{((x_{j,1} - x_{p,1})^2 + (x_{j,2} - x_{p,2})^2 + (x_{j,3} - x_{p,3})^2)^{5/2}} + \frac{1}{((x_{j,1} - x_{p,1})^2 + (x_{j,2} - x_{p,2})^2 + (x_{j,3} - x_{p,3})^2)^{3/2}} \right) \quad (78)$$

The non-diagonal spatial components of the Hessian are given by equation 79

$$\mathbf{H}_{x,m,n} = \sum_{j=1, j \neq p}^N GM_p M_j \left(\frac{-3(x_{j,m} - x_{p,m})(x_{j,n} - x_{p,n})}{((x_{j,1} - x_{p,1})^2 + (x_{j,2} - x_{p,2})^2 + (x_{j,3} - x_{p,3})^2)^{5/2}} \right) \quad (79)$$

Since the order of the partial derivatives can be interchanged the non-diagonal elements are symmetric and it holds that $\mathbf{H}_{x,i,j} = \mathbf{H}_{x,j,i}$.

The velocity sub-matrix is expressed by equation 80.

$$\mathbf{H}_{v,i} = \mathbf{1}/M_i \quad (80)$$

6.9 Application of MLCE-Algorithm on N-Body System: Hamiltonian-Approach

After successfully applying the Hamiltonian-approach on a simple dynamical problem - the Henon-Heiles system - the next step is to apply the method to the general n-body Hamiltonian. The integrator used in this work is a Lie-series integrator. However, this method is independent of the integration scheme and is applicable after the actual integration itself. The only information needed are the output file with the coordinates of the bodies as well as the masses of the bodies.

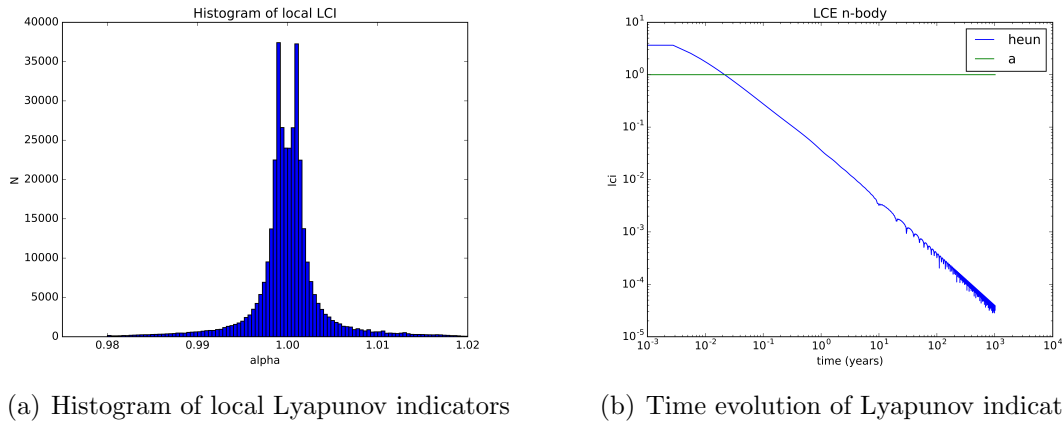


Figure 27: Stable body: The left chart shows the distribution of the local Lyapunov indicators and on the right hand side the time evolution of the Lyapunov indicator is portrayed as well as the time evolution of the bodie's semi-major axis.

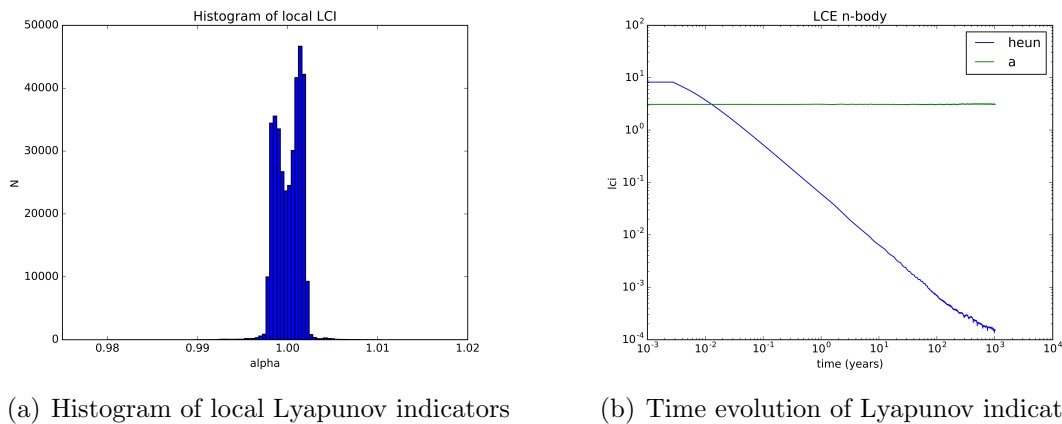


Figure 28: Chaotic body: The left chart shows the distribution of the local Lyapunov indicators and on the right hand side the time evolution of the Lyapunov indicator is portrayed as well as the time evolution of the bodie's semi-major axis.

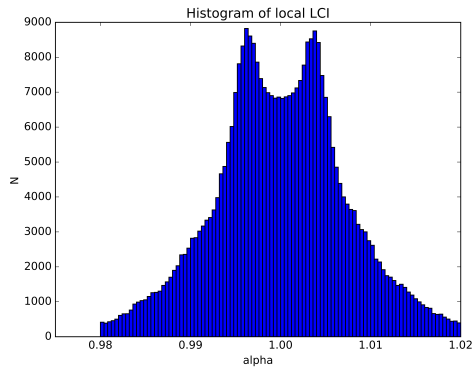
Table 2: This table contains the orbital elements of a system used to test the Hamiltonian-approach for calculations of Lyapunov indicators. The central body has a mass of $1M_{Sun}$.

a	e	i	Ω	ω	M	mass (M_{Sun})
1	0.0	0.0	0.0	0.0	0.0	0.000955
1.1	0.5	10	20	350	258	1E-7

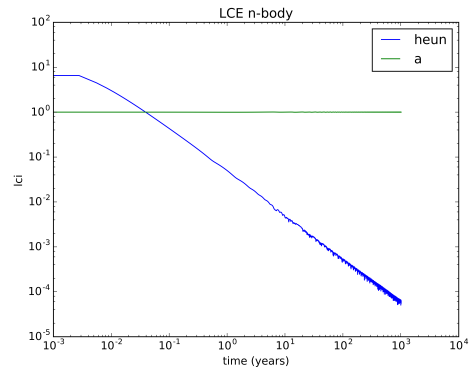
Figures 27 and 28 show the application of the Hamiltonian-approach on a simple system with 3 bodies. The system's orbital elements are given in table 2, with a central body of one solar mass. Figure 27 shows the results for a stable body. The left chart is a local Lyapunov indicator histogram that is clearly symmetrical in shape, which already indicates that the body is stable. The right chart shows the time evolution of the Lyapunov indicator, converging towards zero. The green line is the time evolution of the bodie's semi-major axis which is constant over the whole integration time. On the other hand, the second body is clearly chaotic. The histogram (figure 28) is asymmetric and the Lyapunov indicator converges toward a non-zero value. This corresponds well to the changes we observe in the bodies semi-major axis.

6.10 Application of Hamiltonian-Approach on Trojan Twin Planets

This section tests the applicability of the Lyapunov indicator as stability indicator for the Trojan twin planets. A stable configuration with $M_{tot} = 2M_{Earth}$ and an initial angular separation of $dm = 9^\circ$ gives results, as seen in figures 29 and 30. The local Lyapunov indicator histograms are both symmetrical and the Lyapunov indicator decreases over time. For an unstable configuration with $M_{tot} = 2M_{Earth}$ and $dm = 3^\circ$ the results are shown in figures 31 and 32. Both histograms are asymmetric which already indicates an unstable configuration. After a simulation time of $T = 300$ years the Lyapunov indicator stops decreasing and reaches a plateau. The conclusion is that it is possible to detect stable and unstable configurations of Trojan twin planets by using the Lyapunov indicator.

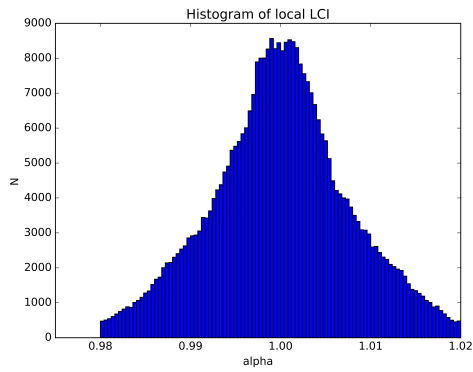


(a) Histogram of local Lyapunov indicators for Trojan 1

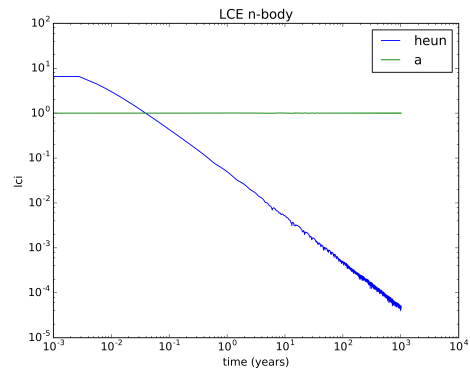


(b) Time evolution of Lyapunov indicator for Trojan 1

Figure 29: Stable configuration: This figures show the histogram of the local Lyapunov indicators as well as the time evolution of the Lyapunov indicator of the first Trojan planet for a stable configuration.

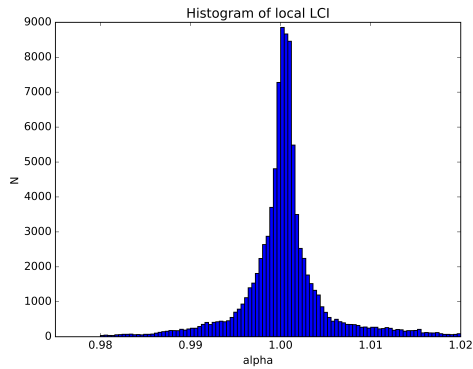


(a) Histogram of local Lyapunov indicators for Trojan 2

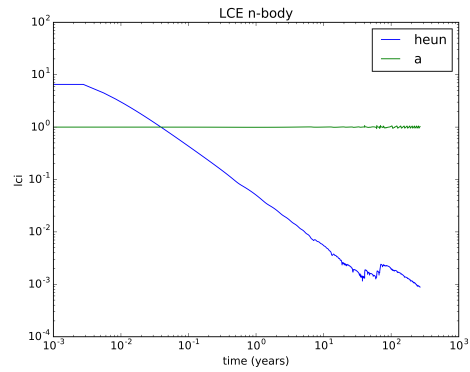


(b) Time evolution of Lyapunov indicator for Trojan 2

Figure 30: Stable configuration: This figures show the histogram of the local Lyapunov indicators as well as the time evolution of the Lyapunov indicator of the second Trojan planet for a stable configuration.

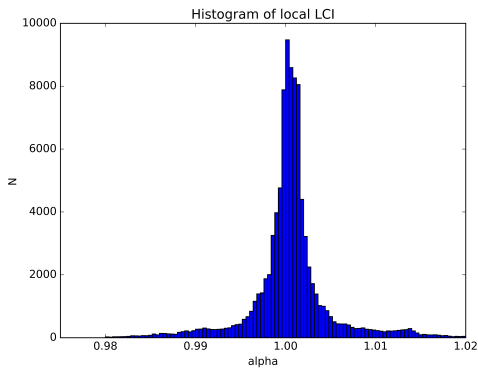


(a) [Histogram of local Lyapunov indicators for Trojan 1

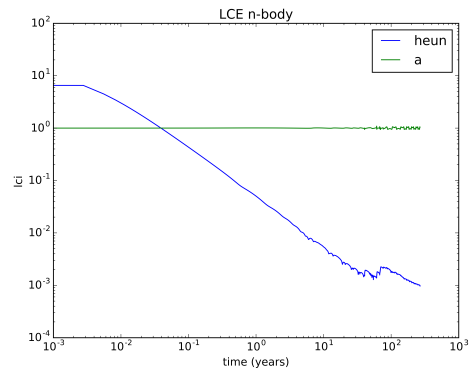


(b) Time evolution of Lyapunov indicator for Trojan 1

Figure 31: Unstable configuration: This figures show the histogram of the local Lyapunov indicators as well as the time evolution of the Lyapunov indicator of the first Trojan planet for an unstable configuration.



(a) Histogram of local Lyapunov indicators for Trojan 2

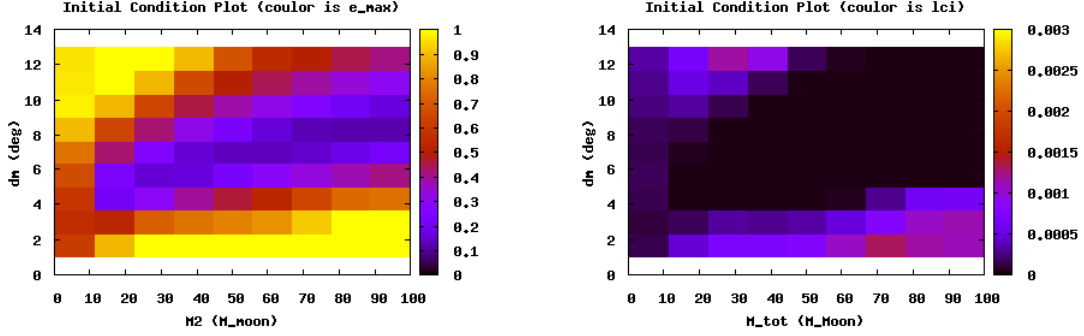


(b) Time evolution of Lyapunov indicator for Trojan 2

Figure 32: Unstable configuration: This figures show the histogram of the local Lyapunov indicators as well as the time evolution of the Lyapunov indicator of the second Trojan planet for an unstable configuration.

The next step is to compare the derived stability indicator with the maximal relative eccentricity. Over a coarse grid in the initial condition plot simulations are conducted and for each combination e_{max} as well as λ_{max} (LCI) values are calculated. Figure 33 shows that the stable areas in both maps are the same. We conclude that the Lyapunov indicator is able to reproduce the stability regions in the initial condition plot. Nevertheless, the calculation time for the Lyapunov indicator is much higher than the calculation time of e_{max} . The differences are significant with the Lyapunov indicator taking ≈ 30 times as much time. The main reason is that

the output interval of the simulation in the case of the Lyapunov indicator has to be small (≈ 1 day) in order to get correct results. In the case of e_{max} an output interval of 50 days still does not change the results drastically. For this reason the e_{max} -indicator is used for the stability maps.



(a) Initial condition plot with e_{max} as stability indicator.

(b) Initial condition plot with λ_{max} as stability indicator.

Figure 33: Comparison of initial condition plots for e_{max} and λ_{max} as stability indicators. Both indicators show the same stable area.

6.11 Conclusions

It was possible to express equations for calculating the Lyapunov indicator via two different approaches. The mapping-approach has been tested on the standard map, which ensures the serviceability of this method. The Hamiltonian-approach was applied to the Henon-Heiles system as well as an the n-body Hamiltonian. The findings are discussed here.

6.11.1 Mapping-Approach

It was shown that it is indeed possible to use the method described in section 6.3 for the calculation of the maximum-Lyapunov-characteristic-exponent for the Lie-series n-body integrator algorithm. The main challenge is to express the Jacobian in form of recursion relations. For different algorithms like the Euler-algorithms and RK-algorithms the integration-step (equation 48) can be explicitly written down relatively easy and therefore the calculation of the Jacobian is not a hard task. The explicit relations for the Lie-series can be used to express the Jacobian but after the 3.th order of the series the analytical terms are getting overwhelmingly long and complicated. For numerical applications it is of great importance to keep the expressions as simple as possible due to the reduction of the algorithm's efficiency for longer expressions. A problem when using the mapping-approach for the calculation of the Lyapunov-characteristic-exponent is furthermore the complexity of the implementation of the Jacobian in the code due to its recursive nature.

6.11.2 Hamiltonian-Approach

The second approach to discuss is the Hamiltonian-approach. This method can be applied independently of the n-body integrator. The information needed is the Hamiltonian of the n-body problem which is always known. It is a moderately difficult task to express the Hessian of the Hamiltonian which is needed to calculate the time derivative of the deviation vector. For the calculation of the Lyapunov indicator the necessary information for the Hamiltonian-approach are the positions of the bodies as well as their masses. Hence the Hamiltonian-approach can be applied without knowing anything about the n-body integrator itself. A problem can be that the time-steps of the output are too large which increases the uncertainties in the calculation of the Lyapunov indicator. In the tested system the time-step was as small as 1 day which increases the computation time and file size. Already time-steps of 5 days were not capable of calculating the Lyapunov indicator correctly anymore.

6.11.3 Comparison of the Two Approaches

When comparing the two approaches for the n-body system, following different characteristics are found:

- Complex implementation of the Jacobian for the mapping-approach.
- Relatively easy calculation of Hessian-Matrix for Hamiltonian-approach.
- Mapping-approach has to be directly implemented in the Lie-series code.
- Hamiltonian-approach only needs output of the integrator. The LCE calculation is independent of the integrator. This requires a small output interval.

The conclusion is that the usage of the Hamiltonian-approach is recommended due to its easier and more general implementation.

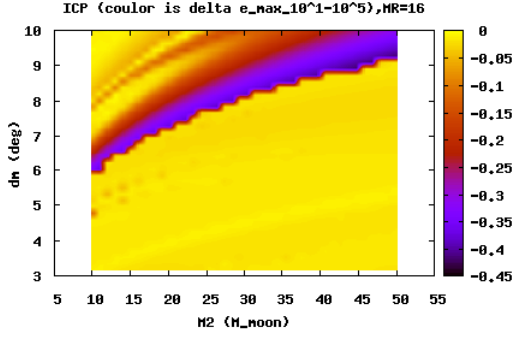
7 Results

7.1 Integration Time

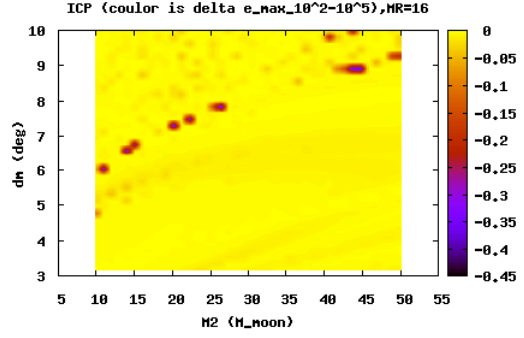
An important parameter of the integration is the integration time itself. Ideally the simulations should run as long as possible ($T_{int} \Rightarrow \infty$) to obtain smaller errors for the stability indicators. This is of course not practicable. We have to find a reasonable integration time with a manageable truncation error. The values of the maximal relative eccentricity of many initial conditions for different lengths of integration are compared. The results are shown in figure 34. Four integrations are compared to the reference value of 10^5 years. The used mass-ratio for all calculations is $MR = 16$. The plots show the difference of the e_{max} value relative to the longest integration time (10^5 years). The shortest depicted integration (chart a, $T = 10$ years) is not capable of reproducing the border area correctly but already integrations of 100 years show little deviations from the results of the longest integration.

Apart from the inaccuracies at the border slight shades indicating errors in the stable and unstable areas are found. These deviations are reduced even more when the integration time is increased to 10^3 years.

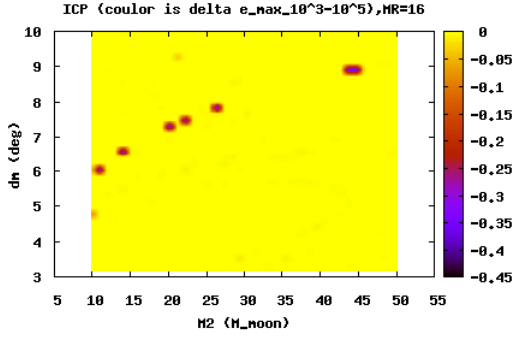
At 10^4 years the only remaining deviations are single calculations exactly around the border of the stable and unstable region. A possible quantitative analysis of the runs can be achieved by forming the average of the absolute deviations across all parameters - $\bar{\Delta}_t = \frac{1}{N} \sum_{i=1}^N |e_{max,i,10^t} - e_{max,i,10^5}|$ - a good estimate of the stability indicator quality. By calculating $\bar{\Delta}_t$ for different integration times figure 35 is obtained. The biggest decrease in the cumulative error occurs for the step from an integration time $T = 10$ years to $T = 100$ years. For further increases of the integration time the error changes only slowly and insignificantly. The standard integration time chosen - in order to obtain usable results within a reasonable time - is $T = 10^4$ years.



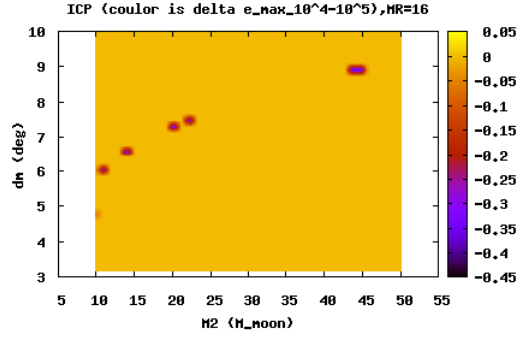
(a) Initial condition plot for differences at integration time of $T = 10^1$ years



(b) Initial condition plot for differences at integration time of $T = 10^2$ years



(c) Initial condition plot for differences at integration time of $T = 10^3$ years



(d) Initial condition plot for differences at integration time of $T = 10^4$ years

Figure 34: For different integration times distinct values of the stability indicator are obtained. The real values would be the ones the system assumes for $t \rightarrow \infty$, which is not computable. An estimate for this value of the stability indicator is the value achieved for long-time integrations. In this case $T = 10^5$ years are chosen as reference. These figures show the difference of e_{max} for different integration times (a: $T = 10^1$ years, b: 10^2 years, c: 10^3 years, d: 10^4 years) to the reference value. The extremely short integration time of 10 years is not capable of reproducing the border area correctly. For longer integration times only a few calculation are different from the 10^5 years-run.

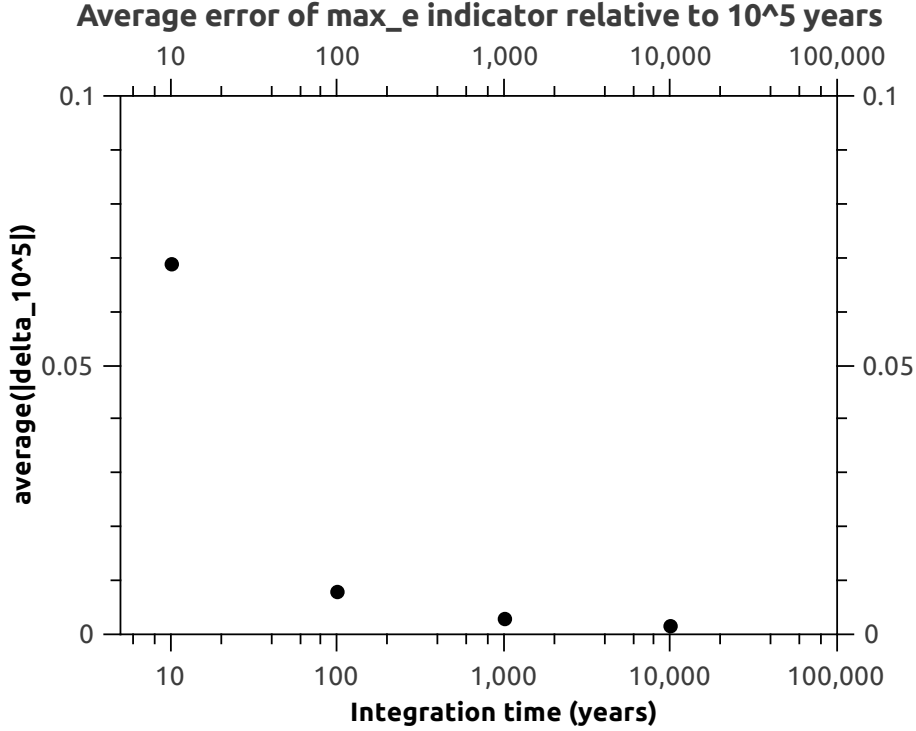


Figure 35: The averaged absolute error of the e_{max} stability indicator relative to the integration time of $T = 10^5$ years ($\bar{\Delta}_t = \frac{1}{N} \sum_{i=1}^N |e_{max,i,10^t} - e_{max,i,10^5}|$) shows a rapid decline with increased integration time. Almost no further improvement is achieved by increasing the integration time further from 10^4 years.

7.2 Grey Area

When recalling figure 14 it was already mentioned that a gap in the values of the maximal relative eccentricity occurs for values between $\approx 0.7-1.0$. When conducting a better resolved investigation of the border region for fixed Trojan masses one obtains results as seen in figure 36. The angular distance is varied and the e_{max} -indicator is calculated for each distance. Now not only the gap in the values but also a spreading out of the border region is clearly accessible. This region is denoted as "grey area" since no statements about the system's stability can be made.

A classification between heavily chaotic (from $\approx 3.33^\circ$ up to $\approx 3.365^\circ$) and weakly chaotic (from $\approx 3.305^\circ$ up to $\approx 3.37^\circ$) behavior is helpful.

It gets even more interesting when conducting high resolution simulations of the border itself. In figure 37 the border region with a width of 0.4° in the angular separation and a mass-range of $10.0 - 13.0M_{Moon}$ for the first Trojan at a mass-ratio of $MR = 16$ is displayed. In this two dimensional parameter plot a "grey area" is also formed. The border is not at distinct values but is spread over a range of parameters. Almost a line of stable configurations is observed slightly within the

unstable region. Nevertheless, it is not of continuous nature. Furthermore it is found that in the stable region of the initial condition plot unstable stripes occur which are almost parallel to the actual stability border. These stripes are probably caused by resonances. We will later identify further structures in the initial condition plot with similar structures.

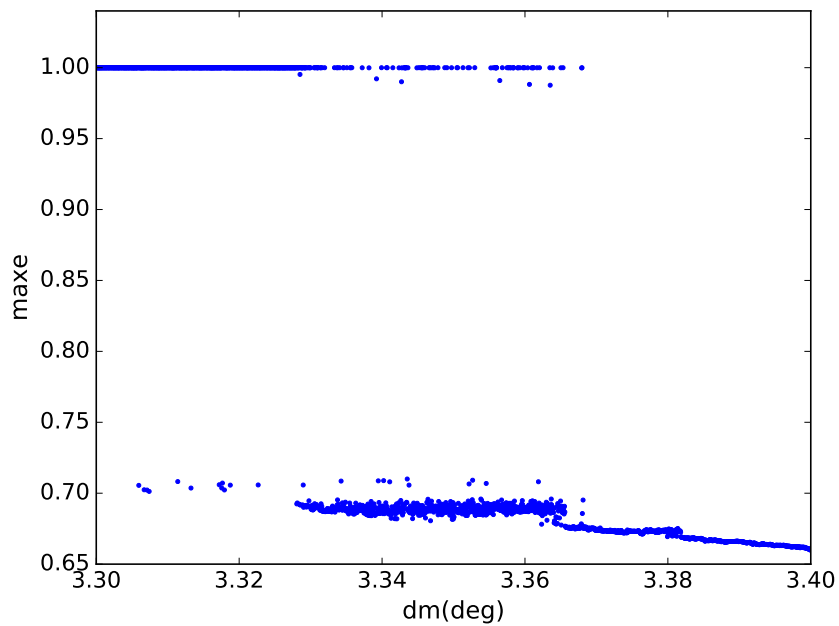


Figure 36: This plot shows the border area of an initial condition plot for a fixed mass. The mass of each Trojan is $50M_{Moon}$. The angular distance is varied around the region of the border and the system is integrated for $T = 10^4$ years. A gap in the values of the eccentricity is observed. Also, the border is not at a particular point but is spread out over a larger interval of angular distances.

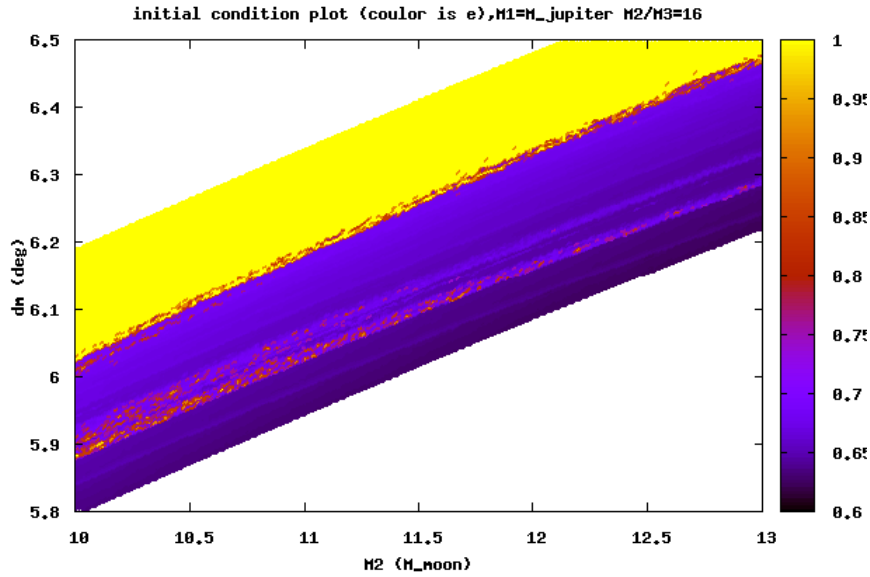


Figure 37: The initial condition plot at the border area with a high resolution grid shows many substructures around the "grey area" as well as the interior of the stable region. The border itself shows almost a "line" of stable configuration in the unstable area. The blue area contains stripes of unstable configurations which are, except for a slight curvature, following the general form of the stability border. For the white region no calculations were conducted.

7.3 Long Term Stability

Long term stability is a highly debated topic in astrodynamics. When habitability is of concern long, term stability is a crucial criterion for the formation of life on a planet. The earth has an age of $4.5 \cdot 10^9$ years ([2]) and life is found on earth at least for the last $3.5 \cdot 10^9$ years ([39]). We can hence assume a necessity of at least several hundred millions of years in which the conditions of the planet should not vary much in order to be able to develop life.

One big problem with relatively short simulations is that long term influences like secular resonances are not considered. It is even more striking when using a proximate stability indicator like e_{max} where we are not able to give any estimates of the duration of the system's future stability. It is different when using quantities like the Lyapunov indicator: the inverse of the Lyapunov indicator is the so-called Lyapunov time and it describes for how long the system is predictable in its behavior. This gives us a clear estimate of the future behavior. Since only proximate stability indicators are used also long term simulations of single configurations as substitution are conducted.

We choose an integration time of 10^8 years for the Trojan twin system with a total mass of $M_{tot} = 0.62M_{Earth}$, $MR = 1$ and $dm = 6^\circ$. The results of the integration can be seen in figure 38. The figure shows the time evolution of the Trojan twins distances to the Jupiter as well as the eccentricities of the Trojans. It is clearly visible that the amplitude of the eccentricity oscillation is decreasing over the integration time for both Trojans. This indicates that initially the system was not in a relaxed state and chosen parameters are not the ones with the highest stability. The ideal value for the angular separation would be $dm = 5.2^\circ$. The maximal relative eccentricity over the integration time is $e_{max} = 0.133$.

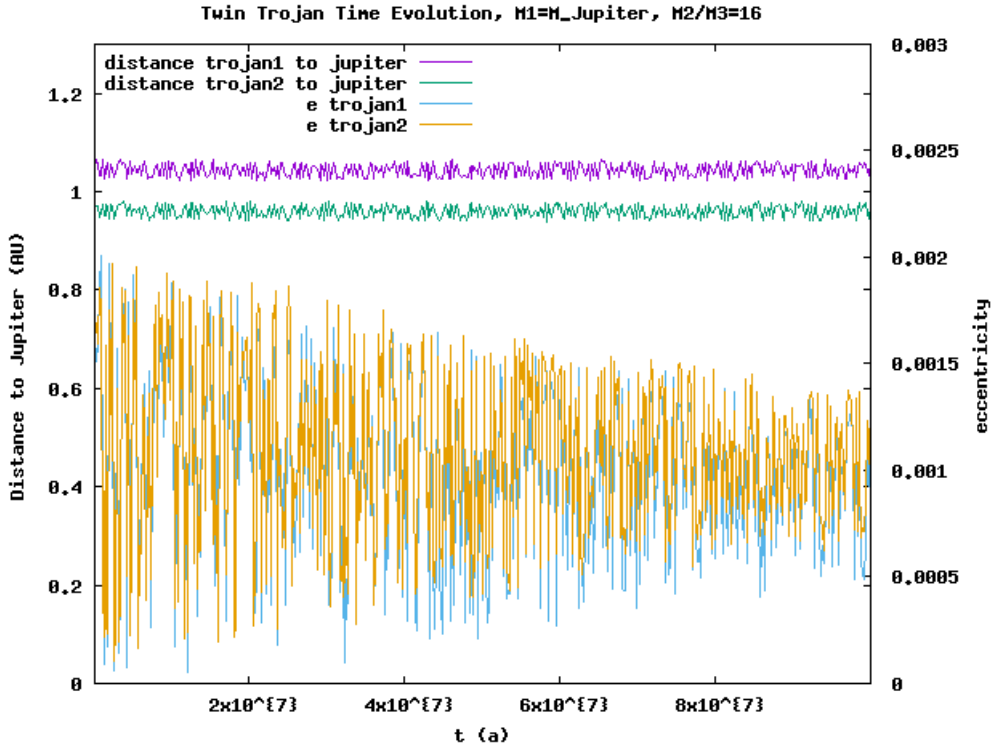


Figure 38: The long term evolution of the Trojan twin planets. The chosen parameters of the simulation are a total mass of $0.62M_{Earth}$ at an angular separation of $dm = 6^\circ$ and $MR = 1$. The integration time of the system is 10^8 years. The plot shows the distances of the individual Trojans to the gas-giant (violet and turquoise) as well as the eccentricities of the Trojans (light blue and yellow). The system is stable over the whole integration time. Interestingly, even a decrease of the Trojans eccentricity is observed.

The conclusion is that long term stability for Trojan twins is indeed expectable. Unfortunately, it is not possible to conduct long time integrations over a parameter grid due to the high computation time needed but individual simulations support the existence long term stable configurations.

7.4 The Valley of Stability

All dm - M_{tot} initial condition plots have a feature of great interest. A clearly visible minimum of the stability indicator can be observed (compare figure 15 c). One is inclined to plot these minima and compare their position for different mass-ratios. To make the mass values on the x-axis comparable the total mass of the two Trojans is chosen as parameter. The maximal total mass is $200M_{Moon}$ which corresponds to $\approx 2.5M_{Earth}$. The total mass is then splitted between the twins according to the mass-ratio. The results of the fits are shown in figure 39.

The first observation is that the general form and position of the minima is approximately the same, independent of the mass-ratio. Upon closer inspection there is a slight variation of the positions of the minima depending on the mass-ratio. This effect is getting more important for higher total masses.

Mass-ratios smaller than one ($MR < 1$) tend to be more stable for higher values of angular separation than configurations with mass-ratios greater than one ($MR > 1$). For the sake of visibility only five mass-ratios are depicted, but the trend still applies to the omitted mass-ratios. Keep in mind that the angular distance of the individual Trojans to $L4$ is determined by the mass-ratio $MR = \frac{M_1}{M_2}$ and the total angular separation dm . The initial position of the Trojans is barycentric. In order to calculate the position of the Trojans barycentrically, equation 81 is applied. l_1 and l_2 are the absolute angular separations of the Trojans from $L4$ respectively.

$$M_1 l_1 = M_2 l_2 \quad (81)$$

We can use $dm = l_1 + l_2$ and equation 81 to express the angular distance of the first Trojan to the Lagrangian point $L4$ and obtain equation 82 as well as the angular separation of the second Trojan (equation 83).

$$l_1 = \frac{dm}{(MR + 1)} \quad (82)$$

$$l_2 = dm - l_1 \quad (83)$$

The barycentric positioning of the Trojans is conducted in order to increase the similarity of the Trojan twin planets to the restricted three-body problem. The general idea is that the barycenter positioned in the Lagrangian point increases the overall stability of the system.

The visualization of the barycentric positioning (40) for $MR = 1 : 10$ and $MR = 10$ shows the big impact on the positions especially for extremely small and large mass-ratios. It is easily understandable why different mass-ratios are expected to have different stable parameter combinations. The most important parameter is the angular separation dm . When recalling the structure of the equipotential lines in figure 1, their tadpole-like structure around the triangular Lagrangian points can be seen. The head is pointed towards the gas-giant and the tail is pointing away from the giant-planet. The tail is much more elongated compared to the head. Having

this picture in mind it is understandable that configurations where the Trojan planet with the higher absolute angular distance from L_4 is also farther away from the gas-giant are the ones stable for larger angular distances dm . The opposite is true for configurations where the bigger angular separation from L_4 is maintained by the planet closer to the gas-giant. It is expected that the stable total angular separation, preferred in terms of stability, is of smaller magnitude. The first is the case for mass-ratios smaller than one ($MR = \frac{M_1}{M_2} < 1$) where the body of the larger angular separation is Trojan 1. We expect the valley of stability at higher values of angular separation. This is indeed the case as seen in figure 39. The opposite is true for $MR > 1$. We expect smaller angular separations to be stable.

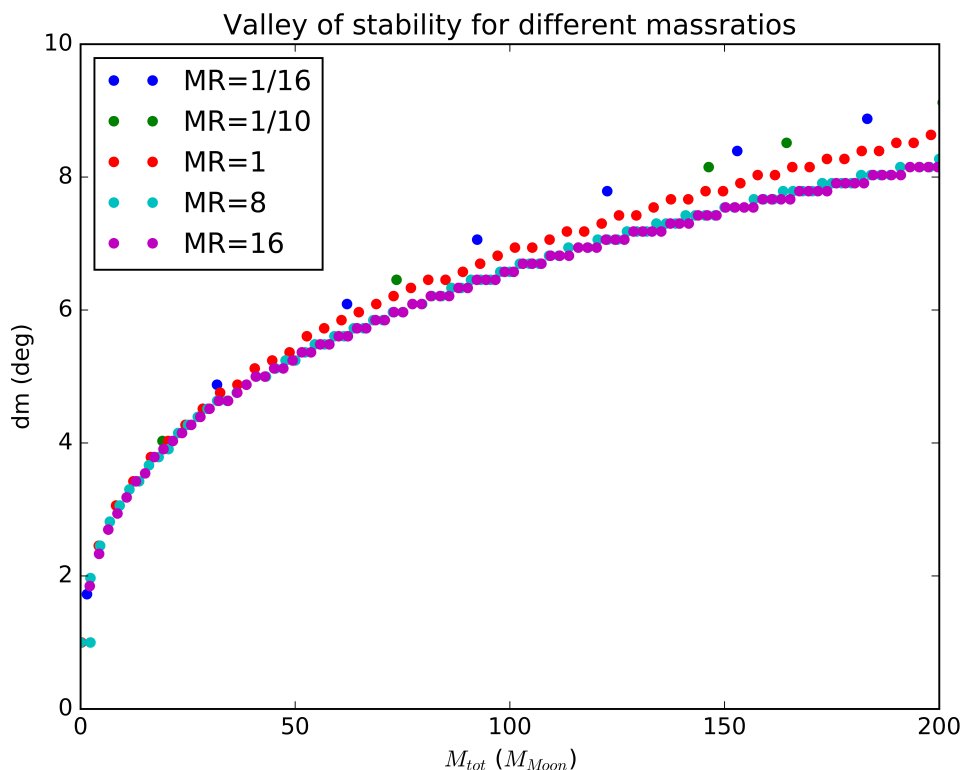


Figure 39: The positions of the valley of stability are obtained by finding the minima of the maximal relative eccentricities in the initial condition plot for each value of the Trojans total mass. For different mass-ratios the position of the minima is shifted. A general trend is that the valley of stability for mass-ratios smaller one ($MR > 1$) lies at higher values of angular separation than for mass-ratios greater one ($MR > 1$).

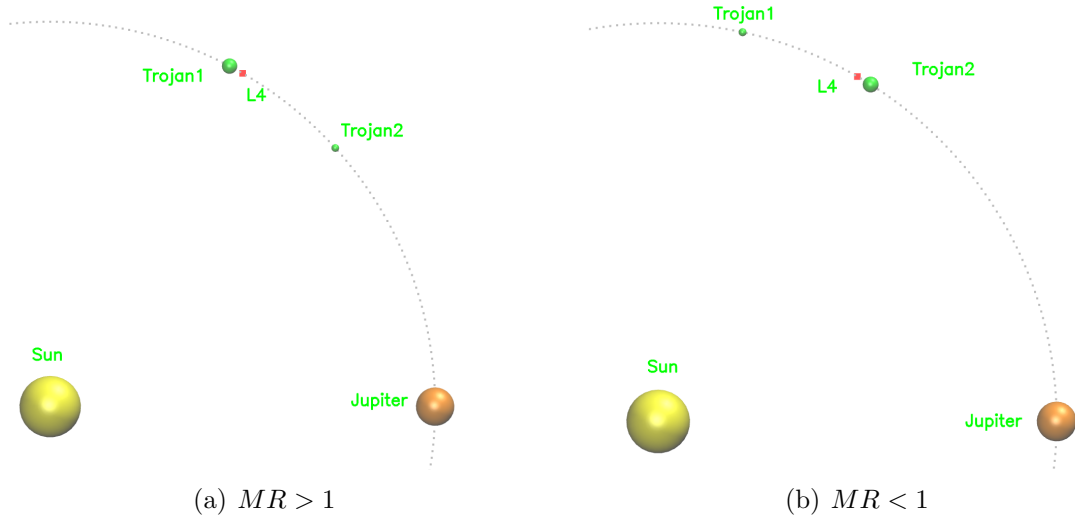
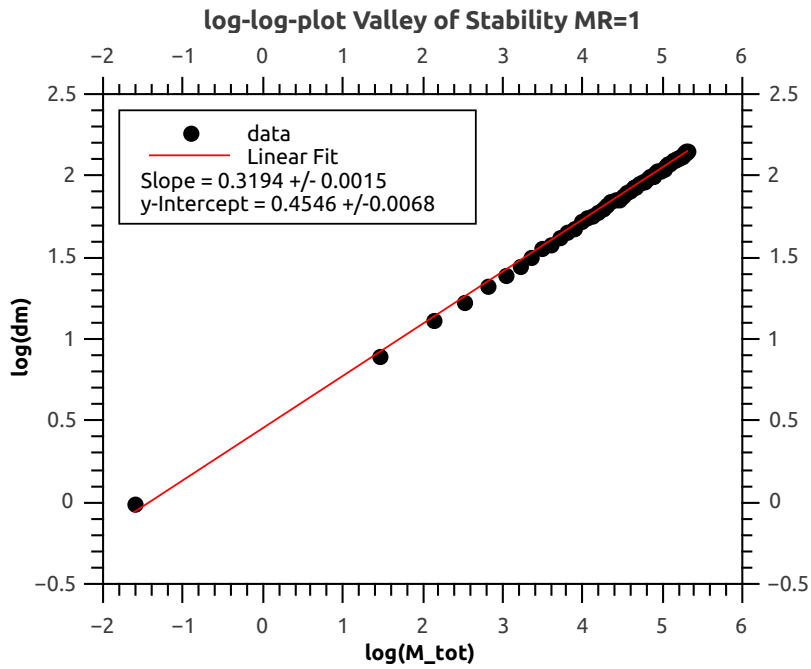


Figure 40: The barycentric positioning of the Trojan twin planets leads to asymmetric configurations of the system for mass-ratios smaller one and mass-ratios greater one even if the total mass of the objects is the same. In the case of $MR < 1$ the first Trojan is lighter than the second one. Hence the position of the second Trojan is closer to the Lagrangian point $L4$ than the position of the first Trojan. The opposite is the case for inverted mass-ratios. This asymmetry in the positions of the Trojans has a moderate but not neglectable impact on the stability of the Trojan system and the position of the stable region in the initial condition plot.

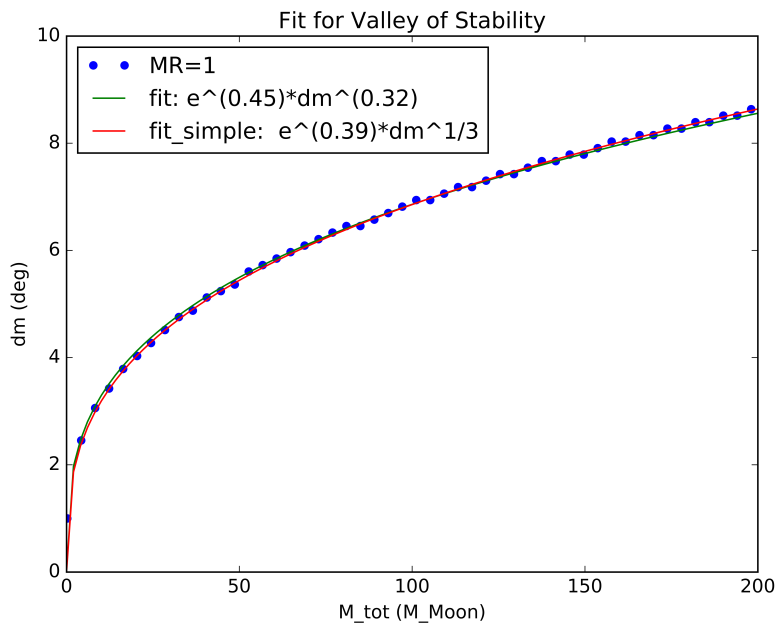
As the similarities of the position of the minima in the initial condition plot for different mass-ratios are striking it seems like the general trend can be explained by expressing dm as function of M_{tot} . Figure 41 shows fits applied to the "valley of stability" for $MR = 1$. One finds that the position of the minimum in terms of angular separation is proportional to the third root of the total mass of both Trojans (see equation 84).

As discussed before there is a slight deviation from of the position of the minimum depending on the mass-ratio. This could be considered when instead of using a mono-parametric fit also the mass-ratio as second parameter of the fit is included.

$$dm(^{\circ}) = 1.477M_{tot}(M_{Moon})^{1/3} \quad (84)$$



(a) Log-log-plot with linear fit



(b) Two different fits in comparison to the fitted data

Figure 41: These plots show fits for the valley of stability at a mass-ratio $MR = 1$. The first plot depicts the minimum of the initial condition plot with $\log(M_{tot})$ on the x-axis and $\log(dm)$ on the y-axis. A linear fit is applied to the data. The fit is plotted again with the data in figure b and with linear scaling including a second fit $\propto M_{tot}^{1/3}$.

7.5 High Mass Twins

In the theoretical part it was already discussed what the mass limit for Trojan objects is. We found that the general limit for the Trojan twin planets is given by equation 85 where M_1 denotes the mass of the star, M_2 the mass of the gas-giant and M_3, M_4 the masses of the Trojans.

$$\frac{M_2 + M_3 + M_4}{M_1} < \frac{1}{27} \quad (85)$$

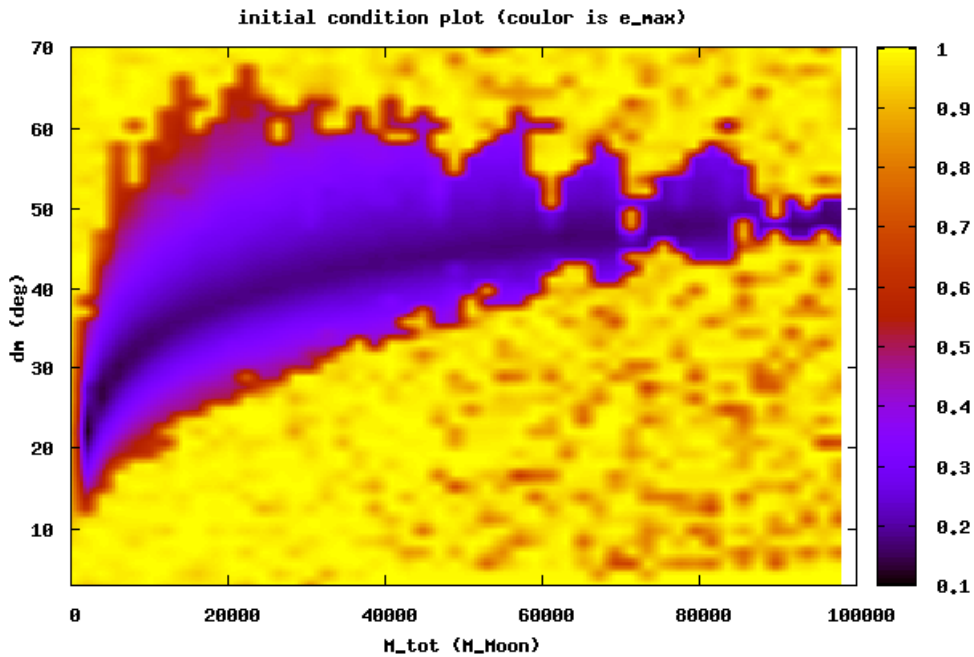


Figure 42: This initial condition plot show that the behavior observed for small masses ($\approx M_{Earth}$) is still obtained for extreme masses of up to $10^5 M_{Moon}$, especially concerning the form of the valley of stability. In the small mass regime an increasing mass of the Trojans corresponds with a broader stable angular separation range. This changes at about $\approx 23000 M_{Moon}$ ($0.89 M_{Jupiter}$) where the stable region is becoming thinner with increased mass of the Trojans.

Figure 42 shows the initial condition plot up to masses of $10^5 M_{Moon}$ which corresponds to a total Trojan mass of $3.87 M_{Jupiter}$. Astonishingly, for masses this high stable configurations are found. Nevertheless, the parameter range is drastically reduced and the thickness of the stability zone is only several degrees in angular separation. At extreme masses it is not expected that the configurations are long

term stable. Simulations show that it is hard to achieve stability for longer than some ten thousand years for $M_{tot} = 10^5 M_{Moon}$. It is worth to mention that the form of the valley of stability does not even change for high masses. The main difference to the low mass initial condition plot is that for a lower mass-regime with increasing masses the range of the stable parameters increases. This is only true for masses up to $\approx 23000 M_{Moon}$ ($0.89 M_{Jupiter}$). For higher masses of the Trojans the stable zone again narrows down to only some degrees. It is improbable that configurations like these where three Jupiter-like planets share the same orbit will ever be observed. It is more of a pure theoretical task to identify the limits for the Trojan twin planets. A work analyzing the stability of similar configurations is [12]. Figure 43 shows three different configurations with bodies of same mass from which only the left one is stable. In figure 42 the stable configuration where all bodies have the same mass is found for $dm \approx 40^\circ$. This corresponds at $MR = 1$ to $\Theta_1 = \Theta_2 = 40^\circ$ (Θ_1 and Θ_2 are the two angles between the three bodies on a circular orbit) not far away from $\Theta_1 = \Theta_2 = 47.36^\circ$ found in [12].

For a single Trojan a possible candidate of a Trojan planet was discovered in a Kepler data release. The planets KOI-730.02 and KOI-73.03 were originally thought to be in a 1:1 MMR ([7]). Further investigations showed that it is not probable and another interesting configuration of a system completely in MMR was suggested ([32]). The radii of the planets are $3.4 R_{Earth}$ and $4.6 R_{Earth}$ respectively, which is in the domain of Uranus and Neptune ([32]). It is in that observers in astronomy are already considering Trojan planets as a valid interpretation of data even in the mass regime of Uranus.

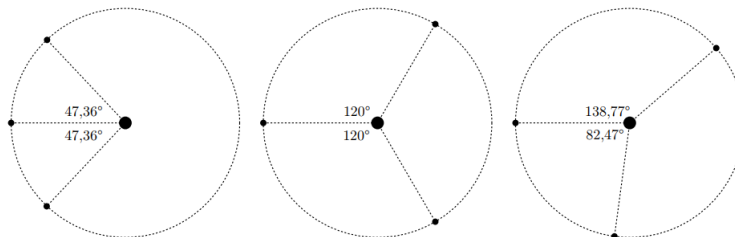


Figure 43: This figure from [12] shows three different co-orbital configurations for bodies of the same mass. Nevertheless, only the left configuration gives stable solutions.

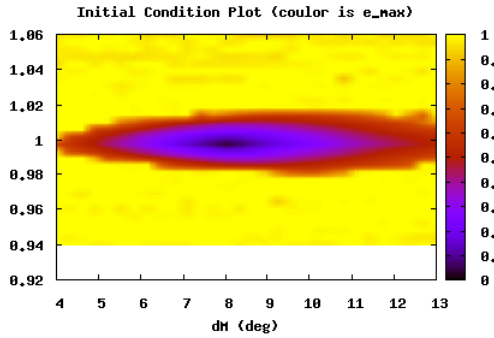
7.6 Change of the Semi-Major Axis of Gas-Giant

We have until now not considered changes of the semi-major axis of the planet. This could occur during events like migrations, close encounters or collisions, where the orbital parameters are changed drastically. In order to quantify the tolerance of the Trojan twin planets to changes of the semi-major axis the gas-giant for this section is not positioned on the same orbit as the Trojans. These changes are of course not

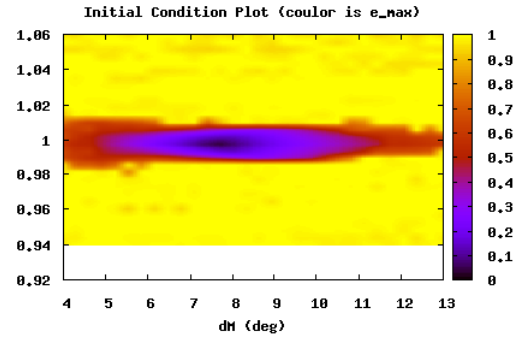
major ones and in the magnitude of hundredths of an astronomical unit.

Figure 44 shows the stability behavior for three different mass-ratios. In all cases for changes of approximately $\pm 0.02AU$ stable configurations are observed. The width of possible angular distances on the other hand narrows down by increased Δa .

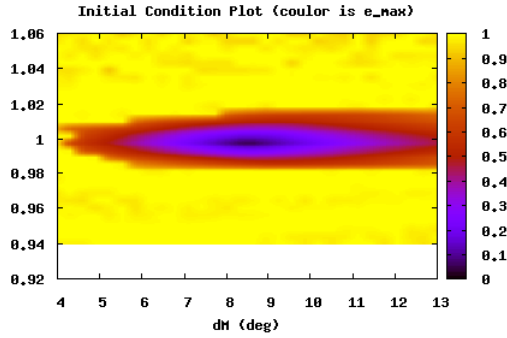
Figure 44 a depicts the initial condition plot for a mass-ratio $MR = 1$. The shape of the stable area is almost symmetrical in both x and y-axis. This changes for different mass-ratios. The initial condition plot's stable area for $MR = 16$ is extended towards small angular distances and opposite to $MR = 1/16$.



(a) Initial condition plot with e_{max} , mass-ratio $MR = 1$



(b) Initial condition plot with e_{max} , mass-ratio $MR = 16$



(c) Initial condition plot with e_{max} , mass-ratio $MR = 1 : 16$

Figure 44: The robustness of the Trojan twin planets is tested by changing the initial semi-major axis of the gas-giant. These diagrams show the initial condition plot where the angular distance dm is plotted against the semi-major axis a . The maximum change in the semi-major axis to still obtain a stable system is about $\pm 0.02AU$. Nevertheless, also the region of stable angular distances is reduced.

We want to have a closer look at the initial condition plot for the mass-ratio $MR = 1$ to identify possible substructures in the plot. Figure 45 has a higher resolution in the parameters (total of 40000 simulations). It is possible to find tail-

like structures for higher values of the angular distance. For small values of the angular distance these substructures are not found.

It is an interesting question if these structures are a phenomenon only observed for the Trojan twin planets or if these tails are also visible in the restricted three-body problem. Of course In the r3bp there is no angular separation parameter but a comparable one is the bodies initial position around the Lagrangian point. Similar results are expected for high values of the angular separation and high displacements from the Lagrangian point $L4$. The comparison of two such plots (figure 46) indeed show similarities. In the case of the r3bp the tails are so-called escape orbits where the Trojan can be ejected from the system.

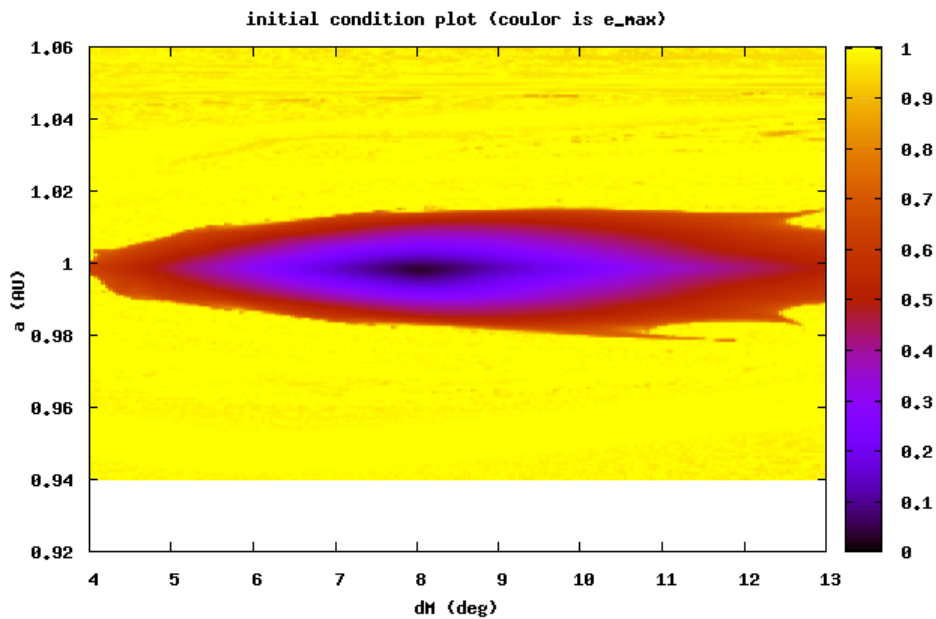
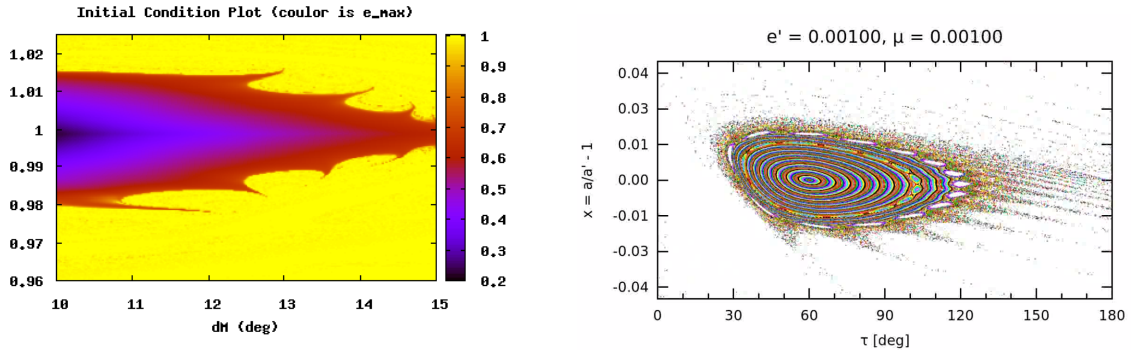


Figure 45: This figure shows a higher resolved initial condition plot with $a_{Jupiter}$ on its y-axis for the mass-ratio $MR = 1$. Substructures not found in the prior figures with lower resolution (fig. 44) are now visible.



(a) Initial condition plot e_{max} , mass-ratio $MR = 1$

(b) Trajectories of r3bp for $\mu = 0.001$ for different initial values

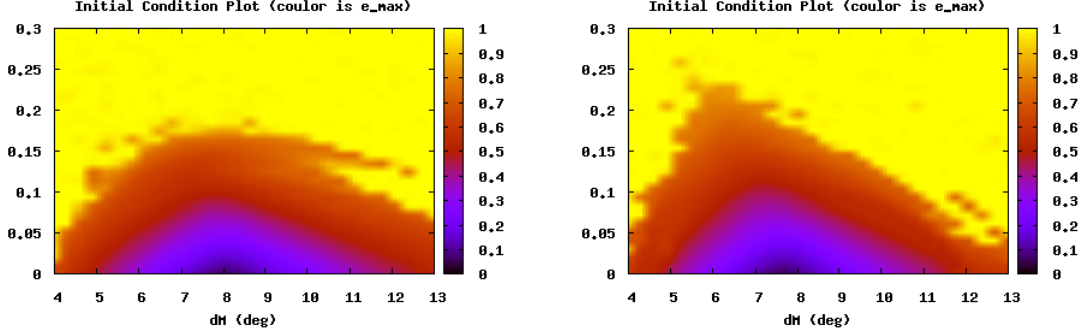
Figure 46: Comparison of a high resolution initial condition plot with $a_{jupiter}$ on the y-axis with a plot showing the stable trajectories for the restricted r3bp. The tails observed are escape orbits where the Trojans are ejected. Source of the figure on the right-hand side is unpublished work of Akos Bazso.

7.7 Change of the Gas-Giants Eccentricity

When considering real planetary systems the eccentricity of the gas-giant cannot be longer neglected. For an exoplanet with $M = 1.0 \pm 0.1 M_{Jupiter}$ the mean eccentricity of all found exoplanets is 0.09 ± 0.14 ($N = 67$, data from exoplanet.eu/catalog). We conclude that relatively high eccentricities are common in exoplanetary systems. This section discusses the impact of eccentricity of the gas-giant on the stability of the Trojan twin planets. In the following simulations the eccentricity of the gas-giant is changed whereas the eccentricity of the Trojans remains at zero. Furthermore, as second parameter the angular separation of the Trojans is changed. The results are plotted in figure 47 where the color code represents the e_{max} stability indicator. The total mass is $M_{tot} = 2M_{Earth}$ for all three mass-ratios.

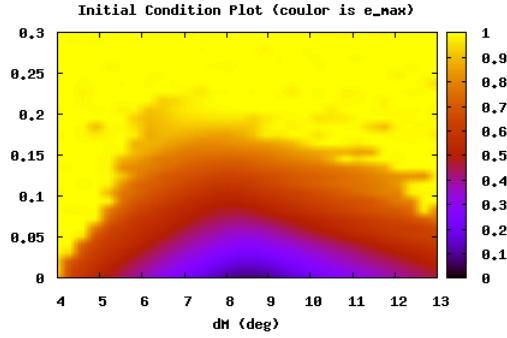
- $MR = 1$: One finds that for $MR = 1$ an increased eccentricity narrows down the stable area in the initial condition plot. The maximal possible eccentricity for the giant planet to maintain stable Trojan twins is approximately 0.17. The structure seems to be symmetrical except from an arm-like structure splitting away from $dm = 9^\circ$ on towards higher values of angular separation. For $e = 0$ the lowest value of the stability indicator is found at $dm = 8.0^\circ$.
- $MR = 16$: When increasing the mass-ratio to $MR = 16$ the initial condition plot becomes more asymmetrical. The stability border for high eccentricities is now shifted towards smaller values of angular separation. The highest possible value of the gas-giant's eccentricity is increased from $e = 0.17$ for $MR = 1$ to $e = 0.23$. The lowest value of the stability indicator for $e = 0$ is attained at $dm = 7.7^\circ$.

- $MR = 1 : 16$: On the other hand, the initial condition plot for $MR = 1 : 16$ does not seem different from the one of $MR = 1$. The main differences are the missing arm-like structure and a more washed out stability border. The lowest value of the stability indicator for $e = 0$ is attained at $dm = 8.5^\circ$.



(a) Initial condition plot with e_{max} -indicator, mass-ratio $MR = 1$

(b) Initial condition plot with e_{max} -indicator, mass-ratio $MR = 16$



(c) Initial condition plot with e_{max} -indicator, mass-ratio $MR = 1 : 16$

Figure 47: The initial condition plot with the angular separation of the Trojan twin planets on the x-axis, the eccentricity of the gas-giant on the y-axis and the e_{max} stability indicator as color code. The total mass of both Trojans in all three plots is $M_{tot} = 2M_{Earth}$ and the mass of the gas-giant is $1M_{Jupiter}$. The presented calculations are for $MR = 1$, $MR = 16$ and $MR = 1 : 16$ respectively.

In order to obtain better results simulations with higher resolutions are needed. This is especially true for the substructure already observed in figure 47 a. Almost certainly, further interesting structures would be visible when reducing the step-size of the parameter grid. Another problem can be the short integration time of 1000 years which effects the results especially at the regions of the stability border.

Shorter integration times generally lead to overestimations of the stable area. Nevertheless, the prior analysis of the integration time truncation error (see figure 35) showed that the results are already reliable at the chosen integration time.

7.8 Additional Gas-Giant

It is uncommon for planets to occur as lone wolves. It is therefore of great interest to consider further planets in the Trojan twin planetary system. The biggest effect on the stability of planetary orbits have high mass planets. Hence an additional gas-giant with a mass of $1M_{Jupiter}$ is placed in the system as perturbing body. The goal is to study the effect of orbital resonances as well as non-resonant effects of close orbits on the stability of the Trojan twin planets.

Each of the Trojan twins has a mass of $1M_{Earth}$ and the host planets a mass of $1M_{Jupiter}$. The initial angular distance of the Trojan twin planets is 8° , which corresponds to the most stable configuration (compare figure 39) for a total mass of $M_{tot} = 2M_{Earth} = 182M_{Moon}$. The twins have a semi-major axis of $1AU$. We calculate the maximal relative eccentricity as stability indicator for different initial positions of the second gas-giant. The simulation time is 1000 years for three different initial values of the perturbing giant's eccentricity.

The results can be seen in figure 48. In general it is concluded that higher eccentricities of the perturbing giant tend to destabilize the Trojan twin planets more. Only semi-major axis values $a > 1.7AU$ can create stable environments for the Trojan planets at eccentricities of 0.1. Decreasing the eccentricity to 0.05 allows stable configurations down to $a = 1.5AU$ and values of 0.01 even down to $1.4AU$. A general increase of the maximal relative eccentricity is observed the closer the orbits of the two giants get.

The second factor having an impact on the stability of the system is mean motion resonance. The most important resonances are marked by a straight line and with the corresponding ratios in figure 48. Especially in a 1 : 2 resonance the disruption effects on the system's stability are devastating. Another observation is that the width of the peaks is getting larger for higher eccentricities. The implication of these findings are especially interesting when considering habitability. A limit on the compactness of an exoplanetary system when Trojan twin planets are inhabited is found. The effect of minor planets is not examined since the biggest influence on the system is exhibited by a heavy gas-giant.

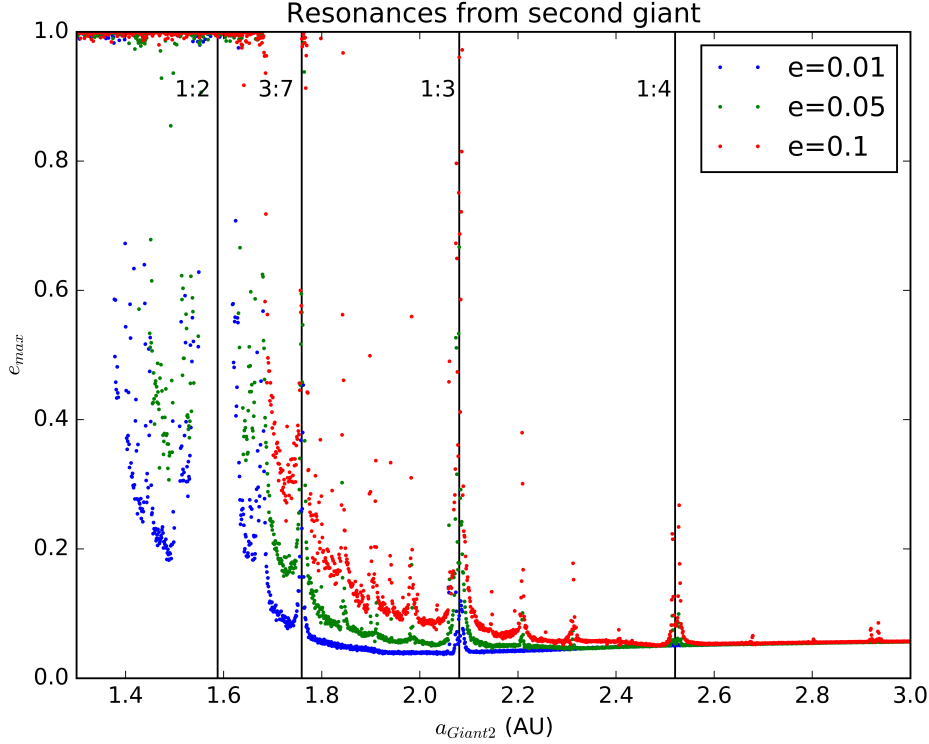


Figure 48: This plot represents the maximal relative eccentricity of the Trojan twin planets each with a mass of $1M_{Earth}$ and in the Lagrangian point $L4$ of a Jupiter at $1AU$ where a second gas-giant with a mass of $1M_{Jupiter}$ is added to the system. The initial angular distance of the Trojans is fixed to 8° . Furthermore, the simulations are conducted for three different initial eccentricities of the second gas-giant. Two effects on the stability of the Trojan planets are observed: The first one is a general increase of e_{max} for closer initial positions of the second gas-giant. The is effect is enhanced for higher eccentricities of the perturbing Jovian planet. Secondly, mean motion resonances are causing instabilities in the system. Also, here a higher eccentricity of the second giant leads to larger disruptions with more extended influenced regions around the resonances.

7.9 Fractal Structures

In this section further investigations on interesting substructures of initial condition plots are presented. It mostly consist of the interpretation of high resolution initial condition plots with smaller parameter ranges. For a mass-ratio of $MR = 16$ a prominent feature is a spike-like structure of stable configurations for low angular separations depicted in figure 49.

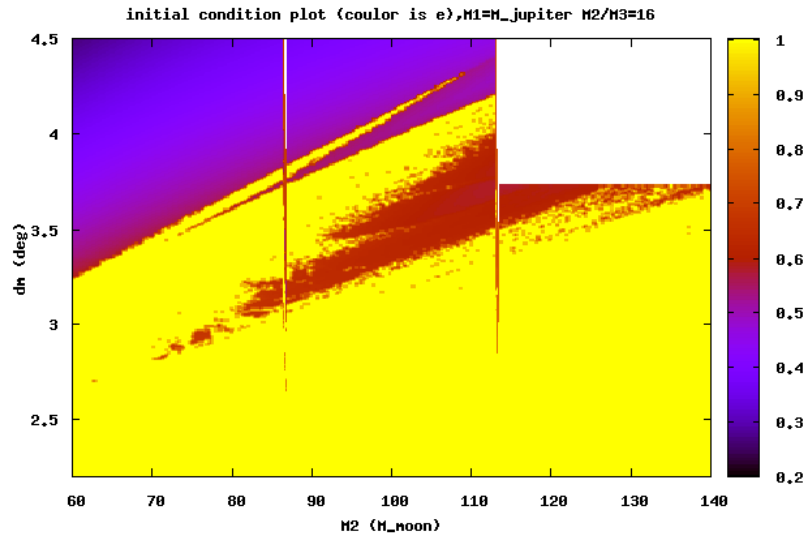


Figure 49: The initial condition plot for $MR = 16$ shows characteristic substructures in form of spikes. For the white region no calculations were conducted.

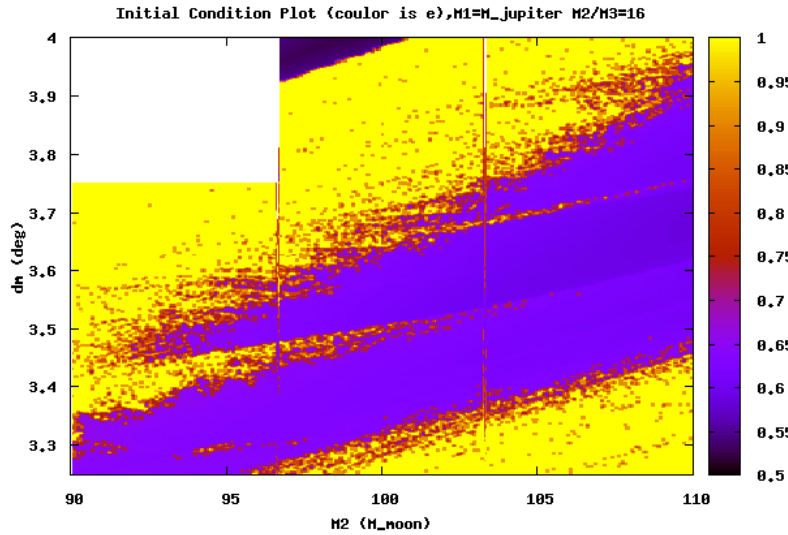


Figure 50: Better resolved simulations show that on the spike-like structure from figure 49 further similar substructures are found, which indicates a fractal behavior. For the white region no calculations were conducted.

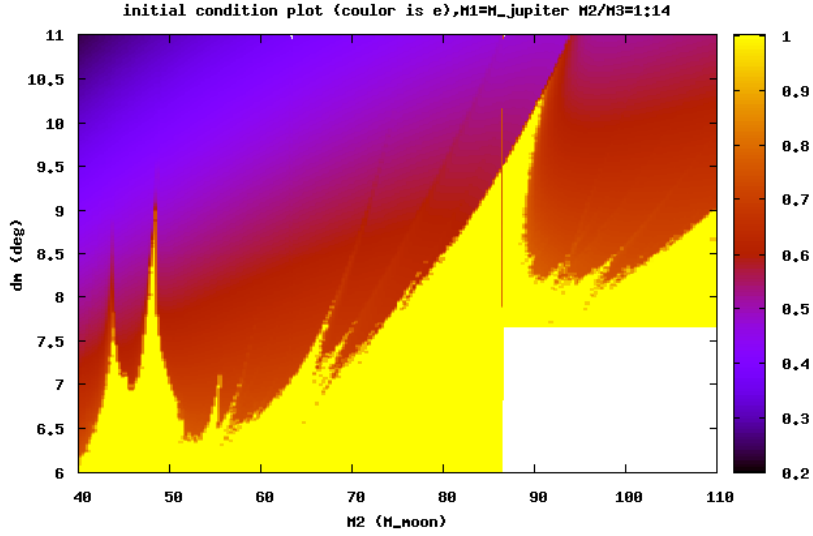


Figure 51: Interesting parameter range for the initial condition plot for $MR = 1/16$. The structures at mass-ratios smaller than one have different shapes from the ones for $MR > 1$. The spikes change to wing-like structures instead. For the white region no calculations were conducted.

Increasing the resolution (figure 50) of the simulation grid reveals that the spike-like structure itself consists of structures of similar form. It seems that these are of fractal nature. A fractal is defined as a structure which has the same form independent of the scale. This means that continuous zooming reveals the same pattern again and again. Probably, the cause of the substructures is the same one as for the tails observed in the initial condition plot for changes of the semi-major axis of the gas-giant in figure 45. Here the angular separation is plotted on the y-axis and a is fixed. The parameter varied is the mass which was prior fixed. A phenomenon which cannot be observed in the r3bp is the change of the patterns in the initial condition plot for different mass-ratios, simply because the bodies have no mass. The form of the fractal structures observed is depending on the mass-ratio (spikes and wings). Further investigations are needed to pin down the reason for the phenomenon.

8 Conclusion

8.1 Lyapunov Indicator

It has been shown that the Hamiltonian-approach is the better way to calculate the Lyapunov indicator for a n-body system. The Hamiltonian-approach was applied first on the Henon-Heiles system. It was possible to identify chaotic orbits and stable orbits by analyzing the histogram of the local Lyapunov indicators, as well as analyzing the time evolution of the Lyapunov indicator. The mapping-approach is not an optimal option for the Lie-series integrator due to the complicated recursive formulation of the Jacobian. Nevertheless, the mapping-approach was applied to the standard-map where it was possible to differentiate stable from unstable initial conditions. The developed Hamiltonian-approach was then successfully applied to the Trojan twin planets.

The calculation of the Lyapunov indicator has the drawback that the print interval of the n-body simulation has to be in the order of days. This produces large files and takes up a lot of computation time. For the calculation of the initial condition plots instead of the Lyapunov indicator the maximum relative eccentricity was used as stability indicator. This was done due to the smaller necessary output interval which speeds up the calculation of the maps by a factor of about 30. Nevertheless, it is the Lyapunov indicator which provides a more profound way of identifying stability. Additionally, it enables predictions - via the Lyapunov time - on the system's stability after the actual simulation itself.

8.2 Trojan Twin Planets

Intensive studies on the Trojan twin planets' stability led to numerous interesting results. The initial condition plots show an area where small changes of the initial parameters are causing big differences in terms of stability. This parameter range is denoted "grey area" since the outcome of a simulation is uncertain. Especially around the stability border, chaotic behavior of the dynamical system is observed consistently. An important result is that the Trojan twin planets can be stable for at least á hundred million years which is especially interesting since the long term stability is a premise for habitability. These simulations were conducted with two identical planets, each having a mass of $1M_{Earth}$ and a semi-major axis of $a = 1AU$ with a host star of one solar mass.

The system's stability strongly depends on initial position and the masses of the twin planets. In the initial condition plot a minimum of the stability indicator, called "valley of stability", is observed. It was found that the ideal angular separation is a function of the total mass of the Trojans. The relation found is $dm \propto M_{tot}^{1/3}$. The relation holds, even up to extreme masses of the Trojans. Configurations of identical Trojans with masses of several Jupiters can be stable for more than $2 \cdot 10^4$ years. Of course the aforementioned is more a theoretical exercise since the occurrence of such systems is highly unlikely. Nevertheless, the findings are consistent with [12]

where stable configurations of three massive planets sharing one orbit are predicted as well.

The influence of sudden alterations of the gas-giants semi-major axis was tested with an initial condition plot where dm is denoted on the x-axis and a is denoted on the y-axis. It was found that changes of up to $0.02AU$ can still yield stable Trojans. Additionally, structures related to escape orbits in the r3bp were found. The influence of changes of the gas-giants eccentricity were examined showing that eccentricities of up to $e = 0.2$ can lead to stable configurations.

Furthermore, the influence of an additional gas-giant in the outer region of the Trojan twin planets was investigated. It was shown that the main destabilizing effects are mean motion resonances. These are manifested by increased values of the stability indicator. Finally, high resolution simulations display many substructures in the system. These structures appear to be of fractal nature.

The conclusion is that a broad parameter range is capable of maintaining the structural integrity of Trojan twin planets. Some configurations are stable for more than a hundred thousand years. This broad parameter range implies that we can expect systems like the Trojan twin planets to be found in extra-solar planetary systems.

Abstract

Ziele: Die vorliegende Arbeit hat die Analyse eines speziellen astrodynamischen Systems zum Ziel, die des Trojanischen Doppelplaneten. In diesem System sind zwei terrestrische Planeten im Lagrangepunkt $L4$ eines Gasriesen zu finden. Die wichtigsten Parameter dabei sind der Winkelabstand der Trojaner dm , die Gesamtmasse der beiden Trojaner $M_{tot} = M_1 + M_2$, sowie das Massenverhältnis $MR = \frac{M_1}{M_2}$. Um Untersuchungen der Stabilität des Systems durchzuführen, werden verschiedene Stabilitätsindikatoren eingeführt. Dadurch ist ein Sekundärziel der Masterarbeit definiert, die Entwicklung eines Codes zur Berechnung des Lyapunov-Exponenten für ein N-Körpersystem.

Methoden: Die Stabilitätsanalysen der Doppel Trojaner werden hauptsächlich durch Simulationen mittels eines Lie-Reihen N-Körper-Integrators durchgeführt. Dies beinhaltet Untersuchungen einzelner Trajektorien sowie die Berechnung von Stabilitätskarten, auch als Initial-Condition-Plots bezeichnet. Die Untersuchung des Lyapunov-Indikators ist zu einem großen Teil von theoretischer Natur. Dabei werden zwei verschiedene Methoden zur Berechnung erörtert. Die erste Methode baut auf der expliziten Form des N-Körperintegrators, in diesem Fall dem Lie-Reihen-Integrator, auf, während die zweite Methode unabhängig vom N-Körperintegrator ist.

Ergebnisse: Es wurde gezeigt, dass die Trojanischen Doppelplaneten einen erstaunlich großen stabilen Parameterbereich aufweisen. Ein Trojanerzwillingssystem, mit jeweils einer Erdmasse im Lagrangepunkt $L4$ eines Jupiters mit $a = 1AU$, kann für zumindest hundert Millionen Jahre stabil bleiben. Desweiteren wurde ein Zusammenhang zwischen dem stabilen Winkelabstand der Trojaner und ihrer Gesamtmasse gefunden ($dm \propto M_{tot}^{1/3}$). Eine moderate Abweichung von dieser Beziehung wird durch ein sich änderndes Massenverhältnis (MR) der Doppel Trojaner erklärt.

Das System bleibt selbst für extreme Konfigurationen, bei welchen die Gesamtmasse der Trojaner im mehrfachen Jupiterbereich liegt, für längere Zeit stabil. Im Speziellen weisen einige Simulationen von Doppel Trojanern mit einer Gesamtmasse von ca. $4M_{Jupiter}$ Stabilitätszeiten von mehr als $2 \cdot 10^4$ Jahre auf. Dies entspricht bei $1AU$ ebensovielen Umläufen der Planeten.

Da Exoplanetensysteme oftmals mehr als einen Gasriesen aufweisen, wurde das System auf Einflüsse eines weiteren Gasriesen überprüft. Es zeigt sich, dass hier vor allem Bahnresonanzen destabilisierend wirken. Bei einer Masse von $1M_{Jupiter}$ sind jedoch ab einer großen Halbachse von $a > 2.5AU$ des störenden Gasriesen keine nennenswerten Effekte mehr nachweisbar.

Ferner wurden bei hochaufgelösten Parameterstudien fraktale Strukturen in den Stabilitätskarten entdeckt. Den größten Einfluss auf die Form der Fraktale hat das Massenverhältnis MR der Doppel Trojaner. Für $MR < 1$ entstehen keilförmige Unterstrukturen, bei $MR > 1$ handelt es sich um kuppelförmige Unterstrukturen.

Es konnten mit Erfolg Lyapunov-Exponenten für zwei Arten von Problemstellungen, Hamiltonische Systeme und Mappings, berechnet werden. Als Beispiel-Mapping wurde die Standard-Map herangezogen, für welche dadurch zwischen chaotischen und stabilen Anfangsbedingungen unterschieden werden

konnte. Im Falle von Hamiltonischen Systemen war es zusätzlich möglich, über Histogramme des lokalen Lyapunov-Indikators, Rückschlüsse über die Stabilität des Systems zu ziehen. Studien des Henon-Heiles-Systems dienten dabei als Vorbereitung für das komplexere allgemeine N-Körperproblem. Die erfolgreiche Anwendung auf ein N-Körpersystem wurde anhand der Doppel-trojaner demonstriert.

Acknowledgements

I would like to thank everybody who supported me with the writing of my master's thesis. Special thanks to Rudolf Dvorak for his supervision, Akos Baszo for materials and his scientific expertise, Andreas Felsenstein for his patient and precise work as well as to my parents who financially enabled my education and always supported my decisions.

References

- [1] Y Alibert, F Carron, A Fortier, S Pfyffer, W Benz, C Mordasini, and D Swo-boda. Theoretical models of planetary system formation: mass vs semi-major axis. Technical Report arXiv:1307.4864, Jul 2013. Comments: accepted in Astronomy and Astrophysics. URL: <http://cds.cern.ch/record/1563008>.
- [2] C. J. Allègre, G. Manhès, and C. Göpel. The age of the Earth.
- [3] C. Beaugé, Z. Sándor, B. Érdi, and Á. Süli. Co-orbital terrestrial planets in exoplanetary systems: a formation scenario. *aap*, 463:359–367, February 2007. doi:10.1051/0004-6361:20066582.
- [4] Giancarlo Benettin, Luigi Galgani, Antonio Giorgilli, and Jean-Marie Strelcyn. Lyapunov characteristic exponents for smooth dynamical systems and for hamiltonian systems; a method for computing all of them. part 1: Theory. *Mec-canica*, 15(1):9–20, Mar 1980. URL: <https://doi.org/10.1007/BF02128236>, doi:10.1007/BF02128236.
- [5] Giancarlo Benettin, Luigi Galgani, and Jean-Marie Strelcyn. Kolmogorov entropy and numerical experiments. *Phys. Rev. A*, 14:2338–2345, Dec 1976. URL: <https://link.aps.org/doi/10.1103/PhysRevA.14.2338>, doi:10.1103/PhysRevA.14.2338.
- [6] Giancarlo Benettin, Luigi Galgani, and Jean-Marie Strelcyn. Kolmogorov entropy and numerical experiments. *Phys. Rev. A*, 14:2338–2345, Dec 1976. URL: <https://link.aps.org/doi/10.1103/PhysRevA.14.2338>, doi:10.1103/PhysRevA.14.2338.
- [7] William J. Borucki, David G. Koch, Gibor Basri, Natalie Batalha, Timothy M. Brown, Stephen T. Bryson, Douglas Caldwell, Jørgen Christensen-Dalsgaard, William D. Cochran, Edna DeVore, Edward W. Dunham, Thomas N. Gautier III, John C. Geary, Ronald Gilliland, Alan Gould, Steve B. Howell, Jon M. Jenkins, David W. Latham, Jack J. Lissauer, Geoffrey W. Marcy, Jason Rowe, Dimitar Sasselov, Alan Boss, David Charbonneau, David Ciardi, Laurance Doyle, Andrea K. Dupree, Eric B. Ford, Jonathan Fortney, Matthew J. Holman, Sara Seager, Jason H. Steffen, Jill Tarter, William F. Welsh, Christopher Allen, Lars A. Buchhave, Jessie L. Christiansen, Bruce D. Clarke, Santanu Das, Jean-Michel Désert, Michael Endl, Daniel Fabrycky, Francois Fressin, Michael Haas, Elliott Horch, Andrew Howard, Howard Isaacson, Hans Kjeldsen, Jeffery Kolodziejczak, Craig Kulesa, Jie Li, Philip W. Lucas, Pavel Machalek, Donald McCarthy, Phillip MacQueen, Søren Meibom, Thibaut Miquel, Andrej Prsa, Samuel N. Quinn, Elisa V. Quintana, Darin Ragozzine, William Sherry, Avi Shporer, Peter Tenenbaum, Guillermo Torres, Joseph D. Twicken, Jeffrey Van Cleve, Lucianne Walkowicz, Fred C. Witteborn, and Martin Still. Characteristics of planetary candidates observed by kepler. ii. analysis of the

- first four months of data. *The Astrophysical Journal*, 736(1):19, 2011. URL: <http://stacks.iop.org/0004-637X/736/i=1/a=19>.
- [8] Stanley F. Dermott Carl D. Murray. *Solar System Dynamics*. Cambridge University Press, 1 edition, 2000.
- [9] Veillet C. Connors M, Wiegert P. Earth’s trojan asteroid. *Nature*, 2011 Jul 27(475(7357)):481–3, 2015. URL: <https://arxiv.org/ftp/arxiv/papers/1506/1506.01658.pdf>, doi:10.1038/nature10233.
- [10] George Contopoulos, Luigi Galgani, and Antonio Giorgilli. On the number of isolating integrals in hamiltonian systems. *Phys. Rev. A*, 18:1183–1189, Sep 1978. URL: <https://link.aps.org/doi/10.1103/PhysRevA.18.1183>, doi:10.1103/PhysRevA.18.1183.
- [11] A. Crida. Solar system formation. 2009. arXiv:arXiv:0903.3008, doi:10.1002/9783527629190.ch11.
- [12] Simon Dauth. Das drei-trojaner-problem. *Phys. Rev. A*, 18:1183–1189, Sep 1978. URL: <http://othes.univie.ac.at/28652/>.
- [13] C. de la Fuente Marcos and R. de la Fuente Marcos. Asteroid 2013 nd15: Trojan companion to venus, pha to the earth. *Monthly Notices of the Royal Astronomical Society*, 439(3):2970–2977, 2014. URL: <http://dx.doi.org/10.1093/mnras/stu152>, arXiv:/oup/backfile/content_public/journal/mnras/439/3/10.1093/mnras/stu152/2/stu152.pdf, doi:10.1093/mnras/stu152.
- [14] C. de la Fuente Marcos and R. de la Fuente Marcos. Asteroid (469219) 2016 HO₃, the smallest and closest Earth quasi-satellite. *mnras*, 462:3441–3456, November 2016. arXiv:1608.01518, doi:10.1093/mnras/stw1972.
- [15] J L. de Lagrange. Essai sur le probleme des trois corps. *Oeuvres completes*, 1772.
- [16] 2013 Dvorak R. Lhokta Ch. *Celestial Dynamics: Chaoticity and Dynamics of Celestial Systems*. 2013.
- [17] S. Eggl and R. Dvorak. *An Introduction to Common Numerical Integration Codes Used in Dynamical Astronomy*, pages 431–480. Springer Berlin Heidelberg, Berlin, Heidelberg, 2010. URL: https://doi.org/10.1007/978-3-642-04458-8_9, doi:10.1007/978-3-642-04458-8_9.
- [18] Routh E.J. On laplace’s three particles, with a supplement on the stability of steady motion. *Proc. London Math. Soc.*, 6(86), 1875.

- [19] Morbidelli A. et al. The complex history of trojan asteroids. 2015. URL: <https://arxiv.org/ftp/arxiv/papers/1506/1506.01658.pdf>, doi:10.2458/azu_uapress_9780816532131-ch011.
- [20] Rauer H et al. The PLATO 2.0 mission. *Experimental Astronomy*, 38:249–330, November 2014. arXiv:1310.0696, doi:10.1007/s10686-014-9383-4.
- [21] A. Guilbert-Lepoutre. Survival of water ice in Jupiter Trojans. *icarus*, 231:232–238, March 2014. arXiv:1401.5196, doi:10.1016/j.icarus.2013.12.014.
- [22] M. Hippke and D. Angerhausen. A Statistical Search for a Population of Exo-Trojans in the Kepler Data Set. *apj*, 811:1, September 2015. arXiv:1508.00427, doi:10.1088/0004-637X/811/1/1.
- [23] James F. Kasting, Daniel P. Whitmire, and Ray T. Reynolds. Habitable Zones around Main Sequence Stars. *Icarus*, 101:108–128, 1993. doi:10.1006/icar.1993.1010.
- [24] H. Lammer, A. Stökl, N. V. Erkaev, E. A. Dorfi, P. Odert, M. Güdel, Y. N. Kulikov, K. G. Kislyakova, and M. Leitzinger. Origin and loss of nebula-captured hydrogen envelopes from ‘sub’- to ‘super-Earths’ in the habitable zone of Sun-like stars. *mnras*, 439:3225–3238, April 2014. arXiv:1401.2765, doi:10.1093/mnras/stu085.
- [25] Gregory Laughlin and John E. Chambers. Extrasolar trojans: The viability and detectability of planets in the 1:1 resonance. *The Astronomical Journal*, 124(1):592, 2002. URL: <http://stacks.iop.org/1538-3881/124/i=1/a=592>.
- [26] J. Llibre and M. Ollé. The motion of Saturn coorbital satellites in the restricted three-body problem. *aap*, 378:1087–1099, November 2001. doi:10.1051/0004-6361:20011274.
- [27] P. S. Lykawka, J. Horner, B. W. Jones, and T. Mukai. Origin and dynamical evolution of neptune trojans - i: Formation and planetary migration. 2009. arXiv:arXiv:0909.0404, doi:10.1111/j.1365-2966.2009.15243.x.
- [28] A. Mainzer, T. Grav, J. Bauer, J. Masiero, R. S. McMillan, R. M. Cutri, R. Walker, E. Wright, P. Eisenhardt, D. J. Tholen, T. Spahr, R. Jedicke, L. Denneau, E. DeBaun, D. Elsbury, T. Gautier, S. Gomillion, E. Hand, W. Mo, J. Watkins, A. Wilkins, G. L. Bryngelson, A. Del Pino Molina, S. Desai, M. Gómez Camus, S. L. Hidalgo, I. Konstantopoulos, J. A. Larsen, C. Maleszewski, M. A. Malkan, J.-C. Mauduit, B. L. Mullan, E. W. Olszewski, J. Pforr, A. Saro, J. V. Scotti, and L. H. Wasserman. Neowise observations of near-earth objects: Preliminary results. *The Astrophysical Journal*, 743(2):156, 2011. URL: <http://stacks.iop.org/0004-637X/743/i=2/a=156>.

- [29] F. Marchis, J. Durech, J. Castillo-Rogez, F. Vachier, M. Cuk, J. Berthier, M. H. Wong, P. Kalas, G. Duchene, M. A. van Dam, H. Hamanowa, and M. Viikinkoski. The puzzling mutual orbit of the binary trojan asteroid (624) hektor. *The Astrophysical Journal Letters*, 783(2):L37, 2014. URL: <http://stacks.iop.org/2041-8205/783/i=2/a=L37>.
- [30] F. Marzari, H. Scholl, C. Murray, and C. Lagerkvist. *Origin and Evolution of Trojan Asteroids*, pages 725–738. March 2002.
- [31] Scholl H Marzari F, Tricarico P. Eclues to the origin of jupiter’s trojans: the libration amplitude distribution. *Icarus*, 162 (2003):453–459, 2003. URL: <https://pdfs.semanticscholar.org/eeb7/00f52d92ff8f72a3f501902f2882eaaeed3b.pdf>, doi:doi:10.1016/S0019-1035(03)00026-5.
- [32] Sean M Mills, Daniel C Fabrycky, Cezary Migaszewski, Eric B Ford, Erik Petigura, and Howard Isaacson. A resonant chain of four transiting, sub-neptune planets. *Nature*, 533(7604):509—512, May 2016. URL: <https://doi.org/10.1038/nature17445>, doi:10.1038/nature17445.
- [33] A. Morbidelli, H.F. Levison, K. Tsiganis, and R. Gomes. Chaotic capture of jupiter’s trojan asteroids in the early solar system. *Nature*, 435:462–465, 2005. *Nature*, 435, pp. 462-465, <http://dx.doi.org/10.1038/nature03540>. URL: <https://hal.archives-ouvertes.fr/hal-00388297>, doi:10.1038/nature03540.
- [34] T. Nakamura and F. Yoshida. A New Surface Density Model of Jovian Trojans around Triangular Libration Points. *pasj*, 60:293–296, April 2008. doi:10.1093/pasj/60.2.293.
- [35] David Nesvorný, David Vokrouhlický, and Alessandro Morbidelli. Capture of trojans by jumping jupiter. *The Astrophysical Journal*, 768(1):45, 2013. URL: <http://stacks.iop.org/0004-637X/768/i=1/a=45>.
- [36] S. B. Nicholson. The Trojan Asteroids. *Leaflet of the Astronomical Society of the Pacific*, 8:239, 1961.
- [37] S. J. Peale. The effect of the nebula on the Trojan precursors. *icarus*, 106:308, November 1993. doi:10.1006/icar.1993.1173.
- [38] Dvorak R. *The Role of Resonances in Astrodynamical Systems*. University of Vienna- IfA, <http://www.univie.ac.at/adg/Publications/resonance-cont-phys.pdf>, -.
- [39] J. W. Schopf, A. B. Kudryavtsev, A. D. Czaja, and A. B. Tripathi. Evidence of Archean life: Stromatolites and microfossils. *Precambrian Research*, 158:141–155, October 2007. doi:10.1016/j.precamres.2007.04.009.

- [40] E. M. Shoemaker, C. S. Shoemaker, and R. F. Wolfe. Trojan asteroids - Populations, dynamical structure and origin of the L4 and L5 swarms. In R. P. Binzel, T. Gehrels, and M. S. Matthews, editors, *Asteroids II*, pages 487–523, 1989.
- [41] 2011 Souchay J., Dvorak R (Editors). *Dynamics of Small Solar System Bodies and Exoplanets*. Springer, 2010. doi:10.1007/978-3-642-04458-8.
- [42] J. N. Spitale, R. A. Jacobson, C. C. Porco, and W. M. Owen, Jr. The Orbits of Saturn’s Small Satellites Derived from Combined Historic and Cassini Imaging Observations. *aj*, 132:692–710, August 2006. doi:10.1086/505206.
- [43] P. C. Thomas. Sizes, shapes, and derived properties of the saturnian satellites after the Cassini nominal mission. *icarus*, 208:395–401, July 2010. doi:10.1016/j.icarus.2010.01.025.
- [44] T. A. Vinogradova and Yu. A. Chernetenko. Total mass of the jupiter trojans. *Solar System Research*, 49(6):391–397, Nov 2015. URL: <https://doi.org/10.1134/S0038094615060076>, doi:10.1134/S0038094615060076.
- [45] F. Yoshida and T. Nakamura. Size distribution of faint jovian l4 trojan asteroids. *The Astronomical Journal*, 130(6):2900, 2005. URL: <http://stacks.iop.org/1538-3881/130/i=6/a=2900>.